ABSTRACT

Title of dissertation: QUANTUM MANY-BODY PHENOMENA
IN ULTRA COLD ATOMS
IN OPTICAL LATTICES

Anzi Hu, Doctor of Philosophy, 2011

Dissertation directed by: Professor Bei-Lok Hu
Department of Physics

Two models are discussed here to illustrate the quantum many-body phenomena in mixtures of ultra-cold atoms in optical lattices. The first model describes a mixture of two species of bosonic atoms of equal masses in optical lattices and the second describes a mixture of heavy bosonic atoms and light fermionic atoms in optical lattices. For both models, we assume the trap is present and use parameters typical in experiment.

For the first model, the discussion is aimed at providing a thorough description of the collective behavior of the binary mixture in various interaction regions, with emphasis on two many-body phenomena, pairing and anti-pairing, as a result of the inter-species interaction. The pairing leads to a new type of superfluid order, called the paired superfluid (PSF) and the anti-pairing leads to another type of superfluid order, called the counterflow superfluid (CFSF). In addition, we discuss the coexistence of charge density wave order with the three superfluid orders in the strong interaction region. We use both Luttinger liquid theory and the time evolving block decimation (TEBD) method to study this model in one dimension. The discussion is organized in three parts: the phase diagram and the correlation functions; the noise correlation functions; and the transport properties. Two phase diagrams are constructed to map the different orders in the parameter space. The correlation functions, include noise correlations, are carefully examined for the determination of the orders and for possible detection methods. In the end, the transport properties of the PSF and CFSF orders are studied through the dipole oscillation induced by trap displacement.

For the second model, examining a mixture of heavy bosons and light fermions, the discussion is oriented toward determining the thermal properties of the mixture for attractive inter-species interactions. This work is motivated by experiments creating artificial molecules through optical and magnetic control of ultra-cold atoms. We use the strong coupling (SC) expansion method to evaluate the density profile, the onsite inter-species correlations, the density fluctuations and the entropy per particle. Analytical expressions are derived for all the quantities above as well as the partition function. To benchmark the accuracy, the SC calculations are compared with inhomogeneous dynamical mean field theory (IDMFT) and Monte Carlo (MC) simulation. From the calculations, we find that 1) the efficiency of creating pre-formed molecules is significantly increased by confining the mixtures onto optical lattices; 2) the temperature of the mixtures in optical lattices can be reliably estimated through the density gradient and the density fluctuations.

QUANTUM MANY-BODY PHENOMENA IN ULTRA-COLD ATOMS IN OPTICAL LATTICES

by

Anzi Hu

Dissertation submitted to the Faculty of the Graduate School of the
University of Maryland, College Park in partial fulfillment
of the requirements for the degree of
Doctor of Philosophy
2011

Advisory Committee

Professor Bei-Lok Hu, Chair
Professor Carl Williams
Professor James Freericks (Georgetown University)
Professor Eite Tiesinga
Professor Victor Galitski
Professor Ramani Duraiswami, Dean's representative

©Copyright by

Anzi Hu

2011

to my parents

Acknowledgments

Five years of living and studying in Maryland has been quite a journey. I am grateful to all the people who helped and befriended me along the way and will always cherish the memories of my time in graduate school.

I am fortunate enough to meet Dr. Bei-Lok Hu in the very beginning of the graduate school. I am thankful for the many interesting discussions we had, his introduction to Dr. Carl Williams and other scientists at National Institute of Standards and Technology (NIST), his support for me to pursue research in the field of ultra-cold atoms and his kind reminder that as a theorist, it is always important to keep an eye on the bigger picture and think deeper. Besides research, I am grateful for his sharing many classical music resources in the area, which has become an essential part of my life in the past few years.

I am equally fortunate to be under the guidance of Dr. Carl Williams and am grateful to him for giving me the opportunity to work at NIST and interact with so many brilliant scientists. I would like to thank Dr. Williams for his introduction to computational physics and specifically the time evolving block decimation (TEBD) method, which has lead to fruitful research and helped my understanding of many-body effects in reduced dimensions, and his introduction to Dr. Maciej Maśka of University of Silesia and Dr. Jim Freericks of Georgetown University. I am also very grateful for being able to walk into Dr. Williams' office whenever I have a question, despite his busy schedule. I cannot imagine being in today's position without his guidance and advices.

During my stay at NIST, I have met and interacted with many brilliant scientists. Among them, I would like to first thank Dr. Ludwig Mathey for his guidance and collaboration on studies of one dimensional Bose mixtures. I am grateful for his introduction to the rich many-body phenomena in one dimension and to the ultra-cold atom experiments, for answering so many of my naive questions and for helping me through the scientific paper writing process. It has been a pleasure working with him.

I would like to thank Dr. Ippei Danshita for his assistance on the TEBD code and very helpful discussions. I would like to thank Dr. Eite Tiesinga for his advice and discussions, particularly for his involvement in the research on one dimensional Bose mixtures and his careful editing of our paper. I also would like thank Dr. Charles Clark for giving me the opportunity of working with Dr. Mathey and Dr. Danshita in his division, spending time editing our paper on the noise correlations and his kind invitation to the QIBEC talks as well as many other events. I would like thank Dr. Paul Julienne for the helpful discussions on atomic systems in optical lattices.

While working on the Bose-Fermi mixtures, I was fortunate to meet Dr. Maciej Maśka and Dr. Jim Freericks. I am especially grateful for Dr. Maśka's hospitality during my stay in Poland and for his teachings on the Monte Carlo method and on numerical simulation in general. I would like to thank Dr. Jim Freericks for his introduction to the strong coupling expansion method. I have benefited greatly from his thorough and solid knowledge in condensed matter physics and his careful attitude towards research.

Besides research, I have enjoyed many graduate courses. I still feel quite fortunate for learning statistical mechanics from Dr. Michael Fisher. His teaching was not just about the knowledge but also about scientific thinking and questioning and his homework problems often felt like research projects, which can be challenging sometimes, but always stimulating. I also want to thank Dr. Victor Galitski for his class on solid state physics, where I got my first glimpse of renormalization group theory, and many other important concepts and methods in condensed matter physics. Although I have not worked on any research related with relativity, Dr. Ted Jacobson's introduction to general relativity was so fresh and enjoyable that I was completely absorbed in the curved space during that course. I am also very happy that I chose to take the scientific computing class by Dr. Ramani Duraiswami at the end of my coursework Dr. Duraiswami's class introduced me to the basic computer science knowledge that turned out to be very helpful to my research and has since greatly influenced the way I write programming codes.

I owe my deepest thanks to my family - especially my mother, who has been staying with me for the past half year. She is always my best friend and best supporter. She and my dad have always respected and supported me even when they disagree with my choices. Words cannot express my gratitude for their unconditional love.

In retrospective, so many people inside and outside school have helped me along my five years in Maryland. Without them, this thesis would never be possible. I can't believe myself how lucky I have been.

Contents

List of Figures **ix**

List of Tables **xxiv**

1 Introduction **1**

1.1 Second quantization 4

1.1.1 Bose Hubbard model 5

1.1.2 Multi-component Hamiltonian 7

1.2 Phase diagram 9

1.2.1 Off diagonal long-range order 9

1.2.2 Order parameter 10

1.2.3 Superfluid to Mott insulator phase transition 12

1.3 Tomonaga-Luttinger liquid theory 13

1.4 Detection Methods 17

1.4.1 Time-of-flight measurement 17

1.4.2 Noise correlation 18

1.4.3 *In situ* measurement 20

2 Time evolving block decimation method **21**

2.1 Basic TEBD method 21

2.1.1 State decomposition 21

2.1.2 Single-site and two-site operations 25

2.1.3 Time evolution 28

2.1.4 Observables 30

2.2 Extended TEBD method 32

2.2.1 Number conservation 32

2.2.2 One dimensional two-component Hamiltonian 35

2.3 Efficiency and accuracy estimation 37

2.4 Example: one-dimensional Bose Hubbard model 37

- 2.4.1 Homogeneous System 38
- 2.4.2 Harmonic trap 41
- 2.4.3 Accuracy estimation 42

3 One dimensional binary Bose mixtures in optical lattices (I): paired and counter-flow superfluidity 46

- 3.1 Introduction 46
- 3.2 Two-component Bose Hubbard model 49
- 3.3 Luttinger liquid approach 49
- 3.4 Numerical approach 56
  - 3.4.1 Phase diagram 62
    - 3.4.1.1 Phase diagram at a fixed hopping parameter 62
    - 3.4.1.2 Phase diagram at half-filling 63
  - 3.4.2 Realization and detection 65
- 3.5 Summary 69

4 One dimensional binary Bose mixtures in optical lattices (II): noise correlation 73

- 4.1 Noise correlations and quasi-orders 74
- 4.2 Luttinger liquid approach 76
- 4.3 Numerical approach 82
  - 4.3.1 Homogeneous systems 83
  - 4.3.2 Trapped systems 88
  - 4.3.3 Determination of Luttinger parameters from experimental data . . . 91
- 4.4 Summary 92

5 One dimensional binary Bose mixtures in optical lattices (III): transport properties 93

- 5.1 Dynamics after a trap displacement 94
  - 5.1.1 Model and parameters 94
  - 5.1.2 Simulation of the real time evolution 95

5.2 Result 96
5.2.1 Brief displacement 97
5.2.2 Constant displacement 101
5.3 Summary 103

6 Two dimensional Bose-Fermi mixtures in optical lattices: pre-formed molecules and novel thermometry 105

6.1 Introduction 105
6.2 Fermi-Bose Falicov-Kimball model 108
6.3 Strong coupling expansion formalism 112
6.4 Results 119
6.4.1 Comparison with the IDMFT and MC calculations 119
6.4.2 Finite-size effects 123
6.5 Thermometry 128
6.5.1 Temperature and Density fluctuations 128
6.5.2 Fluctuation calculation 129
6.5.3 Results 132
6.6 Summary 135

7 Conclusion and further discussions 136

Bibliography 139

List of Figures

2.1 Number fluctuations Δ_j and density distribution $\langle n_j \rangle$ for $U/t = 1$(a), 4(b), 10(c), 20(d). The total number of particle is 50. The density distribution is uniformly 1 except for at the boundary. In (a) and (b), the system is in the SF state, this is reflected by the large number fluctuation. In (c) and (d), the system is in the MI state and the number fluctuations are much reduced. . . 39

2.2 One-body density matrix $G_{ij} = \langle b_i^\dagger b_j \rangle$ for $U/t = 1$(a), 4(b), 10(c) and 20(d). The parameters are the same as in Fig. 2.1. In (a) and (b) the system is in the SF state. In (c) and (d) the system is in the MI state. In (a), G_{ij} decays very slowly and the correlation function is forced to zero by the boundary condition at the edge of the lattice. In (b), G_{ij} decays faster than in (a) but still qualifies as algebraic decay (see also Fig. 2.3) with a larger decay power. In (c) and (d), G_{ij}becomes short-ranged and the decay behavior changes to exponential. 40

2.3 Algebraic and exponential fit for G_{ij}. Here we choose $i = 25$, $j = 25, ...50$. The function $G_{25,j}$ represent the decay behavior of the off-diagonal one body density matrix. Through the fit, one can obtain the Luttinger parameter K, $K = 9.4$ in (a) and $K = 6.4$ in (b). The decay length X_0 can be found for the exponential decay, $X_0 = 1.5$ in (c) and $X_0 = 0.75$ in (d). 41

2.4 Density distribution and number fluctuations in a trapped system. In (a), the system is in the SF state with $U/t = 1$ In (b), the interaction is strong, $U/t = 20$. The density forms a plateau near the center of the trap. This is where the MI state is formed. The fluctuations are reduced at the plateau area as the result of the MI order. The SF state still exists at the edge of the trap. 42

2.5 One-body density matrix in a trapped system. The parameters in (a) and (b) are the same as in Fig. 2.4. In (a), the system is in the SF state. The density matrix is reduced dramatically to zero near the edge of the cloud. In (b), the off-diagonal decay is exponential in the MI region. The decay changes to algebraic as a result of the SF state at the edge. 43

2.6 Vector $\lambda^{[l]}$ as a function of l and α. The decomposition rank χ is 50 and the size of the system is 50 lattice sites. In (a) and (b), the value of λ decreases to around 10^{-4} for $\alpha = 50$ at the center. In (c) and (d), the value of λdecays rapidly as α increases and is less than 10^{-9} at $\alpha = 50$. 44

2.7 Decay of $\lambda^{[25]}$ in SF and MI states. Here, $\lambda^{[25]}$is chosen because it relates with the Schmidt rank at the center of the lattice, which usually has the slowest decay with regard to α. The vector $\lambda^{[25]}$ decays much faster in the MI region than in the SF region. 44

2.8 Behavior of $\lambda^{[j]}$ for a trapped system. In (a), $\lambda^{[l]}$ corresponds to the SF state of Fig. 2.4 (a) and in (b), $\lambda^{[l]}$ corresponds to the MI-SF mixed state of Fig. 2.4 (b). The behavior of λ reflects the orders that exists in the trap. 45

3.1 Sketch of a condensate of pairs. Atoms of each species (red/green) pair together and form a paired superfluid (PSF) state. 47

3.2 Sketch of a condensate of anti-pairs. Here, atoms of one species are strongly anti-correlated with atoms of the other species, creating a counterflow superfluid (CFSF) state. These composite bosons can also be thought of as a pair of one atom of one species and one hole of the other species. 48

3.3 Phase diagram of a bosonic mixture at non-unit and non-half-filling. For attractive interactions U_{12} and $K < 2$ the system can form a paired superfluid state, in the regime labeled PSF and PSF(CDW). This phase can coexist with CDW order for weaker interactions. For large repulsive (attractive) interactions U_{12} the system phase separates (PS) (collapses (CL)). For the remaining regime the system shows single particle superfluidity (SF). This can coexist with CDW order, resulting in a quasi-supersolid (SS) regime. 53

3.4 Phase diagram of a bosonic mixture at half-filling. In addition to the phases that appear in Fig. 3.3, the system now develops a counterflow superfluid (CFSF) phase, which can coexist with CDW order. 55

3.5 Correlation functions R_A, R_S, and G on a logarithmic scale as a function of distance $|i-j|$. The index i is 40, the center of the 80 lattice sites. The squares are the numerical data. The blue lines are exponential fits to the data and red dotted lines are algebraic fits. Note that the scale of the vertical axis of the graphs differs by orders of magnitude. In (a), we show an example for the paired superfluid phase at ν=0.3, $t = 0.02U$, and $U_{12} = -0.16U$. R_A decays exponentially and R_S decays algebraically. The single-particle correlation function decays exponentially, implying the absence of single-particle superfluidity. In (b), we show an example for the counterflow superfluid phase at $\nu = 0.5$, $t = 0.02U$, and $U_{12} = 0.2U$. The anti-pair correlation function R_A decays algebraically, while the pair correlation function decays exponentially. Single-particle superfluidity is again absent. The algebraic fits deviate from the data around $|i-j| \approx 40$, due to the boundary conditions of our numerical calculations. 58

3.6 (a) K_S and K_A as a function of U_{12} as extracted from the fit of the correlation functions, R_S and R_A. The filling ν is 0.7 and t/U is 0.02. Around $U_{12}/U \approx -0.06$, the anti-pair correlation function changes from algebraic to exponential decay. This corresponds to the transition from the PSF to SF phase. When R_A decays exponentially, K_A is formally set to zero. For $K_a + K_s \lesssim 2$, the system has CDW order. Error bars are one standard deviation uncertainties obtained from the power-law fit to the numerical data. (b) Comparison of K_A obtained from our RG and TEBD calculations. The red square connected by lines are the TEBD results while all other lines are determined from the RG flow with flow parameter $l = 3, 4, 7$, and 10, where l is defined in Eq. 3.10. The error bars are as in panel (a). The PSF-to-SF transition obtained from TEBD is around $U_{12}/U \approx -0.06$, while the RG calculation shows that for $l = 10$, the transition occurs near $U_{12}/U \approx -0.01$. We interpret the regime between $U_{12}/U \approx -0.06$ and -0.01 the cross-over region. 60

3.7 Phase diagram for a homogeneous system with 80 sites and the hopping parameter $t = 0.02$U as a function of filling ν and inter-species interaction U_{12}/U. The horizontal axis shows three disconnected regions in U_{12}/U. The solid lines are the estimated phase boundaries based on the TEBD results and the dotted line is the PSF-to-SF phase boundary predicted by our RG calculation (see Eq. 3.20). For attractive interaction $U_{12} \lesssim -0.06U$, the system forms a paired-superfluid (PSF). The state collapses(CL) for $U_{12} \lesssim -0.7U$. For $U_{12} \gtrsim -0.06$ and $U_{12} \lesssim U$ the system shows single-particle superfluidity (SF). The system phase-separates (PS) for $U_{12} \gtrsim 1$ and forms two single-particle superfluids (SF). Open circles are the points where $K_S+K_A < 2$ and charge density wave (CDW) order coexists with a superfluid phase (SF,PSF, or CFSF). At half and unit filling there exist special phases. For repulsive interaction $U_{12} \gtrsim 0.08U$ and half-filling, the system forms a counterflow superfluid (CFSF). For unit filling, we find a Mott-Insulator (MI) phase for interactions $|U_{12}| \lesssim U$. Finally, in the PS region at half- and unit-filling, the system forms two individual MI states. 61

3.8 Phase diagram at half-filling as a function of U_{12}/U and t/U. The solid lines are estimated phase boundaries from the TEBD calculation and the dotted lines are the phase boundaries predicted by the RG calculation (see Eqs. 3.20 and 3.24). For large repulsive interaction, the system phase separates (PS) and for large attractive interaction, the system collapses (CL). For moderate interactions and for $t/U \lesssim 0.2$, the system shows paired superfluidity (PSF) on the attractive side and counterflow superfluidity on the repulsive side. Both PSF and CFSF can coexist with charge density wave (CDW) order when $t \lesssim 0.1U$. 64

3.9 Density distribution of a trapped system for $t = 0.02U$. (a) Attractive interaction U_{12}. The trap frequency is $\Omega = 1 \times 10^{-5}U$ and the number of atoms is 20 for each species. For attractive interactions, the density distributions of the two species are identical. For $U_{12} = -0.01U$ (curve I) the system is superfluid. For $U_{12} = -0.11U$ (curve II) and $U_{12} = -0.21$U (curve III), the system is in the paired superfluid (PSF) state. As U_{12} becomes more negative the distribution gradually shrinks in size. (b) Repulsive interaction $U_{12} = 0.2U$ with $\Omega = 8 \times 10^{-5}U$ and 30 atoms of each species. The red and green curves correspond to the species, respectively. The density distribution has a 'plateau' with half-filling in the center of the trap. The system is in a counter-flow superfluid (CFSF) state. The two species have weak interlocked density modulations around half filling. 66

3.10 Density distribution after a time-of-flight expansion. We assume ^{87}Rb atoms and use an expansion time of 0.03s. The hopping energy is $t = 0.02U$. Panel (a): For attractive interaction U_{12}, we show the TOF expansion of a SF state at $U_{12} = -0.01U$ (red line) and of a PSF state at $U_{12} = -0.21U$ (green line). The two curves correspond to the expansion of the densities shown as curve I and III in Fig. 3.9(a) The trap frequency is $\Omega = 1 \times 10^{-5}U$. Panel (b): For repulsive interaction, we show a TOF expansion of a SF state at $U_{12} = 0.01U$ and of a CFSF state at $U_{12} = 0.21U$. The trap frequency is $\Omega = 8 \times 10^{-5}U$. . 67

3.11 Density distribution of molecules after time-of-flight expansion of state III in Fig. 3.9(a). The expansion time is 0.03s. We assume two hyperfine states of ^{87}Rb. These are converted into Feshbach molecules at $T = 0$ via a fast ramp across a resonance. We assume a complete conversion. The strongly peaked interference pattern of molecules indicates the presence of a quasi-condensate of pairs. For comparison, we also show the TOF expansion of atoms in the PSF phase for the same parameters. The broad Lorentzian distribution demonstrates the absence of single-particle SF. 71

3.12 Structure factor at filling $\nu = 0.3$. For $U_{12} = -0.01U$ the system is in the SF regime (dashed line) and for $U_{12} = -0.07U$ the system is in the PSF regime (continuous line). Cusps at $|k| = 2\pi\nu$ only occur for $U_{12} = -0.07U$ indicating the coexistence of CDW with PSF order. 71

3.13 Structure factor $S_{+}(k)$ (blue line) after applying a $\pi/2$ pulse in the CFSF phase. The quasi-condensate of anti-pairs generates an algebraic peak at $k = 0$. The cusp also appear in the Fourier transform of the anti-pair correlation function $R_a(i,j) = \langle b^\dagger_{1,i} b_{2,i} b^\dagger_{2,j} b_{1,j}\rangle$(red dashed line). 72

4.1 Noise correlations in different phases, derived from Luttinger liquid theory. In the MI state (column (a)), δ-function like correlations along $k = k'$ in $\mathcal{G}_{11}(k,k')$ are visible, whereas $\mathcal{G}_{12}$ nearly vanishes. In the SF state (column (b)), with Luttinger parameters $K_A = 1.03$ and $K_S = 0.96$, we find various contributions in $\mathcal{G}_{11}$, especially δ- function along $k = k'$. In Fig. 4.2, we show the contour plots for $\mathcal{G}_{11}$ and $\mathcal{G}_{12}$ for the same state, where we can see the negative correlations at $k = 0$ and $k' = 0$, as well as pairing correlation along $k = -k'$, which is similar to the single-species result in Ref. [35]. $\mathcal{G}_{12}$ shows similar features, but the bunching contribution is an algebraic peak, rather than a δ-function. In (c) we show an example for the PSF phase, with $K_A = 0.01$ and $K_S \simeq 1.3$, in (d) an example for the CFSF phase, with $K_S = 0.01$ and $K_A \simeq 1.2$. In the PSF state, the inter-species correlation $\mathcal{G}_{12}(k,k')$ has strong correlations along $k = -k'$, a reflection of pairing. In the CFSF state, the peak is formed along $k = k'$ direction, an indication of the anti-pairing (particle-hole) formation in the CFSF state. 77

4.2 Noise correlations, $\mathcal{G}_{11}(k,k')$ (a) and $\mathcal{G}_{12}(k,k')$ (b), in the SF state. The data used here are the same as those used in Fig. 4.1 (b). We create the non-linear gray scales by plotting functions $\tanh(500\mathcal{G}_{11})$ (a) and $\tanh(10^5\mathcal{G}_{12})$ (b), in order to magnify the details around $k = k' = 0$. The labels of the color-bar reflect the values of $\mathcal{G}_{11}(k,k')$ and $\mathcal{G}_{12}(k,k')$. In these plots, we can clearly see the negative correlations between the quasi-condensate ($k = 0$ and $k' = 0$) and the higher momentum states at the quantum depletion, as well as the anti-pairing correlation along $k = k'$ and the pairing correlation along $k = -k'$. 77

4.3 Noise correlations for a homogeneous system of 40 lattice sites, calculated with the TEBD method. The frames (a) – (d) correspond to the examples (a) – (d) in Table 4.1. In (a), we show the noise correlations of a MI state. In the plot of $\mathcal{G}_{11}(k,k')$, there is a strong correlation along the direction $k = k'$, whereas the noise correlation function $\mathcal{G}_{12}(k,k')$ essentially vanishes. In (b), we show the noise correlations of a SF state. Here, we can see the peak around $k = k'$ corresponding to the δ- function bunching peak predicted by Luttinger Liquid theory (see also Fig. 4.1 (b)). For $\mathcal{G}_{12}$, we find negative value at $k = k' = 0$, which is different from the Luttinger Liquid result (Fig. 4.1 (b)). Other structures predicted by Luttinger Liquid theory can be seen in Fig. 4.4, where $\mathcal{G}_{12}$ and $\mathcal{G}_{11}$ are plotted in a non-linear color scale to magnify the structures around $k = k' = 0$. In (c) and (d), we show the noise correlations of the PSF and CFSF state, respectively. In the PSF state (c), the inter-species correlation $\mathcal{G}_{12}(k,k')$ has strong correlations along $k = -k'$, a consequence of pairing (see also Fig. 4.1 (c)). In the CFSF state (d), the peak is formed along the direction $k = k'$, an indication of anti-pairing in the CFSF state (see also Fig. 4.1). 83

4.4 Noise correlations, $\mathcal{G}_{11}(k,k')$ (a) and $\mathcal{G}_{12}(k,k')$ (b), in the SF state of a homogeneous system. The values of $\mathcal{G}_{11}(k,k')$ and $\mathcal{G}_{12}(k,k')$ are exactly the same as in Fig. 4.3 (b). We create non-linear gray scales by plotting $\tanh(10\mathcal{G}_{11})$ and $\tanh(200\mathcal{G}_{12})$ in linear scales. The labels of the color-bar reflects the values of $\mathcal{G}_{11}(k,k')$ and $\mathcal{G}_{12}(k,k')$. The features around $k=k'=0$ are magnified as a result of the non-linear scale. In (a), we find the features predicted by LL calculations (4.2 (a)). In addition, we can see a weak correlation at around $k=k'\pm 2k_F$, where $k_F=\nu\times\pi/a_L=0.5\pi/a_L$. This is where a strong correlation (cusps) will develop if CDW order is present. This feature can also been shown in Luttinger Liquid calculations at around $k\approx 0$ and $k'\approx 2k_F$ (Eq. 4.23). In (b), we find that the structures along $k=k'$ is similar with the ones in Luttinger Liquid calculations, however, the structures along $k=-k'$ is negative, different from the Luttinger Liquid predictions (see also Fig. 4.2). The difference may be understood as a result of different boundary conditions used for the finite-size calculations: the numerical calculations use a "hard-wall" boundary condition, whereas the Luttinger Liquid calculations assume a periodic boundary condition. 84

4.5 Left : The correlation function $C_{11}(q)$, as defined in Eq. 4.2; right: the structure factor $S(k)$ for a quasi-supersolid state. The parameters are given in example (5) of Table. 4.1. The Luttinger parameters are $K_A\approx 1.4$ and $K_S\approx 0.57$. The filling fraction is $\nu=0.2$, hence the "Fermi wave vector" k_F is $\pi\times 0.2$. At momentum $2k_F$, both quantities develop cusps, indicating the presence of CDW order. 86

4.6 Noise correlations in the trapped system. The system size is 80 sites and $t/U = 0.02$. In (a), the system is in the SF state. The particle number of each species is 30, the trap frequency $8 \times 10^{-5}U$ and $U_{12}/U = 0.01$. In (b), the particle number of each species is 40, the trap frequency $1 \times 10^{-4}U$ and $U_{12}/U = -0.11$. The system has both MI and PSF orders. The MI state forms a plateau at unit-filling at the center of the trap and the PSF is formed at the edge. The PSF state at the edge causes the small peak along the $k = -k'$ direction, similar to the one in (c). However, this peak is at a much smaller amplitude than the one shown in (c), where the whole system is a PSF state. In (c), the particle number of each species is 20, the trap frequency $1 \times 10^{-5}U$ and $U_{12}/U = -0.11$. The whole system is in the PSF state. A strong pairing correlation is formed along $k = -k'$ direction. In (d), the particle number of each species is 30, the trap frequency is $8 \times 10^{-5}U$ and $U_{12}/U = 0.2$. The system has both CFSF and SF order. The CFSF order forms a plateau at half-filling at the center of the trap and the SF state towards the edges of the trap. The CFSF order causes a strong anti-pairing (particle-hole) correlation along $k = k'$direction. At the same time, the SF order adds to the "dips" along $k = 0$ and $k' = 0$. 89

4.7 Correlations $C_{12}(q)$ and $D_{12}(q)$ for the states that are described in Fig. 4.7. In (a), we show the behavior of $C_{12}(q)$ (Eq. 4.2) in SF, MI, PSF and CFSF states. The strong anti-pairing (particle-hole) correlations in the CFSF state gives a strong signal around $q = 0$ in $C_{12}(q)$. This strong signal is also unique to the CFSF state and therefore can be used to detect to the CFSF order. In (b), we show the behavior of $D_{12}(q)$ (Eq. 4.3) in SF, MI, PSF and CFSF states. The strong pairing correlation in the PSF state is the reason for the high peak around $q = 0$ in $C_{12}(q)$. This suggests measuring $C_{12}(q)$ is a good way of detecting the PSF order. 90

4.8 Noise correlation $C_{11}(q)$ and structure factor $S(k)$ in a PSF/CDW state. The system size is 80 sites and there are 20 particles of each species ($\nu = 0.25$). The trap frequency is $\Omega = 10^{-5}U$, the hopping $t = 0.02U$ and the inter-species interaction is $U_{12} = -0.11U$. The density at the center of the trap is roughly 0.45 per site and the cusps are developed around $\pm 0.9\pi$. The inhomogeneity of a trapped system means that the "Fermi wave vector" k_F is no longer $\pi\nu$, where ν is the average filling of the system. Instead, k_F can be evaluated as πn_{center}, where n_{center} is the density at the center of the trap, 90

5.1 Dipole oscillation in the CFSF state. Note that time t is in the unit of $\hbar/J$ for all plots. At $t = 0$, the density distributions of both species have the same plateau at half-filling and then the trap of species 1 is briefly perturbed by a displacement of one lattice site [see Fig. 5.2 (a)]. In (a) and (b), we show the density distributions of species 1 and 2 as a function of time after the brief displacement. Species 1 and 2 have exactly opposite oscillation. In (c), we show the time evolution of the total density of both species. There is no oscillation in the total density and the plateau at the center is fixed at one. In (d), we show the time evolution of the relative density between the two species. The relative density reflects the oscillatory motion in species 1 and species 2. 97

5.2 (a) Trap displacement as a function of time. Only the trap of species 1 is displaced at $t = 0$. The displacement is one lattice site and is removed at $t = 1J/\hbar$. (b)-(d) Dipole oscillation of the center of mass in SF, PSF and CFSF states induced by the displacement of species 1's trap. In the SF state (b), only species 1 are excited at $t = 0$ as a result of displacement. In PSF (c) and CFSF (d) states, both species are excited at $t = 0$ as a result of their pairing and anti-pairing order respectively. The red(green) color stands for species 1(2) for all plots in this chapter. 98

5.3 (a) Trap displacement as a function of time. Here, two traps are displaced by 1 lattice site at $t = 0$ and brought back to the original place at $t = J/\hbar$. (b) Dipole oscillation in the PSF state after the same displacement. (c) Trap displacement as a function of time. Here, two traps are displaced by ± 1 lattice site from the center and brought back to the center at $t = J/\hbar$. (d) Dipole oscillation of center of mass in the CFSF state after the opposite displacement. The parameters used are shown in Table. 5.1. Note that there is no dipole oscillation for the CFSF state under the same displacement and for the PSF state under the opposite trap displacement. 100

5.4 (a) Trap displacement as a function of time. Both traps are displaced by 1 lattice site at $t = 0$. In (b), the system is at SF state. Both species show the heavily damped dipole oscillation. In (c), the system at the PSF state and the two species show identical heavily damped dipole oscillations. In (d), the system is in a CFSF state. The dipole oscillation is overdamped in this case and the center of mass stays near the original equilibrium position before the displacement. 101

5.5 (a) Trap displacement as a function of time. The traps are displaced in the opposite direction by 1 lattice site at $t = 0$. (b) Dipole oscillation of the center of mass induced by the trap displacement. In this case, the PSF state prohibit the separation of the two species and the center of mass stays at the original equilibrium position of the trap before the displacement. For both CFSF and SF states, the center of mass of each species moves apart from each other under the displacement. In the SF case, the oscillation converges to the new equilibrium position of the traps after the displacement. But, in the CFSF case, each species keep moving away from each other, until they reach the edge of the CFSF state. In (c)-(e), we show the density distribution at different times for the CFSF state. 102

6.1 (Color on-line) Efficiency $\mathcal{E}$ as a function of temperature calculated by the SC (red cross), IDMFT (blue triangle) and MC (green circle) methods. The interaction parameters, U_{bb} and U_{bf}, are shown in each plot. In (a), the SC calculation differs from the other two methods for $T < 1t/k_B$. For this region, the SC expansion formulas derived here are no longer accurate. In (b)-(f), all three methods give almost identical results. These calculations also show that almost 100% efficiency is reached for relatively strong attraction, $U_{bf} \geq -6t$, at low temperature, $T < t/k_B$. 120

6.2 (Color on-line) (a) Entropy per particle as a function of temperature T. The SC calculation is marked with red crosses and the IDMFT calculation by the blue line. We find excellent agreement between the SC calculation and the IDMFT calculation. 122

6.3 (Color on-line) Efficiency as a function of entropy per particle for different interaction parameters. Note here that we didn't include the case of $U_{bf} = -2t$, because it is already shown in Fig. 6.1 that the SC calculation is not accurate for low temperatures in this case. In (a) and (b), we consider two different bosonic interaction strengths and five different inter-species interaction strengths. For all parameters, the efficiency reaches 100% when the entropy is very low. For an intermediate entropy, with an entropy per particle around $1k_B$, the efficiency is around 80%. 122

6.4 (Color on-line) Finite-size effects on the radial density profile. We assume a two-dimensional $N \times N$ square lattice with hard-wall boundary conditions. The dotted lines indicate the boundaries of different lattices.The interaction parameters are $U_{bf} = -16t$, $U_{bb} = 11.5t$. We use the density distribution of the fermionic particle to represent the general dependence of density on the lattice size. In (a), we consider the case of low temperature, $T = t/k_B$. Here, the density distribution is concentrated at the center of the trap and there is no difference between different lattice sizes. In (b), we consider the case of high temperature at $T = 20t/k_B$. Here, the density is confined mainly by the size of the lattice. For $N = 50$, the density is confined at the edge of the lattice, $r = 25$. For $N = 100$, the density is again confined at the edge, $r = 50$. For both $N = 200$ and 300, the density goes to zero before reaching the edge of the lattice and the two distributions overlap with each other. We estimate that finite-size effects are eliminated for the 300×300 square lattice for the trap frequency and number of particles considered here. 124

6.5 (Color on-line) Finite-size effects on the entropy per particle and the efficiency. We assume a two-dimensional $N \times N$ square lattice with hard-wall boundary conditions. The interaction parameters are $U_{bf} = -16t$, $U_{bb} = 11.5t$. In (a), we show the behavior of the entropy per particle as a function of temperature for different system sizes. We see the entropy is significantly affected by the finite size when the lattice is smaller than around 200×200. The finite-size effect is not noticeable at lower temperature ($T < 1t/k_B$). 125

6.6 (Color on-line) Efficiency as a function of entropy per particle for a 300×300 square lattice system. We consider 625 atoms for each species. Compared with Fig. 6.3, the efficiency is significantly higher for the same value of the entropy per particle in the 300×300 lattice system when the entropy per particle is large. On the other hand, the behavior is similar in both lattice systems when the entropy per particle is less than $1k_B$. The unit efficiency is reached roughly when the entropy per particle is less than $0.5k_B$. 126

6.7 (Color on-line) Density fluctuations averaged over different numbers of samples. The density fluctuations shown here are the total density fluctuations divided by the input temperature, $T = 2tk_B^{-1}$. All the fluctuations are compared with $-(2V_t r)^{-1}\partial(\rho_b+\rho_f)/\partial r$. According to Eq. (6.50), these two quantities should equal to each other. In (a)-(c), the total number of configuration generated is 2×10^5, with a different sampling strategy. In (a), one sample is taken at every 10^3 configurations, which gives a total of 200 samples to average over. The statistical error in this case is very large. In (b), one sample is taken at every 100 configurations, which gives a total of 2000 samples. The statistical error is reduced compared with (a). In (c), the total number of samples is 2×10^4. The statistical error is the smallest among (a) to (c). In (d), a total of 2×10^6 configurations are generated and 2×10^4 samples are taken at every 100 configurations. 129

6.8 (Color on-line) Extracted temperature as a function of the input temperature. The fluctuations are obtained from 2×10^4 samples out of 2×10^6 configurations. The value of T_1 is the mean of $T_1(r)$ averaged over $12 < r/a < 25$ and the error-bar for T_1 is the standard deviation in $T_1(r)$ [Eq. (6.61)]. The value of T_2 is obtained through Eq. (6.62). The input temperature T is drawn as a straight blue line in both plots. In (a), we show our result for the full range of the input temperature, from $T = 0.2t/k_B$ to $20t/k_B$. In this plot, we find very good overall agreement of T_1 and T_2 with the input temperature for the temperature range considered, particularly for $T > 1t/k_B$. In (b), we blow-up the area inside the black square in (a), which corresponds to the low temperature region, where $T = 0.2t/k_B$ to $0.5t/k_B$. In this region, we find that T_1 shows large relative fluctuations (deviation) from the mean value and the mean value of T_1 differs relatively greater from T. The extracted temperature T_2 however still shows excellent agreement with the input temperature. 133

List of Tables

3.1 Definitions of MI, SF, CFSF and PSF orders in terms of the large x behavior of the correlation functions $R_S(x)$, $R_A(x)$, and $G(x)$, $R_{n,a}(x)$. A: algebraic decay of the form $x^{-\alpha}$; E: exponential decay of the form $e^{-\beta x}$. A correlation function is said to exhibit quasi-order when it is subject to algebraic decay with $\alpha < 2$. In this system, the algebraic decay for R_S, R_A and G always has $\alpha < 2$, while $R_{n,a}$ can have $\alpha \geq 2$. CDW quasi-order exists only when $R_{n,a}$ is described by $\alpha < 2$. 57

4.1 The parameters used in the numerical examples and the Luttinger parameters extracted from the algebraic fit of correlation functions, R_A and R_S. The Luttinger parameters are set to zero when the correlations decay exponentially. The hopping parameter t is $0.02U$ for all cases. The parameters are chosen to represent different orders that can exist in this system. 82

5.1 Parameters used to represent the SF, PSF and CFSF states. The hopping parameter is set at $U/J = 8$ for all cases. The particle number of each species is the same and denoted as N_a. stands for the particle number of either species. 95

Chapter 1

Introduction

Incredibly rich quantum many-body effects are observed (and predicted) in ultra cold atoms [1, 2, 3]. Study in this area now involves methods and concepts from atomic physics, condensed matter physics, quantum information theory and quantum chemistry. With the development of the technology for cooling and manipulating atoms, dilute gases of alkali or alkaline-earth atoms can be cooled to temperatures below micro-Kelvin. The extremely low temperature leads to the realization of quantum degenerate gases such as the Bose-Einstein condensate [4, 5] and the Fermi degenerate gas [6]. With the ability to adjust the interaction strength through the Feshbach resonance [7] and the possibility of changing the dimensionality with optical potentials and of generating optical lattices [8], the dilute gases can display many-body phenomena that are characteristic of strongly correlated systems, which typically exist only in the dense and strongly interacting quantum liquids of condensed matter or nuclear physics.

In principle, an accurate quantum description of such many-body phenomena requires solving the many-body Schrödinger equation with the inclusion of the scattering interaction and the interaction with the optical potential. In practice, the Schrödinger equation of such large systems is impossible to solve directly. However, the resemblance between ultra-cold atoms in optical lattices and a conventional condensed matter system is often made, with atoms in analogy to electrons and the periodic optical lattice to the periodic crystalline lattice [9, 10]. Such resemblance leads to suggestions that the many-body phenomena for ultra-cold atoms can be studied through the methods used in the condensed matter theory, such as non-relativistic field operators and the second quantization of the many-body Hamiltonian. Describing ultra-cold atoms in optical lattices with second quantized many-body Hamiltonians has lead to the successful prediction of the quantum phase transition between the superfluid (SF) and the Mott insulator (MI) states as the amplitude of the optical lattice increases [10]. This SF to MI transition has been observed in three [11], quasi-two [12] and quasi-one dimensions [13] in ultra-cold atom experiments.

In this thesis, the discussion is focused on two types of ultra-cold atom mixtures in optical lattices in reduced dimensions. The first mixture consists of two species of bosonic atoms of equal mass. We assume that the system is in one dimension, which can be studied efficiently by the Luttinger liquid theory and the time evolving block decimation (TEBD) method. The discussion for this system is carried on in four parts: the introduction to the TEBD method in Chapter 2; the phase diagram and correlation functions in Chapter 3, the noise correlation functions in Chapter 4, and the transport properties in Chapter 5. In Chapter 6, we discuss the second model, which consists of heavy bosonic and light fermionic atoms. The discussion is focused on the pre-formed molecules in such systems.

For the rest of this chapter, we would like to give a brief introduction to the basic concepts and methods that are most relevant to discussions in the later chapters.

Publications in the PhD work:

- Chapter 3:
  - *Counterflow and paired superfluidity in one-dimensional Bose mixtures in optical lattices*, Anzi Hu, L. Mathey, Ippei Danshita, Eite Tiesinga, Carl J. Williams, and Charles W. Clark, Phys. Rev. A **80**, 023619 (2009).
- Chapter 4:
  - *Noise correlations of one-dimensional Bose mixtures in optical lattices*, Anzi Hu, L. Mathey, Carl J. Williams, and Charles W. Clark, Phys. Rev. A **81**, 063602 (2010).
- Chapter 5:
  - *Detecting paired and counterflow superfluidity via dipole oscillations*, Anzi Hu, L. Mathey, Ippei Danshita, Carl J. Williams, and Charles W. Clark, in preparation.
- Chapter 6
  - *Improving the efficiency of ultracold dipolar molecule formation by first loading onto an optical lattice*, J. K. Freericks, M. M. Maśka, Anzi Hu, Thomas M. Hanna, C. J. Williams, P. S. Julienne, and R. Lemański, Phys. Rev. A 81, 011605 (2010).
  - *Efficiency for preforming molecules from mixtures of light Fermi and heavy Bose atoms in optical lattices: the strong-coupling-expansion method*, Anzi Hu, J. K. Freericks, M. M. Maśka, C. J. Williams, in preparation.

1.1 Second quantization

Theoretical studies on interacting many-body systems almost always start with a second quantized Hamiltonian. Here, we discuss the general procedure of the second quantization (for detailed discussion, see for example [14]) and then derive several of the many-body models relevant to ultra-cold atoms in optical lattices.

Creation and annihilation operators: In general, we can assume that there exists a quantum-mechanical basis that describes the number of particles occupying each state in a complete set of single-particle states and introduce the vector state as

$$|n_1, n_2, ..., n_\infty\rangle \tag{1.1}$$

where the notation means that there are n_1 particles in the eigenstate 1, n_2 in the eigenstate 2, etc. We also assume that this basis is complete and orthonormal. The creation and annihilation operators are introduced as operators that create or annihilate one particle from the corresponding eigenstate. For bosonic particles, the creation and annihilation operators follow the same rule as those for harmonic oscillators:

$$\left[b_r, b_s^\dagger\right] = \delta_{r,s},\ [b_r, b_s] = \left[b_r^\dagger, b_s^\dagger\right] = 0. \tag{1.2}$$

For fermionic particles, the creation and annihilation operators satisfy the anticommutation rules,

$$\left\{c_r, c_s^\dagger\right\} = \delta_{r,s},\ \{c_r, c_s\} = \left\{c_r^\dagger, c_s^\dagger\right\} = 0, \tag{1.3}$$

where the anticommutator is defined by the following relationship,

$$\{A, B\} \equiv AB + BA. \tag{1.4}$$

Second quantization: For almost all systems with two-body interactions, the Hamiltonian takes the form

$$H = \sum_{k=1}^{N} T(x_k) + \frac{1}{2} \sum_{k \neq l = 1}^{N} U(x_k, x_l). \tag{1.5}$$

Here $T(x_k)$ is the single-particle energy, which includes the kinetic energy, the potential, etc. And $U(x_k, x_l)$ is the energy due to interaction between particles. The second quantization of the Hamiltonian is introduced by applying the field operator,

$$\hat{\psi}(\mathbf{x}) = \sum_j \psi_j(\mathbf{x}) a_j, \tag{1.6}$$

onto the Hamiltonian

$$\hat{H} = \int d^3x \hat{\psi}^\dagger(\mathbf{x}) T(\mathbf{x}) \hat{\psi}(\mathbf{x}) + \frac{1}{2} \int \int d^3x d^3x' \hat{\psi}^\dagger(x) \hat{\psi}^\dagger(x') U(\mathbf{x}, \mathbf{x}') \psi(x') \psi(x). \tag{1.7}$$

Here, the field operator a_j can be either bosonic or fermionic and the function $\psi_j(\mathbf{x})$ is the single-particle wave function. Note that the relationship represented in Eq. (1.7) is independent of the specific representation of field operators. For field operators represented by annihilation operators, the equation above leads to a discretized Hamiltonian which we will derive in the following section. A different way of representing the field operators is discussed in the section of Luttinger liquid theory.

1.1.1 Bose Hubbard model

As suggested in Ref. [10], the Bose Hubbard model can describe a system of bosonic atoms in the optical lattices. In this case, the field operator $\hat{\psi}(\mathbf{x})$ is constructed to describe the behavior of atoms in the lowest energy band of the energy spectrum of a single atom in an optical lattice,

$$\hat{\psi}(\mathbf{x}) = \sum_j w(\mathbf{x} - \mathbf{x}_j) b_j \tag{1.8}$$

where $w(\mathbf{x} - \mathbf{x}_j)$ is the Wannier function of the lowest band and b_j corresponds to the bosonic annihilation operator at lattice site j. The Hamiltonian for the bosonic system is written as,

$$
\begin{aligned}
H &= \int d^3x \hat{\psi}^\dagger(\mathbf{x}) \left(-\frac{\hbar}{2m}\nabla^2 + V_0(\mathbf{x}) + V_T(\mathbf{x}) \right) \hat{\psi}(x) \\
&\quad + \frac{1}{2}\frac{4\pi a_s \hbar^2}{m} \int d^3x \int d^3x' \hat{\psi}^\dagger(x)\hat{\psi}^\dagger(x')\delta(x-x')\hat{\psi}(x')\hat{\psi}(x).
\end{aligned} \tag{1.9}
$$

Here, the first term corresponds to the kinetic energy, $p^2/2m$. The function $V_0(x)$ is the periodic potential created by the optical lattice and $V_t(x)$ is the external trapping potential. In the simplest case, the optical lattice potential can be written as standing waves of wave vector $k = 2\pi/\lambda$, with λ the wavelength of the laser light,

$$
V_0(\mathbf{x}) = \sum_{j=1}^{3} V_{j0} \sin^2(kx_j). \tag{1.10}
$$

The interaction potential is approximated by a on-site interaction with scattering length a_s and atomic mass m.

After the second quantization, the Hamiltonian is written as,

$$
H = -\sum_{\langle j,j' \rangle} t_{j,j'} b_j^\dagger b_{j'} + \sum_j \epsilon_j n_j + \frac{1}{2}U \sum_j n_j(n_j - 1) \tag{1.11}
$$

where n_j is the number operator at site j, $n_j = b_j^\dagger b_j$. The parameter $t_{j,j'}$ is the hopping parameter between site j and j',

$$
t_{j,j'} = \int d^3x w^*(\mathbf{x} - \mathbf{x}_j) \left[-\frac{\hbar^2}{2m}\nabla^2 + V_0(\mathbf{x}) \right] w(\mathbf{x} - \mathbf{x}_{j'}). \tag{1.12}
$$

For the simplest case, the sites j and j' are adjacent sites. The parameter ϵ_j describes the energy offset of each lattice site,

$$
\epsilon_j = \int d^3x V_T(x) |w(\mathbf{x} - \mathbf{x}_j)|^2 \approx V_T(\mathbf{x}_j). \tag{1.13}
$$

And the parameter U describes the interaction between two atoms at site j,

$$U = \frac{4\pi a_s \hbar^2}{m} \int d^3x |w(\mathbf{x})|^4. \tag{1.14}$$

Typically, we consider repulsive interactions, $a_s > 0$, and therefore U is always positive. This model can be further simplified if we assume the energy offset due to the external trapping potential is negligible and the system is homogeneous. In this case, and when a grand canonical ensemble is considered, the energy offset term $\epsilon_j n_j$ is replaced by the chemical potential term, $-\mu n_j$.

1.1.2 Multi-component Hamiltonian

For ultra-cold atom systems with internal degrees of freedom, one can derive multi-component Hubbard-type models similar to the way the Bose Hubbard model is derived. The internal degrees of freedom can be the result of mixed species, mixed atomic states, and/or mixed energy bands. Here, we consider mixed species as an example and introduce α to denote different species. The bosonic and fermionic field operators are now written as a sum of different species,

$$\hat{\psi}_b(\mathbf{x}) = \sum_{j,\alpha} w_\alpha(\mathbf{x} - \mathbf{x}_j) b_{j,\alpha}, \tag{1.15}$$

and

$$\hat{\psi}_f(\mathbf{x}) = \sum_{j,\alpha} w_\alpha(\mathbf{x} - \mathbf{x}_j) c_{j,\alpha}. \tag{1.16}$$

Here $b_{j,\alpha}$ is the bosonic annihilation operator of species α at site j and $c_{j,\alpha}$ is the fermionic annihilation operator of species α at site j. The function w_α is the single-particle Wannier function of species α .

The quantization is carried out in a similar way except for the Hamiltonian is now a matrix in internal degrees of freedom. If we assume there are no cross-species correlations, the Hamiltonian can be written as a sum of single-species Hamiltonians, H_α. The parameters in each H_α depends on each species' atomic properties and their Wannier functions.

For a given lattice, it is possible that different species experience very different hopping and interaction strengths, as a result of different atomic masses and scattering lengths.

If we assume that there are cross-species interactions, i.e. the interaction part of the Hamiltonian is not diagonal, one additional term appears in the Hamiltonian,

$$U_{\alpha\alpha'} n_{\alpha,j} n_{\alpha',j}. \tag{1.17}$$

Here $n_{\alpha,j}$ is either the bosonic or fermionic number operator of species α at site j. For a Bose-Fermi mixture, $n_{\alpha,j}$ and $n_{\alpha',j}$ represent the bosonic and fermionic number operator respectively.

If we assume that the species are associated with each other, i.e. the single particle Hamiltonian is not diagonal, two additional terms can occur in the Hamiltonian: one corresponds to transferring one species to another at one site,

$$t_{\alpha,\alpha',j} a^{\dagger}_{\alpha,j} a_{\alpha',j} + h.c., \tag{1.18}$$

and the other corresponds to transferring one species at site j to another species at site j',

$$t_{\alpha,j;\alpha',j'} a^{\dagger}_{\alpha,j} a_{a',j'} + h.c.. \tag{1.19}$$

Note that such off-diagonal terms can only occur within bosonic or fermionic mixtures, not Bose-Fermi mixtures.

In this thesis, the first model we describe is a two-component Bose Hubbard model in which both components have the same hopping and the same repulsive intra-species interactions. The inter-species interaction in this model can be either positive or negative [see Eq. (3.1)]. For the second model, we consider tunable bosonic intra-species interactions and tunable inter-species interactions and neglect the quantum effect of the hopping of the heavy bosons. This leads to the spinless Bose-Fermi Falicov Kimball model [see Eqs. (6.1-6.3)].

1.2 Phase diagram

1.2.1 Off diagonal long-range order

First discussed by Penrose in Ref. [15], the quantum coherence in Bose-Einstein condensates and the superfluidity in liquid Helium can be characterized by the non-decaying behavior of the single-particle density matrix in the coordinate space representation, i.e.

$$\rho_1(\mathbf{x}, \mathbf{x}') = \langle \hat{\psi}^\dagger(x)\hat{\psi}(x)\rangle \sim constant, \tag{1.20}$$

as $|\mathbf{x} - \mathbf{x}'| \to \infty$. Off diagonal long-range order (ODLRO) is introduced to describe this non-decaying behavior. A more general discussion on ODLRO is given in Ref. [16]. The discussion in Ref. [16] turns out to be relevant not just to superfluidity, but also the pairing and counter-flow effects to be discussed in later chapters.

Here, we consider a many-particle system with fixed number of particles whose density matrix is denoted as ρ,

$$\mathbf{Tr}(\rho) = 1, \tag{1.21}$$

We define the reduced density matrices ρ_1, ρ_2, ρ_3.... as

$$\begin{aligned} \langle i|\rho_1|j\rangle &= \mathbf{Tr}(a_j \rho a_i^\dagger) \\ \langle ij|\rho_1|kl\rangle &= \mathbf{Tr}(a_k a_l \rho a_j^\dagger a_i^\dagger) \\ &etc. \quad , \end{aligned} \tag{1.22}$$

where i, j,... represent single particle states and a_i, a_j,..., are the corresponding annihilation operators. The density matrices ρ_1, ρ_2, and ρ_3 stands for one-, two- and three- particle reduced density matrix. Ref. [16], it argues that ODLRO can occur in groups of particles that are composed of bosons and an *even* number of fermions. In this generalized statement, the Bose Einstein condensate and the superfluid correspond to the ODLRO of $m = 1$. The superconductivity in electronic systems corresponds to the ODLRO of a special group of $m = 2$, where the group is composed of one spin-up and one spin-down fermion.

1.2.2 Order parameter

Also originating from the theory for dilute Bose gases is mean-field theory introduced by Bogoliubov (1947). The key point in mean-field theory is the separation of the condensate contribution from the bosonic field operator. In other words, we can introduce a complex function $\phi(\mathbf{x})$,

$$\phi(\mathbf{x}) = \langle \hat{\psi}(\mathbf{x}) \rangle. \tag{1.23}$$

This function $\phi(\mathbf{x})$ is a classical field (not an operator). It has the meaning of an *order parameter* and characterizes the off-diagonal long-range behavior of the one-particle density matrix,

$$\langle \hat{\psi}^\dagger(\mathbf{x}) \hat{\psi}(\mathbf{x}') \rangle \to \phi^*(\mathbf{x}) \phi(\mathbf{x}'), \tag{1.24}$$

for large $|\mathbf{x} - \mathbf{x}'|$. It immediate follows that if $\langle \hat{\psi}^\dagger(\mathbf{x}) \hat{\psi}(\mathbf{x}') \rangle$ goes to a constant as $|\mathbf{x} - \mathbf{x}'|$ goes to infinity, the order parameter $\phi(\mathbf{x})$ should also approach a constant. In the mean-field theory, the non-zero order parameter is used as an indication of the existence of its corresponding ODLRO.

The concept of the order parameter can be applied to study other long-range orders, such as superconductivity. In the BCS theory [17], the order parameter can be written as

$$\phi \sim \sum_{\mathbf{k}} \langle c_{-\mathbf{k},1} c_{\mathbf{k},2} \rangle. \tag{1.25}$$

Here, the index 1 stands for spin down electrons and 2 stands for spin up electrons. If we define the field,

$$\hat{\psi}_\alpha(\mathbf{x}) = \sum_{\mathbf{k}} e^{-i\mathbf{k}\mathbf{x}} c_{-\mathbf{k},\alpha}, \tag{1.26}$$

the order parameter can be written as the expectation value of the pair,

$$\phi \sim \langle \hat{\psi}_1(\mathbf{x}) \hat{\psi}_2(\mathbf{x}) \rangle. \tag{1.27}$$

Combining Yang's discussion on ODLRO and the order parameter introduced in the mean-field theory, we find that in general one can define an operator to represent to the group of m particles, whose reduced density matrix presents an ODLRO,

$$O_m = a_1 a_2 ... a_m. \tag{1.28}$$

Here O is an operator of the product consisting of the annihilation operators, a_1, a_2, ..., a_m. For the superfluid and the Bose Einstein condensate of identical bosonic particles, this operator is the bosonic field,

$$O_{SF} = \hat{\psi}(x). \tag{1.29}$$

In superconductivity, the operator is the pair of one spin-up and one spin-down fermion, $\hat{\psi}_1(x)$ and $\hat{\psi}_2(x)$,

$$O_{BCS} = \hat{\psi}_1(\mathbf{x})\hat{\psi}_2(\mathbf{x}). \tag{1.30}$$

The correlation function of O_m, $\langle O_m^\dagger(\mathbf{x}) O_m(\mathbf{x}')\rangle$, is the m-particle reduced density matrix and the non-decaying behavior of the correlation function signals the existence of the corresponding ODLRO.

For many quantum many-body models, ODLRO occurs only below a certain critical temperature, when the thermal fluctuation is low. This is the case for the Bose-Einstein condensate, superfluid and superconductivity. ODLRO may also disappear at zero temperature, as a result of the competition between the kinetic energy, the interaction and the external potential. It is also possible that for a given model, several different ODLROs can exist in different parameter regions and sometimes, different ODLROs can coexist, such as the case for supersolid[18]. How to determine the existence of an ODLRO therefore becomes very important, because the ODLRO characterizes the properties of the state. A parameter map can be drawn to show the parameter regions of different ODLRO and the border where the transition occurs. Such a parameter map is often called the phase diagram, which is often used to study the phase transitions for a given model.

1.2.3 Superfluid to Mott insulator phase transition

The existence of two phases in the Bose Hubbard model can be understood from the two extreme cases: 1) the non-interacting case, where $U = 0$; 2) the extremely strong repulsive interaction case, where the hopping is completely suppressed, i.e. $t = 0$.

In the case $U = 0$, the model is quadratic in the operators b_j and $b_j^\dagger$. Transforming the Hamiltonian into the momentum space and diagonalizing the Hamiltonian. We find that the energy spectrum is

$$E = \sum_{\mathbf{q}} \left[\mu - 2t\cos(\mathbf{q} - \pi)\right] n_{\mathbf{q}}. \tag{1.31}$$

and the ground state of the model corresponds to the state where all the atoms occupy the $\mathbf{q} = 0$ state of the lowest band,

$$|\Psi_N\rangle(U = 0) = \frac{1}{\sqrt{N}} \left(\frac{1}{\sqrt{N_L}} \sum_j b_j^\dagger \right)^N |0\rangle, \tag{1.32}$$

where N is the total number of particles and $N_L$is the total number of lattice site.

In the case $t = 0$, the Hamiltonian is diagonal in the Fock state basis, $\prod_j \otimes|\nu_j\rangle$, where ν_j corresponds to the occupation number at site j. The energy at each site j is a function of ν_j as

$$E_j = -\mu\nu_j + U\nu_j(\nu_j - 1). \tag{1.33}$$

For the case where $N/N_L = 1$, the ground state of the system is a MI state with one particle at each site,

$$|\Psi_{N=N_L}\rangle(t = 0) = \prod_{j=1}^{N} b_j^\dagger|0\rangle. \tag{1.34}$$

If we define the order parameter for the SF order as $\langle a_j\rangle$, it is easy to show that $\langle a_j\rangle$ is non-zero in the SF state of Eq. (1.32) and zero in the MI state of Eq. (1.34). These two extreme cases also imply that the phase transition between the SF and the MI states is the result of the competition between the kinetic energy (represented by t), which trys to delocalize the particles and reduce the phase fluctuations, and the *combination* of the interactions and the periodic potential (represented by U), which tries to localize the particles and reduce the density fluctuations. Depending on the values of U and t, either the SF or MI state has lower energy and is energetically favored at very low temperature. The competition between the kinetic energy and the interactions also plays an important role for the pairing and anti-pairing ordering in the mixtures, which is going to be discussed in Chapter 3.

For more rigorous studies on the SF to MI phase transition, one can use many different methods, such as mean-field theory [19, 20] which studies the behavior of the order parameter$\langle a_j \rangle$, the strong-coupling expansion method [22] which studies the energy gap between the ground state in the atomic limit ($t = 0$), $|\Psi\rangle$ and the state with one added particle, $\sim \sum_i a_i^\dagger |\Psi\rangle$ and one hole, $\sim \sum_i a_i |\Psi\rangle$, or quantum Monte Carlo simulation which studies either the correlation function or the density fluctuations [21]. Generally speaking, the SF-MI phase diagram as a function of μ and t/U usually contains loops for the MI state, where the density is fixed at some integer number and is not susceptible to a small change of μ. This indicates the incompressibility of the MI state.

1.3 Tomonaga-Luttinger liquid theory

Quasi-one-dimensional systems can be achieved by loading cold atoms onto a two-dimensional lattice, where the atoms are confined by the cigar-shaped one-dimensional tubes created by the lattice. In these arrays of one-dimensional tubes, interesting quantum many-body phenomena have been observed, such as the Tonks-Girardeau gas [23] and the one-dimensional SF to MI transition. The many-body physics in one dimension has attracted much interest because it is in many senses quite different from the physics in higher dimensions. In one-dimensional systems, the quantum fluctuations play an much enhanced role and there is no true long-range order even at zero temperature. Instead, one can define quasi-long range order through the asymptotic behavior of various correlation functions. Theoretically, these correlation functions and other observables are calculated based on the Tomonaga-Luttinger liquid theory. In this subsection, we briefly describe how Tomonaga-Luttinger liquid theory is applied to one-dimensional bosonic atoms as an example. More detailed discussion about Tomonaga-Luttinger liquid theory and its application in cold atom systems can be found in [24, 25].

We start the discussion by considering the effective Hamiltonian for a homogeneous one-dimensional system of bosonic atoms in lattices,

$$\begin{aligned} H &= \int dx \left[-\frac{\hbar^2}{2m}\partial_x\hat{\psi}^\dagger(x)\partial_x\hat{\psi}(x) + V(x)\rho(x)\right] \\ &\quad +\frac{g}{2}\int dx\hat{\psi}^\dagger(x)\hat{\psi}^\dagger(x)\hat{\psi}(x)\hat{\psi}(x), \end{aligned} \tag{1.35}$$

where $V(x)$ is the lattice potential in one-dimensional system, $V(x) = V_0\sin^2(kx)$ and g is the on-site interaction strength. In Tomonaga-Luttinger liquid theory, the Hamiltonian is rewritten in terms of collective variables that describe the density and phase fluctuations. The advantage of the density-phase presentation is that the interaction term becomes *quadratic* in this presentation, therefore can be treated non-perturbatively. To first illustrate the quadratic form of the Hamiltonian, we consider the case of one-dimensional interacting systems where the lattice is absent, $V(x) = 0$.

The field operator in the density-phase representation up to the leading order is written as

$$\hat{\psi}(x) = (\rho_0 + \frac{1}{\pi}\partial_x\theta)^{1/2}\sum_p e^{i2p(\pi\rho_0 x+\theta(x))}e^{i\phi(x)}. \tag{1.36}$$

Here θ and ϕ are the long wavelength density and phase fields that obey the standard commutation relation

$$[\partial_x\theta(x), \phi(y)] = i\pi\delta(x-y). \tag{1.37}$$

The variable ρ_0 is the average density. The field $\partial_x\theta$ corresponds to the density fluctuation and is assumed to be small compared with ρ_0. Using Eq. 1.36 and retaining only the terms that can become dominant at the low temperature, the Hamiltonian is rewritten as,

$$H_0 = \frac{\hbar v}{2\pi}\int_0^L dx\left[K\left(\partial_x\phi\right)^2 + \frac{1}{K}\left(\partial_x\theta\right)^2\right] \tag{1.38}$$

Here the parameters K and v are dimensionless and depend on both the density ρ_0 and the interaction strength. This Hamiltonian leads to the action,

$$S/\hbar = \frac{1}{2\pi K}\int dx \int d\tau \left[\frac{1}{v}(\partial_\tau\theta)^2 + (\partial_x\theta)^2\right] \tag{1.39}$$

and the partition function is expressed via functional integrals,

$$\mathcal{Z} = \int \mathcal{D}\theta(x,\tau)\int \mathcal{D}\Pi(x,\tau)e^{S/\hbar}, \tag{1.40}$$

where $\Pi = \pi\partial_x\theta$.

The single-particle Green's function and the density correlations are then calculated based on the partition function and the leading orders in the two functions are written as

$$\langle\hat{\psi}^\dagger(x)\hat{\psi}(0)\rangle = A\left(\frac{\alpha}{x}\right)^{\frac{1}{2K}} + ... \tag{1.41}$$

$$\langle\rho(x)\rho(0)\rangle = \rho_0 + \frac{K}{2\pi}\frac{y_\alpha^2 - x^2}{(y_\alpha^2 + x^2)^2} + A_3\cos(2\pi\rho_0 x)\left(\frac{1}{x}\right)^{2K} + ... \tag{1.42}$$

Here $A_j$is a prefactor. The parameters y_α and α are related to the interaction parameters and the temperature. It is interesting to note that the asymptotic behavior of the correlation functions is solely determined by the parameter K. For non-interacting systems, $K = \infty$ and we recover the non-decaying single-particle Green's function, which indicates the existence of the ODLRO and the system is condensed in the lowest momentum state. As the repulsion increase (K decreases), the correlation function decays faster and the system has less and less tendency towards superfluidity. For purely local interactions, $K = 1$ is the minimum, corresponding to the infinitely large local interaction. In this limit, the system is the Tonks-Girardeau gas [26].

Now we consider the effect of adding an optical lattice. Here the existence of a lattice introduces an underlying periodicity for the density, characterized by the lattice constant a_L and the quasi-momentum, $q = 2\pi/a_L$. In the interaction process, the conservation of momentum now takes the form $k_1 + k_2 - k_3 - k_4 = q$. This can be understood as the particles transferring momentum back and forth with the lattice. Such process is known as the umklapp process. Now in this case, the term $e^{i2p(\pi\rho_0 x)}$ in Eq. 1.36 can become non-oscillating for $p \neq 0$ when $p\rho_0 x$ becomes an integer. This is possible in the lattice system, because the position x is discretized as ja_L , where j stands for the j th site in the lattice. When $p\rho_0 = na_L^{-1}$ is satisfied, the corresponding term in the Hamiltonian becomes non-trivial and it leads a new term in the Hamiltonian,

$$H_L \propto g_0 \int dx \cos\left[2p\theta(x)\right]. \tag{1.43}$$

For the Bose-Hubbard model with onsite interaction, H_L is non-trivial only for the case $p = 1$ and it corresponds to an integer number of atoms per site, i.e. $\rho_0 a = n$, with n being any integer. The parameter g_0 depends on the optical lattice potential, $g_0 \sim \rho_0 V_0 (V_0/\mu)^{n_0 - 1}$, where μ is the chemical potential and n_0 is the number of bosons per site.

This Hamiltonian takes the form of the sine-Gordon model and can no longer be computed exactly. Treating H_L perturbatively and use the renormalization procedure, one can find that the parameter K is now determined by flow equations. The behavior of the flow equations reveals that the value of K can either converge to a fixed point K^*, in which case H_L is irrelevant, or continue to grow, in which case the system goes to the strong coupling region. Along the separatrix between these two regions, K converges to the fixed point K_c. For the case where H_L is irrelevant, the Hamiltonian is still written in the quadratic form and the asymptotic behavior of correlation functions can still be written in the form of Eq. (1.41) with K replaced by the fixed point K^*. For the case where the system goes to the strong coupling region, H_L can be expanded around $\theta = 0$, assuming the density is localized at each lattice site, and the second order expansion of H_L leads to a "mass" term in the Hamiltonian. The asymptotic behavior becomes exponential.

For the Bose Hubbard model, the separatrix between these two regions at commensurate fillings corresponds to the fixed point $K_c = 2$. If $|K^* - 2| > 0$, the system is in the SF region. Otherwise, the system is the MI region. It is also worth noting that the sine-Gordon problem is a two-dimensional (one space one imaginary time) problem and the SF-MI transition described here falls into the Berezinskii-Kosterlitz-Thouless (BKT) transition [27]. The SF to MI transition in one dimension has also been studied numerically

[29, 28]

1.4 Detection Methods

1.4.1 Time-of-flight measurement

The time-of-flight (TOF) measurement in the context of ultra-cold atom experiments means measuring the absorption image of the density distribution of atoms after the free expansion when all confinement, including the trap and the optical lattices, is turned off [1]. It is one of the most frequently used experimental methods to detect the coherence properties of ultra-cold atoms. Here we briefly explain the mathematical description of the time-of-flight measurement and the reason why the time-of-flight image can reflect the momentum distribution before the flight.

Let's assume at $t = 0$ (in this section t stands for time, not hopping), both the trap and lattices are turned off and all confined atoms are released and start to expand. Because the gas is usually very dilute, we also assume the expansion is ballistic. Ballistic expansion in free space can be described by the time evolution of the field operator,

$$\hat{\psi}(\mathbf{p}, t) \sim \frac{1}{(2\pi)^3} \int d^3p e^{-i\hbar \mathbf{p}^2 t/2M} \hat{\psi}(\mathbf{p}), \tag{1.44}$$

where

$$\begin{aligned} \hat{\psi}(\mathbf{p}) &= \frac{1}{(2\pi)^{3/2}} \int d^3r e^{-i\mathbf{p}\cdot\mathbf{r}} \hat{\psi}(\mathbf{r}) \\ &= \int d^3r \sum_j w(\mathbf{r} - \mathbf{R}_j) b_j e^{-i\mathbf{p}\cdot\mathbf{r}} \\ &= \sum_j \tilde{w}(\mathbf{p}) e^{-i\mathbf{p}\cdot\mathbf{R}_j} b_j. \end{aligned} \tag{1.45}$$

Here, M is the atomic mass, b_j is the annihilation operator at site j, $w(\mathbf{r})$ is the Wannier function and $\tilde{w}(\mathbf{p})$ is the Fourier transform of the Wannier function. At time t after the expansion, the density distribution at position $\mathbf{x}$ at time t is the expectation value of

$\hat{\psi}^\dagger(\mathbf{x},t)\hat{\psi}(\mathbf{x},t)$

$$\begin{aligned}
\langle \hat{n}(\mathbf{x},t)\rangle &= \langle \hat{\psi}^\dagger(\mathbf{x},t)\hat{\psi}(\mathbf{x},t)\rangle \\
&= \frac{1}{(2\pi)^3}\int d^3\mathbf{p}_1 \int d^3\mathbf{p}_2 e^{-i(\mathbf{p}_1-\mathbf{p}_2)\cdot\mathbf{x}}\langle \hat{\psi}^\dagger(\mathbf{p}_1,t)\hat{\psi}(\mathbf{p}_2,t)\rangle \\
&\simeq (M/\hbar t)^3|w(\mathbf{k})|^2\mathcal{G}(\mathbf{k}), \qquad (1.46)
\end{aligned}$$

where $\mathbf{k}$ is related to $\mathbf{x}$ by $\mathbf{k} = M\mathbf{x}/\hbar t$, and $\mathcal{G}(\mathbf{k})$ characterizes the coherence properties of the initial many-body state,

$$\mathcal{G}(\mathbf{k}) = \sum_{j,k} e^{i\mathbf{k}\cdot(\mathbf{R}_j-\mathbf{R}_k)}\langle b_j^\dagger b_k\rangle. \qquad (1.47)$$

If we redefine $\mathbf{k}$ and $\mathbf{R}_j$ as the momentum and the position vectors in the lattice system as $\mathbf{k} = 2\pi n/N_L a_L$, and $R_j = ja_L$, where a_L is the lattice constant, N_L is the total number of lattice sites and $n = 0, 1, ..M$, the function $\mathcal{G}(\mathbf{k})$ above is exactly the momentum distribution of the atoms in the lattice.

The relationship between the density distribution after the time-of-flight and the momentum distribution before the time-of-flight often leads to the simplified relationship

$$\langle \hat{n}(\mathbf{x},t)\rangle_{TOF} \approx \langle \hat{n}(\mathbf{k})\rangle_{trap}, \qquad (1.48)$$

where the position $\mathbf{x}$ is related to the momentum $\mathbf{k}$ before the expansion with $\mathbf{k} = M\mathbf{x}/\hbar t$. This relationship is usually sufficient to estimate the main features in the time-of-flight measurement.

1.4.2 Noise correlation

In the time-of-flight measurement, each experimental image corresponds to a single realization of the density, not the expectation value. Moreover, each pixel in the image records on average a substantial number N_σ of atoms, while in each single realization of an experiment, the number of atoms on the pixel exhibits shot-noise fluctuations of relative order

$1/\sqrt{N_\sigma}$ [1]. These shot-to-shot fluctuations can be characterized by the density-density correlation function $\mathcal{G}_{\alpha\beta}(\mathbf{x},\mathbf{x}')$,

$$\mathcal{G}_{\alpha\beta}(\mathbf{x},\mathbf{x}',t) = \langle \hat{n}_\alpha(\mathbf{x},t)\hat{n}_\beta(\mathbf{x}',t)\rangle - \langle \hat{n}_\alpha(\mathbf{x},t)\rangle\langle \hat{n}_\beta(\mathbf{x}',t)\rangle. \tag{1.49}$$

Here α and β are the species indices for a system of multiple species. For the system of one species, α and β can be omitted. Similar to the relationship between the time-of-flight density distribution and the momentum distribution before the expansion, the density-density correlation (or noise correlation) function after the time-of-flight is related to the density-density correlation in the momentum space before the expansion,

$$\mathcal{G}_{\alpha\beta}(\mathbf{x},\mathbf{x}',t) \approx \langle \hat{n}_\alpha(\mathbf{k})\hat{n}_\beta(\mathbf{k}')\rangle_{trap} - \langle \hat{n}_\alpha(\mathbf{k})\rangle_{trap}\langle \hat{n}_\beta(\mathbf{k}')\rangle_{trap}, \tag{1.50}$$

where, again, $\mathbf{k} = M\mathbf{x}/\hbar t$. The noise correlation function, $\mathcal{G}_{\alpha\beta}(\mathbf{x},\mathbf{x}',t)$, can be particularly useful for detecting certain strongly correlated orders that can not be revealed in the averaged density distribution image. This is because the noise correlation includes contributions from higher-order correlations as

$$\langle \hat{n}_\alpha(\mathbf{k},t)\hat{n}_\beta(\mathbf{k}',t)\rangle \sim \sum_{j,k} e^{i\mathbf{k}\cdot(\mathbf{R}_j-\mathbf{R}_{j'})+i\mathbf{k}'\cdot(\mathbf{R}_k-\mathbf{R}_{k'})}\langle b^\dagger_{\alpha j} b_{\alpha j'} b^\dagger_{\beta k} b_{\beta k'}\rangle. \tag{1.51}$$

This relationship between the noise correlation function and the higher-order correlation functions was first explained in Ref. [30]. Since then, such analysis has been used to experimentally demonstrate the SF to MI phase transition [31, 32] and the formation of fermionic pairs [33]. Theoretically, it has been shown that the noise correlation functions can also be used to detect the charge density wave order [34, 35, 36, 37, 38]. Noise correlation functions are calculated in one- and two-component Fermi systems [36, 38], as well as bosonic systems in the hard-core limit [40].

1.4.3 *In situ* measurement

Although the time-of-flight image and its density fluctuations can reveal rich information about the long-range order, the measurement can only extract information from the momentum space of the lattice system. The direct observation of atoms and their density distribution *in situ* has been a challenge for many years.

Recent progress in this area has been made: the site-resolved optical imaging of single atoms has been demonstrated in lattices with large spacing [41] and in sparsely populated one-dimensional arrays [42]; imaging of 2D arrays of 'tubes' with large occupations with an electron microscope [43] and optical imaging systems [44]. Most recently, the density profile up to a single site resolution was measured experimentally for a thin layer of atoms in a two dimensional lattice [45] and the high-resolution measurement of the density profile in both SF and MI states in two dimension have been also achieved [46, 47].

The in situ measurements make it possible to directly study the observables in real space and real time. It makes it possible to directly study the onsite number fluctuations. It provides new ways of studying the phase diagram. For example, the variance of the local chemical potential can be controlled through the trapping potential. In the trapped system, the density develops a plateau corresponding to integer filling fractions in the MI state and the width of the plateau is related to the width of the MI loops in the phase diagram [47]. It is also possible to directly observe the dynamics. In Refs. [45, 46], the atomic tunneling between the lattice site is directly recorded and the tunneling rate is measured for different lattice depths.

Chapter 2

Time evolving block decimation method

2.1 Basic TEBD method

2.1.1 State decomposition

The time evolving block decimation (TEBD) method is originally developed in the context of quantum information, as a method to simulate quantum computations that involve only a limited amount of entanglement [48]. In the context of quantum information, this method describes a chain of qubits coupled to their neighboring qubits. The total Hilbert space **H** is a product of the Hilbert space of each qubit, which are two-dimensional vector spaces with the qubit states, $|0\rangle$ and $|1\rangle$, as the orthonormal basis. The TEBD method is soon extended to simulate a wide range of one dimensional quantum many-body models outside quantum information and have shown to be an effective tool to study the static and dynamical properties of quantum many-body models [50].

Here, we discuss how the TEBD method is applied to simulate one-dimensional Hubbard-type models. The Hubbard-type models are similar with qubit systems in the sense that its Hilbert space **H** can be decomposed as a product of local Hilbert spaces,

$$\mathbf{H} = \otimes_{l=1}^{M} \mathbf{H}_l. \tag{2.1}$$

Here, l refers to the lth lattice site and M is the number of sites. The local Hilbert space at site l, $\mathbf{H}_l$, has a local dimension of d, $d = 2$ for fermionic systems and d is infinite for bosons. The orthonormal basis in **H** is expressed as the tensor product of the Fock state on each site, $|j_1\rangle|j_2\rangle\cdots|j_M\rangle$. Any state $|\Psi\rangle$ in $\mathbf{H}$ is represented as a superposition of the basis,

$$|\Psi\rangle \;=\; \sum_{j_1,j_2,\ldots,j_M=1}^{d} c_{j_1,j_2,\ldots,j_M}|j_1\rangle|j_2\rangle\cdots|j_M\rangle, \tag{2.2}$$

where $c_{j_1,j_2,\ldots,j_M}$ is the superposition coefficient. The dimension of the superposition coefficients grows like d^M and are very expensive to calculate for a large system. For example, in a system of 100 lattice sites with a local dimension of 2, the dimension of the Hilbert space is as large as $d^M = 2^{100} \sim 10^{33}$. It is necessary to introduce some kind of truncation that can greatly reduce the coefficient space, yet effectively simulate the system.

In the TEBD method, this truncation is inspired by the measure of entanglement. According to the Schmidt decomposition (SD), the decomposition of a state $|\Psi\rangle$with respect to the bipartite splitting of the system at site l, i.e. $[1,\ldots,l-1,l] : [l+1,l+2,\ldots,M]$ is written as

$$|\Psi\rangle \;=\; \sum_{\alpha_l=1}^{\chi_l} \lambda^{[l]}_{\alpha_l}|\Phi^A_{\alpha_l}\rangle|\Phi^B_{\alpha_l}\rangle. \tag{2.3}$$

Here, the vector $\lambda^{[l]}_{\alpha_l}$ and χ_l are the coefficients and rank of the Schmidt decomposition. The states $|\Phi^A_{\alpha_l}\rangle$ form an orthonormal basis for subsystem A of lattice sites $[1,\ldots,l-1,l]$. The states $|\Phi^B_{\alpha_l}\rangle$ form an orthonormal basis for subsystem B of lattice sites $[l+1,l+2,\ldots,M]$. The Schmidt coefficients $\lambda^{[l]}_{\alpha_l}$ satisfy

$$\sum_{\alpha_l}|\lambda_{\alpha_l}|^2 = 1 \tag{2.4}$$

and

$$\langle\Phi^A_{\alpha_l}|\Psi\rangle = \lambda^{[l]}_{\alpha_l}|\Phi^B_{\alpha_l}\rangle. \tag{2.5}$$

The Schmidt coefficients are closely related to the eigenvalues of the reduced density matrices of subsystems,

$$\rho_A = \mathrm{Tr}_{\mathrm{B}}(|\Psi\rangle\langle\Psi|) = \sum_{\alpha_l} \left|\lambda^{[l]}_{\alpha^l}\right|^2 |\Phi^A_{\alpha_l}\rangle\langle\Phi^A_{\alpha_l}|, \tag{2.6}$$

and

$$\rho_B = \mathrm{Tr}_{\mathrm{A}}(|\Psi\rangle\langle\Psi|) = \sum_{\alpha_l} \left|\lambda^{[l]}_{\alpha^l}\right|^2 |\Phi^B_{\alpha_l}\rangle\langle\Phi^B_{\alpha_l}|, \tag{2.7}$$

where Tr_{B} denotes the partial trace over subsystem B and Tr_{A} the partial trace over subsystem A.

The Schmidt rank χ_l is often regarded as a measure of entanglement in quantum information theory [51, 48]. Large values of χ_l usually means more entangled subsystems A and B. For $\chi_l = 1$, the state $|\Psi\rangle$ can be written as a tensor product of $|\Phi^A\rangle$ and $|\Phi^B\rangle$, which means subsystems A and B are *separable* (not entangled). For all possible bipartite splittings, the maximum possible value of χ_l is $d^{M/2}$, when the bipartite splitting is at the center of the system.

State decomposition: Based on the Schmidt decomposition, the TEBD method introduce the following way to decompose the state $|\Psi\rangle$ of Eq. 2.2,

$$\begin{aligned} c_{j_1,j_2,\ldots,j_M} &= \sum_{\alpha_1=1}^{\chi}\sum_{\alpha_2=1}^{\chi}\cdots\sum_{\alpha_{M-1}=1}^{\chi} \Gamma^{[1]j_1}_{\alpha_1}\lambda^{[1]}_{\alpha_1}\Gamma^{[2]j_2}_{\alpha_1\alpha_2}\lambda^{[2]}_{\alpha_2}\cdots \\ &\quad \times\lambda^{[M-2]}_{\alpha_{M-2}}\Gamma^{[M-1]j_{M-1}}_{\alpha_{M-2}\alpha_{M-1}}\lambda^{[M-1]}_{\alpha_{M-1}}\Gamma^{[M]j_M}_{\alpha_{M-1}}. \end{aligned} \tag{2.8}$$

This decomposition is composed of M tensors {$\Gamma^{[1]}$,..., $\Gamma^{[M]}$} and $M-1$ vectors {$\lambda^{[1]}$,..., $\lambda^{[M-1]}$}. The index j_l in $\Gamma^{[l]}$ corresponds to the local basis state $|j_l\rangle$ and take values in {1, ..., $d-1$} and the indices α_l in Γs and λs takes values in {1,..., χ}. Expect for $\Gamma^{[1]}$ and $\Gamma^{[M]}$, all Γs are rank-3 tensor with the dimension of $\chi \times d \times \chi$. The matrices $\Gamma^{[1]}$ and $\Gamma^{[M]}$ have the dimension of $\chi \times d$. The vector $\lambda^{[l]}$ has χ elements, which are ordered in a decreasing order, i.e. $\lambda^{[l]}_1 \geq \lambda^{[l]}_2 \geq \ldots \geq \lambda^{[l]}_\chi$. The total number of parameters in all Γs and λs is $(M-2)d\chi^2 + (M-1)\chi + 2d\chi$, which scales like $M(d\chi^2 + \chi)$ for large M.

For an arbitrary state $|\Psi\rangle$, χ can scale exponentially with M and the total number of parameters after the decomposition is comparable to d^M. However, for states where χ scales linearly with M, this decomposition requires only ploy(M) parameters and is much more efficient than the direct diagonalization. This means that the state decomposition in the TEBD method is efficient for a less entangled state, where the Schmidt rank $\chi \ll d^{M/2}$. Fortunately, for certain one dimensional many-body models, the ground state and low energy excitation states satisfy such condition. In [49], it is shown that the Schmidt coefficients $\lambda_\alpha^{[l]}$ decay roughly exponentially with index α for the ground and low energy excitation states,

$$\lambda_\alpha^{[l]} \sim \exp(-K\alpha). \tag{2.9}$$

This state decomposition directly gives the Schmidt decomposition. For a state $|\Psi\rangle$ represented by Eqs. 2.2 and 2.8, the Schmidt decomposition at site l is given by,

$$|\Psi\rangle = \sum_{\alpha_l=1}^{\chi} \lambda_{\alpha_l}^{[l]} |\Phi_{\alpha_l}^A\rangle |\Phi_{\alpha_l}^B\rangle, \tag{2.10}$$

where the states $|\Phi_{\alpha_l}^A\rangle$ and $|\Phi_{\alpha_l}^B\rangle$ are given by,

$$\begin{aligned} |\Phi_{\alpha_l}^A\rangle &= \sum_{\alpha_1=1}^{\chi} \sum_{\alpha_2=1}^{\chi} \cdots \sum_{\alpha_{l-1}=1}^{\chi} \Gamma_{\alpha_1}^{[1]j_1} \lambda_{\alpha_1}^{[1]} \Gamma_{\alpha_1\alpha_2}^{[2]j_2} \cdots \\ &\quad \times \lambda_{\alpha_{l-1}}^{[l-1]} \Gamma_{\alpha_{l-1}\alpha_l}^{[l]j_l} |j_1\rangle |j_2\rangle ... |j_l\rangle, \end{aligned} \tag{2.11}$$

and

$$\begin{aligned} |\Phi_{\alpha_l}^B\rangle &= \sum_{\alpha_{l+1}=1}^{\chi} \sum_{\alpha_{l+2}=1}^{\chi} \cdots \sum_{\alpha_{M-1}=1}^{\chi} \Gamma_{\alpha_l\alpha_{l+1}}^{[l+1]j_1} \lambda_{\alpha_{l+1}}^{[l+1]} \Gamma_{\alpha_{l+1}\alpha_{l+2}}^{[l+2]j_2} \cdots \\ &\quad \times \lambda_{\alpha_{M-1}}^{[M-1]} \Gamma_{\alpha_{M-1}}^{[M]j_M} |j_{l+1}\rangle |j_{l+2}\rangle ... |j_M\rangle. \end{aligned} \tag{2.12}$$

Besides its relationship with Schmidt decomposition, the state decomposition also provides an efficient way for local operations. In the following section, we discuss how local operations are carried out for the decomposed state.

2.1.2 Single-site and two-site operations

For most one-dimensional Hubbard-type models, the Hamiltonian is written as a sum of only single-site and two-site operations,

$$H = \sum_{l=1}^{M} H_l = \sum_{l=1}^{M} (K_l^{[1]} + K_l^{[2]}), \tag{2.13}$$

where $K_l^{[1]}$ is some single-site operator at site l and $K^{[2]}$ is some two-site operator that involves usually nearest-neighbor or next-nearest-neighbor sites. Here, we only discuss the single-site and double-site operations, but the method can be easily extended to the three- or higher-site operations. However, as we shall see in the discussion that the computational cost grows rapidly for higher-site operations. It is reasonable to expect that the TEBD method is most efficient for models with localized operations.

Single-site operation: For a single-site operator O at site l,

$$O = \sum_{j_l, k_l} O_{k_l}^{j_l} |j_l\rangle\langle k_l|, \tag{2.14}$$

only $\Gamma^{[l]}$ needs to be updated, and the new state is given by

$$\Gamma_{\alpha_{l-1}\alpha_l}^{[l]j_l} = \sum_{k_l=1}^{d} O_{k_l'}^{j_l} \Gamma_{\alpha_{l-1}\alpha_l}^{[l]k_1}. \tag{2.15}$$

Nearest-neighbor operation: For a operator Q of two neighboring sites, l and $l+1$,

$$Q = \sum Q_{k_l k_{l+1}}^{j_l j_{l+1}} |j_l\rangle|j_{l+1}\rangle\langle k_{l+1}|\langle k_l|, \tag{2.16}$$

we need to update the tensors $\Gamma^{[l]}$, $\Gamma^{[l+1]}$ and $\lambda^{[l]}$. To explain the update, we first rewrite the state $|\Psi\rangle$ into four state, the states before site l, on site l, on site $l+1$ and after site $l+1$:

1) an orthonormal basis for sites $[1 ... l-1]$ represented by $|\alpha\rangle$,

$$
\begin{aligned}
|\alpha\rangle &= \sum_{\alpha_1=1}^{\chi}\sum_{\alpha_2=1}^{\chi}\cdots\sum_{\alpha_{l-1}=1}^{\chi}\Gamma^{[1]j_1}_{\alpha_1}\lambda^{[1]}_{\alpha_1}\Gamma^{[2]j_2}_{\alpha_1\alpha_2}\cdots \\
&\quad\times\lambda^{[l-2]}_{\alpha_{l-1}}\Gamma^{[l-1]j_{l-1}}_{\alpha_{l-1}\alpha}|j_1\rangle|j_2\rangle...|j_{l-1}\rangle; \qquad (2.17)
\end{aligned}
$$

2) the Fock state basis for site l, $|j\rangle$;

3) the Fock state basis for site $l+1$, $|k\rangle$;

4) an orthonormal basis for sites $[l+2,...,M]$, represented by $|\gamma\rangle$,

$$
\begin{aligned}
|\gamma\rangle &= \sum_{\alpha_{l+2}=1}^{\chi}\sum_{\alpha_{l+3}=1}^{\chi}\cdots\sum_{\alpha_{M-1}=1}^{\chi}\Gamma^{[l+2]j_1}_{\gamma\alpha_{l+2}}\lambda^{[l+2]}_{\alpha_{l+2}}\Gamma^{[l+3]j_2}_{\alpha_{l+2}\alpha_{l+3}}\cdots \\
&\quad\times\lambda^{[M-1]}_{\alpha_{M-1}}\Gamma^{[M]j_M}_{\alpha_{M-1}}|j_{l+1}\rangle|j_{l+2}\rangle...|j_M\rangle. \qquad (2.18)
\end{aligned}
$$

Together, the state $|\Psi\rangle$ is written as

$$
|\Psi\rangle = \sum_{\alpha,\beta,\gamma=1}^{\chi}\sum_{j,k=1}^{d}\lambda^{[l-1]}_{\alpha}\Gamma^{[l]j}_{\alpha\beta}\lambda^{[l]}_{\beta}\Gamma^{[l+1]k}_{\beta\gamma}\lambda^{[l+1]}_{\gamma}|\alpha\rangle|j\rangle|k\rangle|\gamma\rangle. \qquad (2.19)
$$

If we introduce a rank-4 tensor

$$
\Theta^{jk}_{\alpha\gamma} = \sum_{\beta=1}^{\chi}\lambda^{[l-1]}_{\alpha}\Gamma^{[l]j}_{\alpha\beta}\lambda^{[l]}_{\beta}\Gamma^{[l+1]k}_{\beta\gamma}\lambda^{[l+1]}_{\gamma}, \qquad (2.20)
$$

the expression for $|\Psi\rangle$is further simplified as

$$
|\Psi\rangle = \sum_{\alpha,\gamma=1}^{\chi}\Theta^{jk}_{\alpha\gamma}|\alpha\rangle|j\rangle|k\rangle|\gamma\rangle. \qquad (2.21)
$$

Now when the two-site operator Q is applied, Q is acting on the rank-4 tensor Θ. Let $\widetilde{\Theta}$ be the updated and renormalized Θ after applying Q,

$$\widetilde{\Theta}^{jk}_{\alpha\gamma} = \frac{\sum_{j',k'} Q^{jk}_{j'k'} \Theta^{j'k'}_{\alpha\gamma}}{\left\| \sum_{j',k'} Q^{jk}_{j'k'} \Theta^{j'k'}_{\alpha\gamma} \right\|}. \tag{2.22}$$

To update $\Gamma^{[l]}$, $\Gamma^{[l+1]}$ and $\lambda^{[l]}$ one just need to find $\widetilde{\Gamma}^{[l]}$, $\widetilde{\lambda}^{[l]}$ and $\widetilde{\Gamma}^{[l+1]}$ that satisfy,

$$\widetilde{\Theta}^{jk}_{\alpha\gamma} = \sum_{\beta=1}^{\chi} \lambda^{[l-1]}_{\alpha} \widetilde{\Gamma}^{[l]j}_{\alpha\beta} \widetilde{\lambda}^{[l]}_{\beta} \widetilde{\Gamma}^{[l+1]k}_{\beta\gamma} \lambda^{[l+1]}_{\gamma}. \tag{2.23}$$

The new tensors $\widetilde{\Gamma}^{[l]}$, $\widetilde{\lambda}^{[l]}$ and $\widetilde{\Gamma}^{[l+1]}$can be found through the singular value decomposition (SVD) of $\widetilde{\Theta}$. Specifically, we construct a $\chi d \times \chi d$ matrix T,

$$T_{(j-1)\times\chi+\alpha,(k-1)\times\chi+\gamma} = \widetilde{\Theta}^{jk}_{\alpha\gamma} \tag{2.24}$$

and through the single value decomposition we obtain,

$$T = U \Lambda V^{*}, \tag{2.25}$$

where U is an $\chi d \times \chi d$ unitary matrix, Λ is an $\chi d \times \chi d$ diagonal matrix with non-negative real numbers on the diagonal, and V^{*} is the conjugate transpose of V, an $\chi d \times \chi d$ unitary matrix. The SVD is performed numerically with only the first χ columns of U, the first χ diagonal elements of Λ (in decreasing order) and the first χ rows of V as the output result,

$$T_{(j-1)\times\chi+\alpha,(k-1)\times\chi+\gamma} \quad = \sum\nolimits_{\beta=1}^{\chi} \quad U_{(j-1)\times\chi+\alpha,\beta} \Lambda_{\beta} V_{\beta,(k-1)\times\chi+\gamma}. \tag{2.26}$$

The values of $\widetilde{\Gamma}^{[l]j}_{\alpha\beta}$, $\widetilde{\lambda}^{[l]}_{\beta}$, $\widetilde{\Gamma}^{[l+1]}_{\beta\gamma}$ are determined as,

$$\widetilde{\Gamma}^{[l]j}_{\alpha\beta} = \frac{U_{(j-1)\times\chi+\alpha,\beta}}{\lambda^{[l-1]}_{\alpha}},\ \widetilde{\lambda}^{[l]}_{\beta} = \Lambda_{\beta},\ \widetilde{\Gamma}^{[l+1]}_{\beta\gamma} = \frac{V_{\beta,(k-1)\times\chi+\gamma}}{\lambda^{[l+1]}_{\gamma}}. \tag{2.27}$$

Next-nearest-neighbor operator: In the TEBD simulation, the next-neighboring operator cannot directly be apply to its corresponding sites, instead the site in between should also be included. To apply one next-neighboring operator as a two-site operator while maintaining the tensor product sequence in Eq. 2.8, totally three nearest-neighbor operations are needed. To illustrate the three operations, let's assume V be an operator acting on site l and $l+2$,

$$V = \sum_{k_l, k_{l+2}=1}^{d} V^{j_l j_{l+2}}_{k_l k_{l+2}} |j_l\rangle |j_{l+2}\rangle \langle k_{l+2}| \langle k_l|. \tag{2.28}$$

The three steps of applying V on the state $|\Psi\rangle$are:

1) Exchange the state at site $l+1$ with the state at site $l+2$ by applying the swapping operator at the site $l+1$. The swapping operator at an arbitrary site l is defined as

$$Q^{[l]}_{swap} = \sum_{j'_l, j_l, j'_{l+1}, j_{l+1}} \delta_{j_l, j'_{l+1}} \delta_{j_l, j'_{l+1}} |j_l\rangle |j_{l+1}\rangle \langle j'_{l+1}| \langle j'_l|, \tag{2.29}$$

where $\delta_{x,y}$ is the Dirac delta function $\delta(x-y)$. Since the swapping operator is a nearest-neighbor operator, it is directly applied to the state.

2) Apply V as a nearest-neighbor operator on the *swapped* state (note now the state at site $l+1$ corresponds to the state at site $l+2$ before the swapping),

$$V = \sum_{k_l, k_{l+2}=1}^{d} V^{j_l j_{l+2}}_{k_l k_{l+2}} |j_l\rangle |j_{l+1}\rangle \langle k_{l+1}| \langle k_l|. \tag{2.30}$$

3) Exchange the updated state at site $l+1$ with the state at site $l+2$ again by applying the swapping operator $Q^{[l+1]}_{swap}$.

After the three steps, we effectively apply V onto the state at site l and at site $l+2$. Note that the stat at site $l+1$ is also updated as a result of swapping. For further discussion, see also Ref. [52].

2.1.3 Time evolution

In the TEBD method, both the ground state and the dynamic calculation are based on the application of the time evolution operator, or the propagator, which is decomposed into a series of local operations. This can be done because the Hamiltonian consists only local operations, i.e.

$$H = \sum_l H_{l,l+s}, \tag{2.31}$$

where s is the number of sites around site l. If $s = 1$, the Hamiltonian involves only single-site and nearest-neighbor operations. If $s = 2$, the Hamiltonian involves single-site, nearest-neighbor and next-nearest-neighbor operations. To illustrate the basic steps involved in the time-evolution simulation, we will first explain the case of $s = 1$, where the Hamiltonian involves only single-site and nearest-neighbor operation.

Let the time propagator be $\exp(-iHt)$ with the Plank constant $\hbar = 1$. Because $H_{l,l+1}$ does not necessarily commute with each other, the time propagator can not be written directly as a product of $\exp(-iH_{l,l+1}t)$,

$$\exp(-iHt) = \exp(-i\sum_l H_{l,l+1}t) \neq \prod_l \exp(-iH_{l,l+1}t). \tag{2.32}$$

But notice that $H_{l,l+1}$ and $H_{l+2,l+3}$ always commute with each other. If we divide the Hamiltonian into the even site part H_{even} and the odd site part H_{odd},

$$H = H_{even} + H_{odd} = \sum_{even\, l} H_{l,l+1} + \sum_{odd\, l} H_{l,l+1}. \tag{2.33}$$

every $H_{l,l+1}$ commutes with each other within H_{even} and H_{odd}. Using the second order Suzuki-Trotter expansion [54] we can rewrite the propagator for a very short time δt as follows,

$$\begin{aligned} \mathrm{e}^{-iH\delta t} &= \mathrm{e}^{-iH_{odd}\delta t/2}\mathrm{e}^{-iH_{even}\delta t}\mathrm{e}^{-iH_{odd}\delta t/2} + O(\delta t^3). \\ &= \prod_{odd\, l} \mathrm{e}^{-iH_{l,l+1}\delta t/2} \prod_{even\, l} \mathrm{e}^{-iH_{l,l+1}\delta t} \prod_{odd\, l} \mathrm{e}^{-iH_{l,l+1}\delta t/2} + O(\delta t^3). \end{aligned} \tag{2.34}$$

In this way, $\exp(-iH\delta t)$ is decomposed into a product of local operations $\mathrm{e}^{-iH_{l,l+1}\delta t}$, each of which can be applied onto the state $|\Psi\rangle$through a nearest-neighbor operation. For our calculation, δt is on the order of 0.01 and the error introduced by this expansion is on the order of 10^{-6}. To further reduce the error, one use higher-order Suzuki-Trotter expansions [54].

Imaginary-time evolution: the imaginary time propagation method states that the ground state is the state that the imaginary-time evolution of a superposition of eigenstates converges into as the imaginary time, $\tau = -\mathrm{i}t$, goes to infinite,

$$|\Psi\rangle_{gs} = \lim_{\tau \to \infty} \frac{\exp(-H\tau)|\Psi_{int}\rangle}{\|\exp(-H\tau)|\Psi_{int}\rangle\|}. \tag{2.35}$$

In the TEBD method, the initial superposition of eigenstates can either be the input state, or the state after applying the propagator with a very large $\delta t \sim 10$. We assume such states are a superposition of many eigenstates, including the ground state, of the system.

2.1.4 Observables

To numerically study the static and dynamical properties, it is essential to calculate various quantities, such as the total energy , the density distribution and varies correlation functions. Generally speaking, there are two ways for calculating the quantities in the TEBD method: 1) through calculating reduced density matrix and 2) through the inner tensor product. For quantities that involve only single-site or local sites, it is often more efficient to calculate it through the reduced density matrix. For quantities that involves many sites or far-apart sites, the inner tensor product of the whole state is more efficient. As an example, we explain the calculation of the energy E, the density distribution $\rho(x)$ and the correlation functions. The calculation of other quantities can be easily extended from the examples.

Single-site observables: for the density distribution and other single-site observables, they are calculated through the reduced density matrix at the corresponding site. Let ρ_l be the reduced density of state at site l, ρ_l is directly calculated from $\Gamma^{[l]}$, $\lambda^{[l]}$and $\Gamma^{[l+1]}$,

$$\rho_l = \sum_{\alpha_j, \alpha_{j+1}} \lambda^{[l]}_{\alpha_j} \Gamma^{[l]j_l}_{\alpha_j \alpha_{j+1}} \lambda^{[l+1]}_{\alpha_{j+1}} (\lambda^{[l]}_{\alpha_j} \Gamma^{[l]j'_l}_{\alpha_j \alpha_{j+1}} \lambda^{[l+1]}_{\alpha_{j+1}})^* |j_l\rangle\langle j'_l|. \tag{2.36}$$

The density $n(x)$ at site l is then calculated as

$$n(x) = \langle\Psi|\hat{n}_l|\Psi\rangle = \mathrm{Tr}(\hat{n}_l \rho_l), \tag{2.37}$$

where $\hat{n}_l$ is the number operator at the site l.

Two-site observables: For the total energy E and other observables that involves only neighboring site operators, the calculation is based on the reduced two-site density matrix, $\rho_{l,l+1}$, which can be written in terms of the rank-4 tensor Θ in Eq. 2.20 ,

$$\rho_{l,l+1} = \sum_{\alpha_l,\alpha_{l+2}} \Theta^{j_l j_{l+1}}_{\alpha_l \alpha_{l+2}} \left(\Theta^{j'_l j'_{l+1}}_{\alpha_l \alpha_{l+1}}\right)^* |j_l\rangle|j_{l+1}\rangle\langle j'_{l+1}|\langle j'_l|. \tag{2.38}$$

The total energy E is a sum of local two-site operations over all lattice sites,

$$E = \sum_l E_l = \sum_l \langle\Psi|H_{l,l+1}|\Psi\rangle = \mathrm{Tr}(H_{l,l+1}\rho_{l,l+1}). \tag{2.39}$$

For an observable involving sites l and $l+k$, where $k > 1$, the reduced two-site density of state can be found as a inner product of the Γs and λs between l and $l+k$. For very large k, this calculation can be numerically expensive.

Correlation functions: for the calculation of the correlation function $\langle O^\dagger_{l_1} O_{l_2}\rangle$, one first apply the single-site operator O_{l_2} onto $|\Psi\rangle$which updates the state to $|\Psi_1\rangle$ (non-normalized) and then apply $O^\dagger_{l_1}$ onto $|\Psi_1\rangle$ and update the state to $|\Psi_2\rangle$. The correlation function is then the tensor inner product between $|\Psi\rangle$ and $|\Psi_2\rangle$,

$$\langle\Psi|O^\dagger_{l_2} O_{l_1}|\Psi\rangle = \langle\Psi|O^\dagger_{l_1}|\Psi_1\rangle = \langle\Psi|\Psi_2\rangle, \tag{2.40}$$

where

$$|\Psi_1\rangle = O_{l_1}|\Psi\rangle,\ |\Psi_2\rangle = O^\dagger_{l_2}|\Psi\rangle. \tag{2.41}$$

This method can be easily adapted for n^{th} order correlation functions, $\langle\Psi|O^\dagger_{l_n} O_{l_{n-1}} ....O^\dagger_{l_2} O_{l_1}|\Psi\rangle$, by applying operators in the sequence of O_{l_1} , $O^\dagger_{l_2}$, .., $O_{l_{n-1}}$, , $O^\dagger_{l_n}$onto $|\Psi\rangle$,

$$\begin{aligned}\langle\Psi|O^{\dagger}_{l_n}O_{l_{n-1}}....O^{\dagger}_{l_2}O_{l_1}|\Psi\rangle &= \langle\Psi|O^{\dagger}_{l_n}O_{l_{n-1}}...O^{\dagger}_{l_2}\left(O_{l_1}|\Psi\rangle\right) \\ &= \langle\Psi|O^{\dagger}_{l_n}O_{l_{n-1}}...\left[O^{\dagger}_{l_2}\left(O_{l_1}|\Psi\rangle\right)\right] \\ &... \\ &= \langle\Psi|\left\{O^{\dagger}_{l_n}O_{l_{n-1}}...\left[O^{\dagger}_{l_2}\left(O_{l_1}|\Psi\rangle\right)\right]\right\}. \end{aligned} \tag{2.42}$$

In our calculation, this method have been applied to calculate the pairing, anti-pairing and the four point correlations. Now, we have explained all basic components of the TEBD method and in the next subsection, we will discuss some of additional methods to improve the efficiency and extend the application.

2.2 Extended TEBD method

2.2.1 Number conservation

In the TEBD method, the computational cost is mainly determined by the size of the truncated Hilbert space. The truncated Hilbert space can be further reduced by taking into account the existence of conserved quantities in the studied systems. In our work, we are interested in the ultra-cold atoms in a confined lattice system, it is reasonable to assume that the total number of atoms in the system is conserved. Here we briefly describe how the number conservation can be implemented in the TEBD method.

In the Bose-Hubbard model, the orthonormal basis for the local Hilbert space at an arbitrary site l is the Fock state $|j_l\rangle$, where j_l corresponds to the number of particles at site l. Let the total number to be fixed be at $\mathcal{N}$, the number conservation require that the orthonormal basis for the system, $|j_1\rangle|j_2\rangle...|j_M\rangle$, satisfy $\sum_l j_l = \mathcal{N}$. This is easy to satisfy for the input state in the TEBD method. The question is how to preserve the number conservation through the time propagation. Now because the propagation is decomposed into a series of local two-site operations (see Eq. 2.34), the number conservation is preserved as long as the two-site operation conserves the total number of particles.

To implement the number conservation in the two-site operation, it is obvious that the local two-site Hilbert space should only contain the states whose particle number equals to the total particle number $\mathcal{N}$ minus the particle number of the rest of the lattice. Now the problem here is that the local states are linked with the states on the left and right through tensor products. The numbers of particles on the right and left are not numbers, but a vector. To illustrate this problem, let us first label the lattice sites from the left to right with numbers 1, 2, 3,....M and consider a two-site operation at an arbitrary site l. The state $|\Psi\rangle$ is written as product of states $|\alpha\rangle$, $|j\rangle$, $|k\rangle$, $|\gamma\rangle$ as in Eq. (2.21).

Let $NL^{[l]}(\alpha)$ be the total number of particles in state $|\alpha\rangle$and let $NR^{[l+1]}(\gamma)$ be the total number of particles in state $|\gamma\rangle$. The vector $NL^{[l]}$ contains all the possible total number of the particles on the *left* of site l and the vector $NR^{[l+1]}$ contains all the possible total number of the particles on the *right* of site $l+1$. The states $|j\rangle$ and $|k\rangle$ must satisfy

$$j + k + NL^{[l]}(\alpha) + NR^{[l+1]}(\gamma) = \mathcal{N}. \tag{2.43}$$

Now let the total number of particles in state $|\alpha\rangle$and state $|j\rangle$ be $N_J(\alpha, j) \equiv j + NL^{[l]}(\alpha)$ and the total number of particles in state $|\gamma\rangle$and state $|k\rangle$ be $N_K(\alpha, k) = k + NR^{[l]}(\alpha)$. The biggest and smallest possible value in N_1 are

$$\begin{aligned} N_{J,M} &= \max\left[N_J(\alpha, j)\right] = \min\left[\max(NL^{[l]}) + (d-1), \mathcal{N} - \min(NR^{[l+1]})\right], && (2.44) \\ N_{J,m} &= \min\left[N_J(\alpha, j)\right] = \max\left[\min(NL^{[l]}), \mathcal{N} - \max(NR^{[l+1]})\right]; && (2.45) \end{aligned}$$

where d is the local dimension for all sites. Similarly, we find the biggest and smallest possible values of N_2 are

$$\begin{aligned} N_{K,M} &= \max\left[N_K(\lambda, k)\right] = \min\left[\max(NR^{[l]}) + (d-1), \mathcal{N} - \min(NL^{[l+1]})\right], && (2.46) \\ N_{K,m} &= \min\left[N_K(\lambda, k)\right] = \max\left[\min(NR^{[l]}), \mathcal{N} - \max(NL^{[l+1]})\right]. && (2.47) \end{aligned}$$

There are totally $(N_{J,M} - N_{J,m} + 1)$ possible values for the total particle number for state

$|\alpha\rangle$ and state $|j\rangle$combined. We therefore reconstruct $\widetilde{\Theta}$ into $(N_{J,M} - N_{J,m} + 1)$ matrices, $B^{[v]}$, where $v = 1, 2.., (N_{J,M} - N_{J,m} + 1)$. The matrix element $B^{[v]}_{mn}$ is equal to $\widetilde{\Theta}^{j_m k_n}_{\alpha_m \gamma_n}$ where $\{j_m, \alpha_m, k_n, \gamma_n\}$ be the m^{th} combination of j and α that satisfy $j + NL^{[l]}_{\alpha} = v + N_{J,m} - 1$ and the n^{th} combination of k and γ that satisfy $k + NR^{[l]}_{\gamma} = \mathcal{N} - v - N_{J,m} + 1$. We also store the indices $\{j_m, \alpha_m, k_n, \gamma_n\}$ in matrices $LL^{[v]}$ and $LR^{[v]}$ as

$$LL^{[v]}_{m,1} = j_m,\ LL^{[v]}_{m,2} = \alpha_m,\ LR^{[v]}_{n,1} = k_n,\ LR^{[v]}_{n,2} = \alpha_n. \tag{2.48}$$

The SVD of $B^{[v]}$ yields a series of unitary matrices $U^{[v]}$, $V^{[v]}$ and the diagonal matrices $S^{[v]}$ whose diagonal elements are the single values for $B^{[v]}$,

$$B^{[v]} = U^{[v]} S^{[v]} V^{[v]*}. \tag{2.49}$$

Now, we have a series of matrices $S^{[v]}$ whose diagonal elements are the values for $\widetilde{\lambda}^{[l]}$. But we cannot assign the values in $S^{[l]}$ to $\widetilde{\lambda}^{[l]}$ arbitrarily, because the elements in $\widetilde{\lambda}^{[l]}$ *must* be in the decreasing order. In other words, the value of $\widetilde{\lambda}^{[l]}_{\beta}$ can only be β^{th} largest value in all $S^{[l]}$s. Its corresponding column vectors in $U^{[v]}$ and $V^{[v]}$ should be used to update $\widetilde{\Gamma}^{[l]j}_{\alpha\beta}$ and $\widetilde{\Gamma}^{[l]k}_{\beta\gamma}$.

To satisfy this requirement, $\widetilde{\lambda}^{[l]}_{\beta}$, $\widetilde{\Gamma}^{[l]j}_{\alpha\beta}$ and $\widetilde{\Gamma}^{[l+1]k}_{\alpha\beta}$ are determined in the following way. First, let us assume $S^{[y]}_{x}$ is the β^{th} largest element in all $S^{[v]}$. We then immediately have

$$\widetilde{\lambda}^{[l]}_{\beta} \quad = \quad S^{[y]}_{x}. \tag{2.50}$$

The x^{th} column of matrix $U^{[y]}$ is then used to update $\Gamma^{[l]j}_{\alpha\beta}$,

$$\Gamma^{[l]j}_{\alpha\beta} = \frac{U^{[y]}_{mx}}{\lambda^{[l-1]}_{\alpha}} \tag{2.51}$$

where the indices j and α are determined by $LL^{[y]}$,

$$j = LL^{[y]}_{m,1},\ \alpha = LL^{[y]}_{m,2}. \tag{2.52}$$

Similarly, the x^{th} row of matrix $V^{[y]*}$ is used to update $\Gamma^{[l+1]k}_{\beta\gamma}$,

$$\Gamma^{[l+1]k}_{\beta\gamma} = \frac{V^{*[y]}_{xn}}{\lambda^{[l+1]}_{\gamma}}, \tag{2.53}$$

where the indices k and γ are determined by $LR^{[y]}$,

$$k = LR^{[y]}_{n,1},\ \gamma = LR^{[y]}_{n,2}. \tag{2.54}$$

For the elements in $\widetilde{\lambda}^{[l]}$, $\widetilde{\Gamma}^{[l]}$ and $\widetilde{\Gamma}^{[l+1]}$ that are not updated in the above procedure, they are all set to zero. Tensors $\widetilde{\lambda}^{[l]}$, $\widetilde{\Gamma}^{[l]}$ and $\widetilde{\Gamma}^{[l+1]}$ are the updated $\lambda^{[l]}$, $\Gamma^{[l]}$ and $\Gamma^{[l+1]}$ and the number conserved two-site operation is completed. Repeat the procedures for each application of $\exp(-iH_{l,l+1}\delta t)$, the total number is conserved during the whole time propagation operation.

2.2.2 One dimensional two-component Hamiltonian

The straightforward way of presenting the two-component system is to double the local Hilbert space dimension, but this is not favorable because of the high computational cost for increasing the local dimension. A more efficient way is to map the two-component Bose-Hubbard model (Eq. 3.1) onto the one-component Hamiltonian with next-nearest-neighbor hoppings and nearest-neighbor interactions,

$$\begin{aligned} H &= -t\sum_{l=1}^{2N-2}(b_l^\dagger b_{l+2} + \text{h.c.}) + U_{12}\sum_{\text{odd}\, l} n_l n_{l+1} \\ &\quad + \frac{U}{2}\sum_{l=1}^{2N} n_l(n_l - 1), \end{aligned} \tag{2.55}$$

where N is the number of sites in the original two-species Hamiltonian. In this one-species Hamiltonian, there are $2N$ sites, each of which is indexed by l. The odd sites l correspond to species 1 and the even sites to species 2. Hopping between neighboring sites $-t\, b^{\dagger}_{a,i} b_{a,i+1}$ in Eq. 3.1 is mapped onto a next-nearest-neighbor hopping $-t\, b^{\dagger}_{l} b_{l+2}$ in Eq. 2.55. Similarly, the inter-species onsite-interaction $U_{12} n_{1,i} n_{2,i}$ is mapped onto the nearest-neighbor interaction $U_{12} n_l n_{l+1}$. This type of mapping has been successfully applied to treat the two-legged Bose-Hubbard model [53].

The reason why the mapping reduces the cost is explained as follows. The cost in the TEBD method scales as $Md^3\chi^3$. For the two-species system with N sites, $M = N$, and with a local dimension of D for each species, i.e. $d = D^2$ for two species, the cost scales as $MD^6\chi^3$. On the other hand, for the mapped Hamiltonian with $2N$ sites, $M = 2N$, and with a local dimension of D, the cost only scales as $2ND^3\chi$. In our calculation, we set $d = 3$ or 5. The mapping makes the computation five to ten times faster.

To apply the time propagation of the mapped Hamiltonian, we need to split the Hamiltonian into three parts as $H = H_{\text{int}} + H^{\text{odd}}_{\text{hop}} + H^{\text{even}}_{\text{hop}}$, where

$$\begin{aligned}
H_{\text{int}} &= \sum_{m=1}^{N} \left[U_{12} n_{2m-1} n_{2m} + U n_{2m-1}(n_{2m-1} - 1) \right. \\
&\quad \left. + U n_{2m}(n_{2m} - 1) \right], \qquad (2.56) \\
H^{\text{odd}}_{\text{hop}} &= -t \sum_{\text{odd}\, m} (b^{\dagger}_{2m-1} b_{2m+1} + b^{\dagger}_{2m} b_{2m+2} + \text{h.c.}), \\
H^{\text{even}}_{\text{hop}} &= -t \sum_{\text{even m}} (b^{\dagger}_{2m-1} b_{2m+1} + b^{\dagger}_{2m} b_{2m+2} + \text{h.c.}).
\end{aligned}$$

Subsequently, we use the second-order Suzuki-Trotter expansion to decompose $e^{-i\hat{H}\delta}$ as

$$\begin{aligned}
e^{-iH\delta} &= e^{-iH_{\text{int}}\delta/2} e^{-iH^{\text{odd}}_{\text{hop}}\delta/2} e^{-iH^{\text{even}}_{\text{hop}}\delta} e^{-iH^{\text{odd}}_{\text{hop}}\delta/2} \\
&\quad \times e^{-iH_{\text{int}}\delta/2} + O(\delta^3), \qquad (2.57)
\end{aligned}$$

Each of the operators $e^{-iH_{\text{int}}\delta/2}$, $e^{-iH^{\text{odd}}_{\text{hop}}\delta/2}$, and $e^{-i\hat{H}^{\text{even}}_{\text{hop}}\delta}$ can be decomposed into a product of two-site operators, which can be efficiently applied to the matrix product state $|\Psi\rangle$.

We use swapping techniques to apply the next-nearest-neighbor operators $e^{-iH_{\text{hop}}^{\text{odd}}\delta/2}$ and $e^{-i\hat{H}_{\text{hop}}^{\text{even}}\delta}$.

2.3 Efficiency and accuracy estimation

Based on our previous discussion on the TEBD method, it is easy to see that the complexity of the TEBD method is proportional to $\sim M\chi^3 d^2$, where M is the system-size and $\chi^3 d^2$ is the complexity of a two-site operation. For a given system-size and a local dimension, the computational cost of the TEBD method depends largely on the value of χ. To reduce the computational cost, it is ideal to set $\chi$to a small value.

From the viewpoint of accuracy, larger χ is favorable because it includes more entangled states into the decomposition. In fact, for a system of system-size M and fixed local dimension d, the TEBD method is exact if χ is fixed at the maximum value of $d^{M/2}$. But this value of χ makes the TEBD method even less efficient than direct diagonalization. The optimal value of χ is crucial for achieving the desired accuracy with minimum computational cost. Usually, we determine the accuracy by studying the dependence of $\lambda_\alpha$on α. Numerically, we find that λ_α decreases very fast as α increases. For the value of χ chosen in our calculation, the value of $|\lambda_\chi|$ is less than 10^{-12}.

For models involving bosonic particles, where a cut-off is needed for the local dimension d, the accuracy of the calculation also depends on the value of d. The accuracy can be estimated by compare the calculations with local dimensions of d and $d+1$. When d is large enough for the state considered, there is very small difference in the calculation results between d and $d+1$.

2.4 Example: one-dimensional Bose Hubbard model

To demonstrate the capabilities of the TEBD method, we would like to discuss the computation of the ground state of one dimensional Bose-Hubbard model in different parameter regions. As explained in Chap. 1, the model is written in terms of the bosonic creation and annihilation operators $b_i^\dagger$ and b_j for particles on site j,

$$H = -t\sum_{j=1}^{M-1}(b_j^\dagger b_{j+1} + h.c.) + \sum_{j=1}^{M} U n_j(n_j - 1) - \sum_{j=1}^{M}\left[\mu - \Omega(j - j_c)^2\right] n_j. \tag{2.58}$$

Here we assume a closed lattice system of M lattice sites and the lattice constant a. The operator n_j is the number operator on site j, $n_j = b_j^\dagger b_j$; The parameter t is the hopping parameter, U is the onsite interaction parameter. As a result of the implementation of the total number conservation, the chemical potential μ is set to zero. Instead, we use $\mathcal{N}$ to present the total number of the particles in the system. The term $\Omega(j - j_c)^2$ corresponding to the harmonic trap that is located at the center of the lattice, $j_c = (M + 1)/2$.

As is discuss in the previous chapter, there are two phases that exist in the Bose-Hubbard model: Mott insulator (MI) and superfluid (SF). In this section, we will discuss the TEBD calculation of the ground state in the MI and SF regions in one dimension. We will show the calculation of the one body density matrix $G_{i,j} = \langle b_i^\dagger b_j \rangle$, the momentum distribution $n(k)$ and the on-site number fluctuations $\Delta_j = \sqrt{(n_j - \langle n_j \rangle)^2}$.

2.4.1 Homogeneous System

when the trap frequency $\Omega = 0$, the model corresponding to a homogeneous lattice system with hard-wall boundary conditions. In the SF region, the number fluctuations is very high. The asymptotic behavior of the one-body reduced density matrix, $G_{ij} = \langle b_i^\dagger b_j \rangle$, is algebraic, $G_{ij} \sim |i - j|^{-1/K}$, where K is the Luttinger parameter (Chapter 1). In the MI region, the number fluctuation is low and the Green's function decays rapidly. The asymptotic behavior of G_{ij} is exponential, $G_{ij} \sim \exp(-\alpha|i - j|)$, where α is the decay constant. As an example, we choose a system of 50 lattice sites and totally 50 particles. The local dimension for each site d is 5, which corresponds to the maximum occupation number of 4. The parameter $\chi$is set to 50.

In Fig. 2.1, we show the behavior of the number fluctuation, and density distribution, $\langle n_j \rangle$, as a function of location j in the SF and MI region. The density is at unit filling for both cases, while the fluctuation in the SF region is much higher than the one in the MI

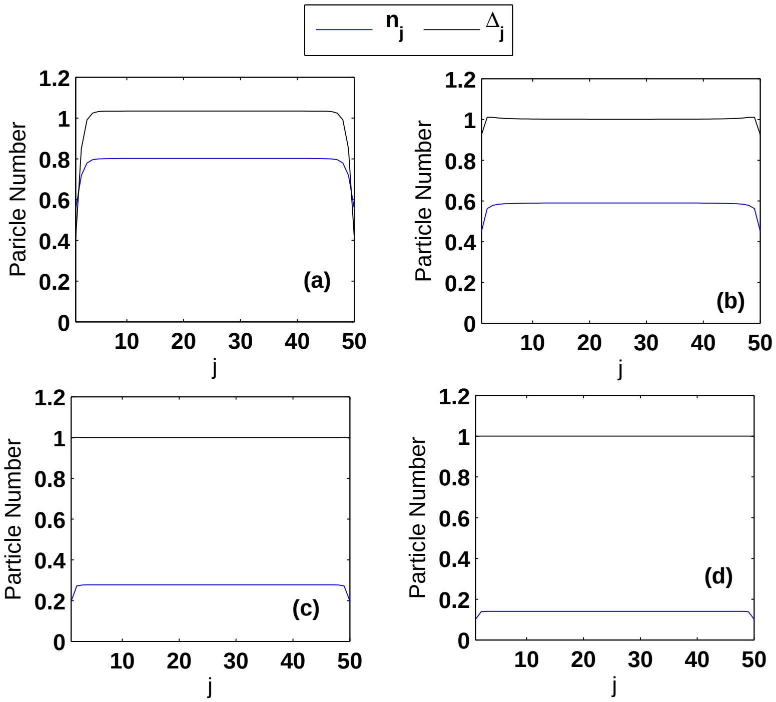

Figure 2.1: Number fluctuations Δ_j and density distribution $\langle n_j \rangle$ for $U/t = 1$(a), 4(b), 10(c), 20(d). The total number of particle is 50. The density distribution is uniformly 1 except for at the boundary. In (a) and (b), the system is in the SF state, this is reflected by the large number fluctuation. In (c) and (d), the system is in the MI state and the number fluctuations are much reduced.

region. In Fig. 2.2 and 2.3, we discuss the behavior of the one body reduced density matrix for U/t =1, 2, 10 and 20. For $U/t = 1$ and 2, the system is in the SF state. In both cases, G_{ij} decays algebraically. For $U/t = 2$, G_{ij} has a larger decay power. This is the result of the increased U/t in (b) compared with (a). As U/t continues to increase, G_{ij} becomes short-ranged and the decay behavior changes to exponential. This is the case for $U/t = 10$ and 20, where the system is in the MI state. In Fig. 2.3, we study the decay behavior of G_{ij} by considering $i = 25$ and $j = 25, 26, ..50$. We can use the power law and exponential fit function to extract the decay parameters. From the decay power, one can determine the Luttinger parameter K. We find that K decreases as U/t increases till around 2, where the transition to MI happens and the decay behavior changes to the exponential decay. In the MI region, G_{ij} decays very fast from the diagonal $j = i$. This decay can approximated by a exponential function, $\exp(-\alpha x)$. The decay constant α becomes bigger for stronger U/t.

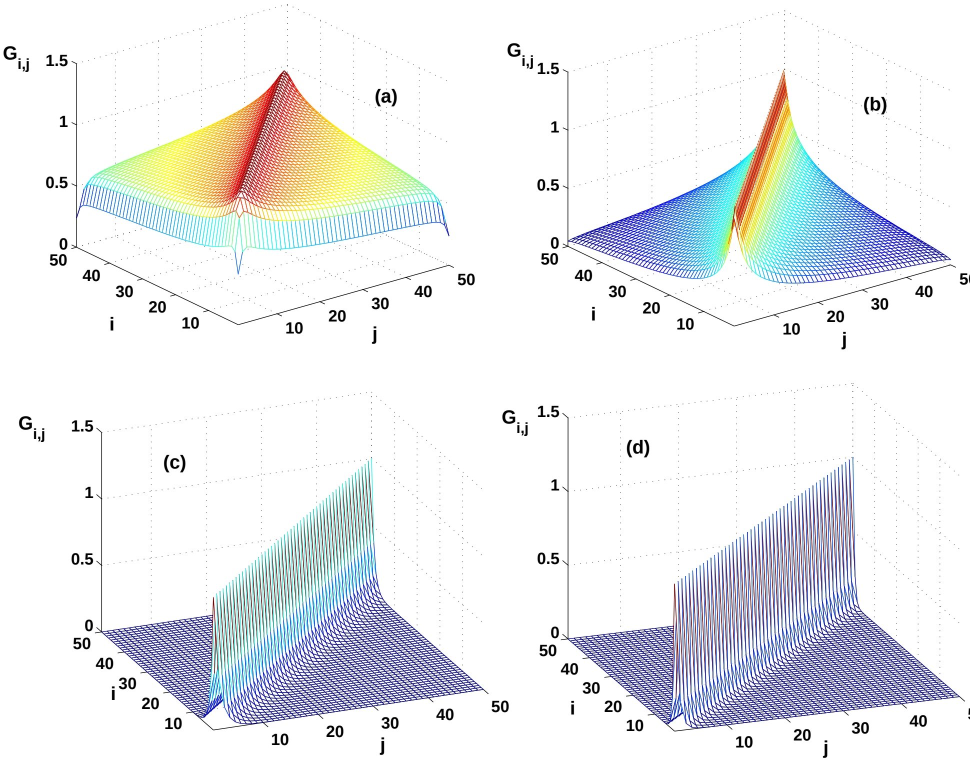

Figure 2.2: One-body density matrix $G_{ij} = \langle b_i^\dagger b_j \rangle$ for $U/t = 1$(a), 4(b), 10(c) and 20(d). The parameters are the same as in Fig. 2.1. In (a) and (b) the system is in the SF state. In (c) and (d) the system is in the MI state. In (a), G_{ij} decays very slowly and the correlation function is forced to zero by the boundary condition at the edge of the lattice. In (b), G_{ij} decays faster than in (a) but still qualifies as algebraic decay (see also Fig. 2.3) with a larger decay power. In (c) and (d), G_{ij}becomes short-ranged and the decay behavior changes to exponential.

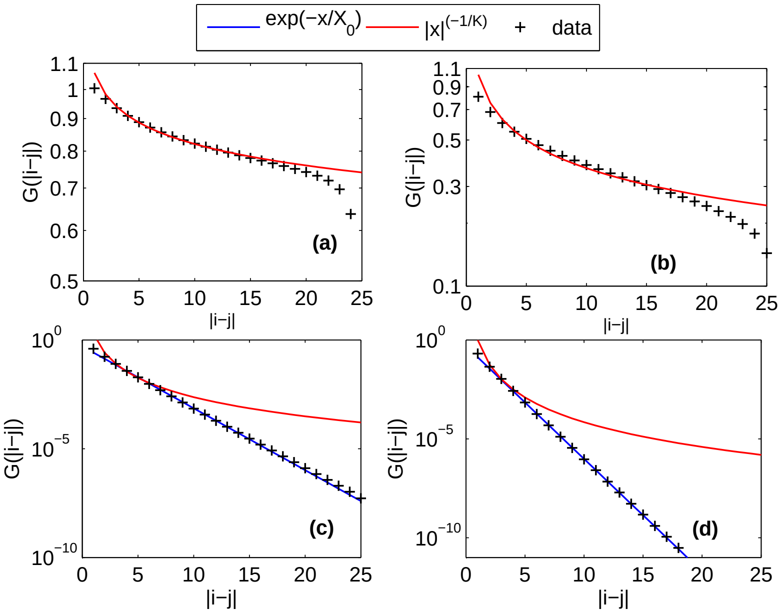

Figure 2.3: Algebraic and exponential fit for G_{ij}. Here we choose $i = 25$, $j = 25, ...50$. The function $G_{25,j}$ represent the decay behavior of the off-diagonal one body density matrix. Through the fit, one can obtain the Luttinger parameter K, $K = 9.4$ in (a) and $K = 6.4$ in (b). The decay length X_0 can be found for the exponential decay, $X_0 = 1.5$ in (c) and $X_0 = 0.75$ in (d).

2.4.2 Harmonic trap

The trap introduces a local potential variance on each site. To understand the effect of the local potential, one can use the local density approximation and treat local potential variance as the chemical potential at site j, $\mu_j = \mu - \Omega(j - j_c)^2$. The state at site j is then the state of the homogeneous system with chemical potential of $\mu - \Omega(j - j_c)^2$ and the same U and t. In the SF-MI phase diagram, the MI state exists within lobes of $\mu$and t/U. In each of the MI lobe, the density is fixed as a integer filling as μchanges. This means that the local compressibility $\partial n/\partial \mu_j$ should be zero. In other words, in MI state, the density is held at an integer filling despite of the trap. The density in the SF state on the other hand will vary over lattice sites and reflect the trap potential.

In Figs. 2.4 and 2.5, we show the number fluctuations, the density distribution and one body density matrix for the trapped system at $U/t = 1$ and $U/t = 20$. The parameters for this calculation is $\Omega = 0.016$ and $\mathcal{N} = 25$. The trap frequency is strong enough to confine the particle within the trapping potential and hard-wall boundary conditions can

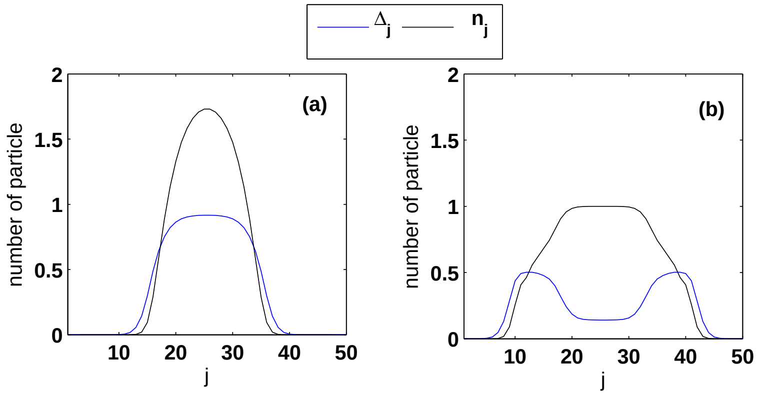

Figure 2.4: Density distribution and number fluctuations in a trapped system. In (a), the system is in the SF state with $U/t = 1$ In (b), the interaction is strong, $U/t = 20$. The density forms a plateau near the center of the trap. This is where the MI state is formed. The fluctuations are reduced at the plateau area as the result of the MI order. The SF state still exists at the edge of the trap.

be neglected. For $U/t = 1$, the whole system is in a SF state. The number fluctuation is high [Fig. 2.4 (a)] and the function $G_{i,j}$ shows long-range correlation [Fig. 2.4 (b)]. For $U/t = 20$, the MI state is at the center of trap, while the SF state is in the edge. The incompressibility of the MI state leads to the plateau at the center of the trap in the density distribution [Fig. 2.4 (b)]. The difference between the MI and SF states can be seen behavior of the number fluctuation in Fig. 2.4 (b) and in the one-body density matrix $G_{i,j}$ in Fig. 2.5 (b).

2.4.3 Accuracy estimation

As is discussed in section 2.3, the truncation parameter χ plays an important role of determine the accuracy of the TEBD method. In Fig. 2.6 and 2.7, we show examples of $\lambda_\alpha^{[l]}$ as a function of l and α for the SF and MI states discussed here. We find that in the SF region, $\lambda_\alpha^{[l]}$ decays to the order of 10^{-4} when α approaches to $\chi = 50$ and in the MI region, $\lambda_\alpha^{[l]}$ decays to the order of 10^{-10} as α approaches $\chi = 50$. The decay becomes faster and faster as U/t increases. In the limit of $U/t \to \infty$, the ground of the model is the Fock state, which is the basis vector state for the TEBD method. Even for the SF region, where the ground state is closer to the many-body state of the lowest single-particle momentum, the value of $\lambda_\alpha^{[l]}$ still decays fast (see Fig. 2.7). Throughout the whole parameter region, we find that reasonable accuracy can be achieved with $\chi \sim M$, where M is the systemsize.

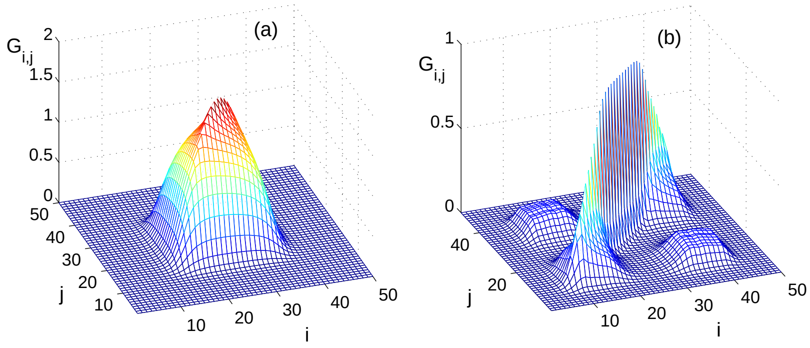

Figure 2.5: One-body density matrix in a trapped system. The parameters in (a) and (b) are the same as in Fig. 2.4. In (a), the system is in the SF state. The density matrix is reduced dramatically to zero near the edge of the cloud. In (b), the off-diagonal decay is exponential in the MI region. The decay changes to algebraic as a result of the SF state at the edge.

The computational cost for one parameter set is around 3 CPU hours for this system-size, which is much more efficient than the direct diagonalization.

In Fig. 2.8, we show the behavior of $\lambda^{[l]}$ in a trapped system. In Fig. 2.8(a), the whole system is in a SF state. The value of $\lambda^{[l]}$ decays faster and the edge of the trap and the slowest at the center of trap. A slight different behavior is found in Fig. 2.8 (b), where $\lambda^{[l]}$ near the center decays much faster than that at the edge. This is the result of a MI state near the center. Overall, we found reasonable accuracy for this calculation as well.

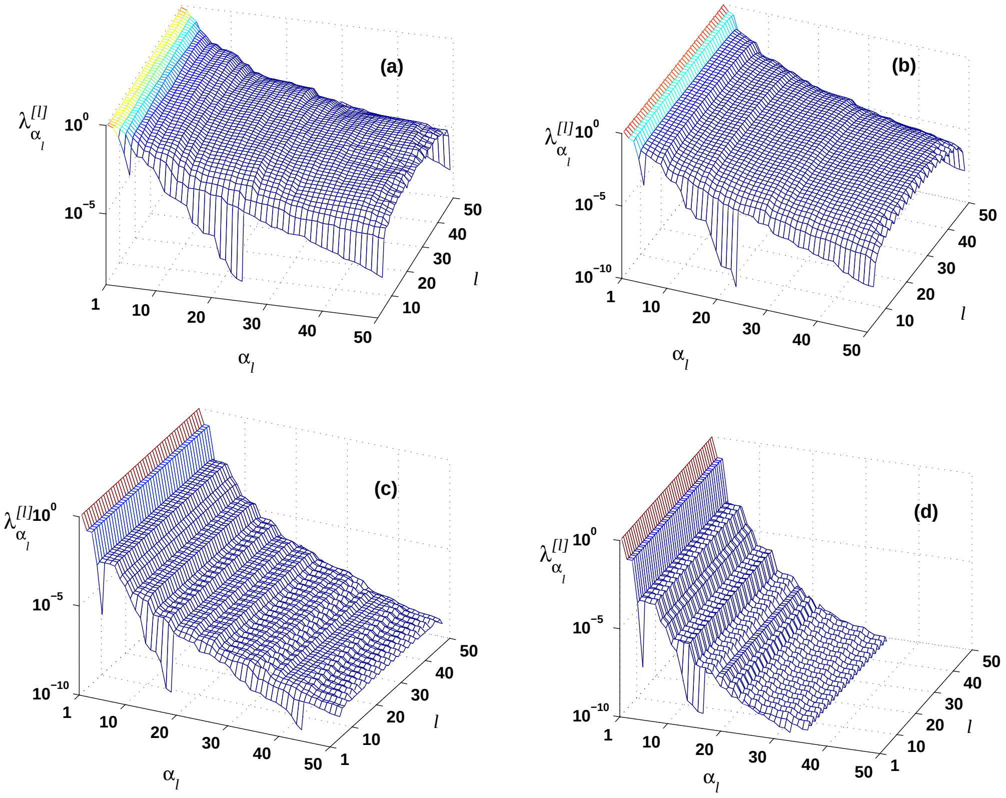

Figure 2.6: Vector $\lambda^{[l]}$ as a function of l and α. The decomposition rank χ is 50 and the size of the system is 50 lattice sites. In (a) and (b), the value of λ decreases to around 10^{-4} for $\alpha = 50$ at the center. In (c) and (d), the value of λdecays rapidly as α increases and is less than 10^{-9} at $\alpha = 50$.

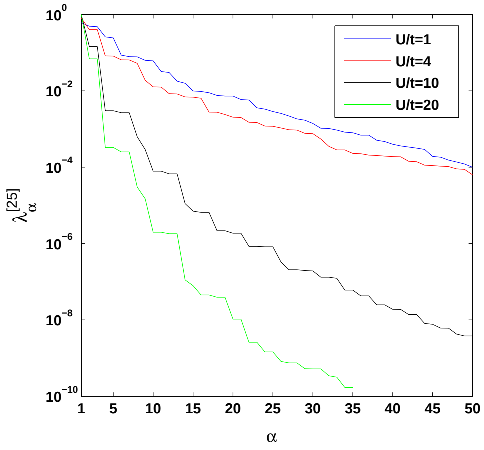

Figure 2.7: Decay of $\lambda^{[25]}$ in SF and MI states. Here, $\lambda^{[25]}$is chosen because it relates with the Schmidt rank at the center of the lattice, which usually has the slowest decay with regard to α. The vector $\lambda^{[25]}$ decays much faster in the MI region than in the SF region.

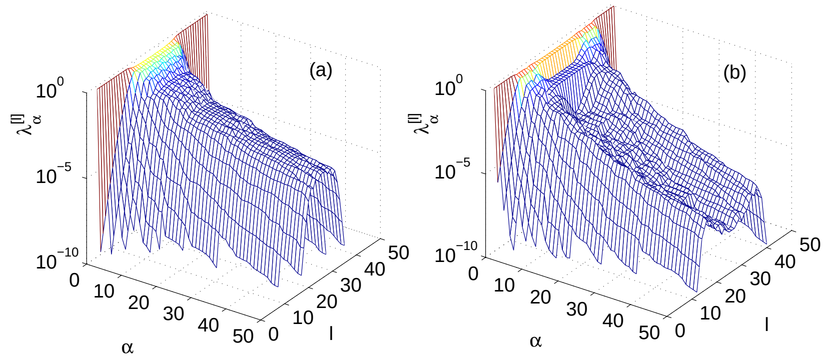

Figure 2.8: Behavior of $\lambda^{[j]}$ for a trapped system. In (a), $\lambda^{[l]}$ corresponds to the SF state of Fig. 2.4 (a) and in (b), $\lambda^{[l]}$ corresponds to the MI-SF mixed state of Fig. 2.4 (b). The behavior of λ reflects the orders that exists in the trap.

Chapter 3

One dimensional binary Bose mixtures in optical lattices (I): paired and counter-flow superfluidity

3.1 Introduction

Bose-Einstein condensation [4] is a fascinating many-body phenomenon, which demonstrates the significance of quantum statistics at low temperature. Identical bosons can occupy the same single particle state and are in fact more likely to do so than classical particles. At a critical temperature, a gas of bosons undergoes a phase transition towards a state in which a macroscopic fraction of the particles occupy the lowest energy state, creating a condensate. Such a state was realized in ultra-cold atom systems in [5], demonstrating that the technology of cooling and manipulating atoms had reached a level of control with which novel states of matter could be generated and studied.

In the case of a Fermi gas, the Pauli exclusion principle prevents such a phenomenon to occur, because no single particle state can be more than singly occupied. However, the phenomenon of condensation can still occur in Fermi systems via a different mechanism: fermions can form pairs to create composite bosons. The bosonic particles then form a condensate of pairs. Conventional superconductors, for example, were understood as a condensate of electron pairs [17]. In ultra-cold atoms, fermionic condensates of this type were created in [55].

Interestingly, this mechanism of condensation of pairs is not limited to fermionic systems but can occur in bosonic systems as well. In fermionic systems, formation of Bosonic pairs necessarily occurs before condensation. In bosonic systems this mechanism can be favored energetically, and will typically be in competition with single particle condensation.

In [56, 57], two types of composite bosons were predicted for a binary Bose mixture in

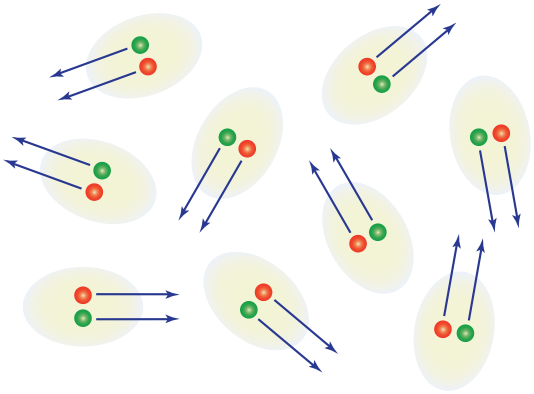

Figure 3.1: Sketch of a condensate of pairs. Atoms of each species (red/green) pair together and form a paired superfluid (PSF) state.

a optical lattice: pairs and anti-pairs. For attractive mutual interactions, a bosonic mixture can form pairs of atoms which then form a paired superfluid (PSF) state, as is visualized in Fig. 3.1. For repulsive interactions, at special fillings, the atoms can form anti-pairs, which can be interpreted as pairs of one atom of one species and one hole of the other species. These anti-pairs can then generate a counterflow superfluid (CFSF) state, visualized in Fig. 3.2. Most of their simulations were performed for two dimensional systems.

In one-dimensional gases quantum phases have quasi-long range order (QLRO), rather than true long range order. QLRO of an operator $O(x)$ is defined as follows: The correlation function $R(x) = \langle O^\dagger(x)O(0)\rangle$ falls off algebraically as $R(x) \sim |x|^{\alpha-2}$ as $|x| \to \infty$ with $\alpha > 0$. Various order parameters $O(x)$ will be defined in the text. In contrast in higher dimensional bosonic systems correlation functions can have true long range order, where correlation functions approach a finite value. Power-law scaling in a 1D optical lattice has been observed in [23]. They observed the Tonks-Girardeau regime of strongly interacting bosons.

In this chapter we consider a two-component Bose mixture held in an optical lattice that only allows atoms to hop in one spatial dimension. We ask the question of how the superfluid as well as other phases or orders can be realized. We assume that the two species of the mixture have the same filling ν, restricted to the range $0 < \nu \leq 1$. The phase diagram of these mixtures is determined using Tomonaga-Luttinger liquid theory [24], which gives the universal phase diagram in terms of a few effective parameters. Based on the universal

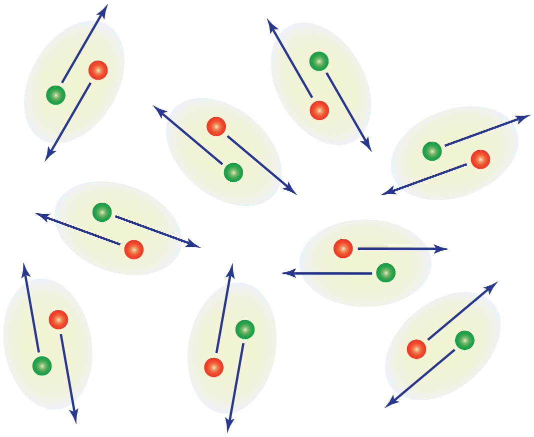

Figure 3.2: Sketch of a condensate of anti-pairs. Here, atoms of one species are strongly anti-correlated with atoms of the other species, creating a counterflow superfluid (CFSF) state. These composite bosons can also be thought of as a pair of one atom of one species and one hole of the other species.

phase diagram, we generate the numerical phase diagram using the time-evolving block decimation (TEBD) method discuss in Chapter 2. With these two approaches we find that CFSF can exist for $\nu = 1/2$ (half-filling) and repulsive interaction, whereas PSF can exist for $\nu < 1$ and attractive interaction (see also [58]).

We also find that charge density wave (CDW) quasi-order can coexist with both PSF and CFSF, as well as single particle superfluidity (SF). The regimes in which CDW and SF quasi-order coexist constitute a quasi-supersolid phase [39, 18]. Similarly, the regimes where CDW and PSF quasi-order coexist is a quasi-supersolid of pairs and in the case of CFSF, a quasi-supersolid of anti-pairs. Previous work has predicted coexistence of CDW and PSF for 1D Bose mixtures [59, 39] and bi-layer 2D lattice bosons with long-range interactions [60], and that of CDW and CFSF for 1D Bose-Fermi mixtures [18, 61].

We then address the question whether PSF and CFSF can be realized and detected in experiment. To simulate the effect of a global trap, we numerically study a mixture confined by a harmonic trap and find that PSF and CFSF can indeed exist in such trapped systems. Their existence can be detected through various measurements. The PSF phase can be detected by using a Feshbach ramp, similar to what has been used in BEC-BCS experiments [55], which generates a quasi-condensate signal in the resulting molecules. The CFSF phase can be detected by applying a $\pi/2$ pulse followed by Bragg spectroscopy.

This generates a quasi-condensate signal in the structure factor. Time-of-flight expansion can also be used to show the absence of single particle superfluidity in PSF and CFSF. Measuring the structure factor via Bragg spectroscopy can be one way of detecting CDW order.

This chapter is organized as follows: in Section 3.2, we introduce the model that is used to describe the system; in Section 3.3, we use Tomonaga-Luttinger liquid theory to derive the phase diagram. The numerical results are discussed in Section 3.4. Specifically, phase diagrams of the homogeneous system are presented in Section 3.4.1, and the realization and detection of PSF and CFSF are discussed in Section 3.4.2. We conclude in Section 3.5.

3.2 Two-component Bose Hubbard model

Ultra-cold bosonic atoms in optical lattices can be well described by Bose Hubbard models [10]. Here, we consider a mixture of two types of atoms confined to a one-dimensional lattice system. The Hamiltonian of such a system is given by

$$\begin{aligned} H &= -t \sum_{a=1,2} \sum_{i=1}^{N-1} (b^{\dagger}_{a,i} b_{a,i+1} + h.c.) + U_{12} \sum_{i=1}^{N} n_{1,i} n_{2,i} \\ &\quad + \frac{U}{2} \sum_{a=1,2} \sum_{i=1}^{N} n_{a,i}(n_{a,i} - 1). \end{aligned} \tag{3.1}$$

We denote the different types of atoms with index $a = 1, 2$, and the lattice site with index i. We assume that the two species have equal particle density $\nu \leq 1$, the same intra-species interaction $U > 0$ and hopping parameter $t > 0$. The inter-species interaction is given by U_{12}. The operators $b^{\dagger}_{a,i}$ and $b_{a,i}$ are the creation and annihilation operators for atoms of type a and site i and $n_{a,i} = b^{\dagger}_{a,i} b_{a,i}$ are the number operators.

3.3 Luttinger liquid approach

The universal behavior of this system can be found within a Tomonaga-Luttinger liquid description [24]. First, we switch to a continuum description, $b_{a,i} \to b_a(x)$, and express the operators $b_a(x)$ through a bosonization identity, according to Haldane [25, 62]:

$$b_a(x) = [n + \Pi_a(x)]^{1/2} \sum_m e^{2mi\Theta_a(x)} e^{i\phi_a(x)}, \tag{3.2}$$

where the real-space density of each species is $n = \nu/a_L$ and a_L is the lattice constant. The lattice sites are at positions $x = ia_L$. This expression is a phase-density representation of the Bose operators, in which the square root of the density operator has been written in an intricate way. The fields $\Pi_{1,2}(x)$ describe the small amplitude and the long wave length density fluctuations. The fields $\Theta_{1,2}(x)$ are given by $\Theta_{1,2}(x) = \pi n x + \theta_{1,2}(x)$, where $\theta_{1,2}(x) = \pi \int^x dy \Pi_{1,2}(y)$. The fields $\phi_{1,2}(x)$ describe the phase, and are conjugate to the density fluctuations $\Pi_{1,2}(x)$.

The contact interactions between the densities in 3.1 written in Haldane's representation generate an infinite series of terms that contain $\exp(2m_1 i(\pi n x + \theta_1) + 2m_2 i(\pi n x + \theta_2))$, where m_1 and m_2 are some integers. A term of this form can only drive a phase transition, if the oscillatory part $2\pi m_1 n x + 2\pi m_2 n x$ vanishes for all lattice sites. This leads to the requirement $m_1\nu + m_2\nu = m_3$, with m_3 another integer [59]. As a further requirement, small integers m_1 and m_2 are necessary, because the scaling dimension of the term scales quadratically in m_1 and m_2.

For the range $0 < \nu \leq 1$, we find that there are three different cases: unit-filling ($\nu = 1$), half-filling ($\nu = 1/2$), and non-commensurate filling ($\nu \neq 1$ and $\nu \neq 1/2$). It can be checked, using renormalization group arguments as below, that higher forms of commensurability do not generate new phases, but that either phase separation or collapse is reached first. Our numerical findings are consistent with this.

Non-commensurate filling. The action of the system, assuming a short-range spatial cutoff r_0, at non-commensurate filling is given by [24, 62, 39]:

$$\begin{aligned} S &= \int d^2r [\sum_{j=1,2} \frac{1}{2\pi K} \left((\partial_{v\tau}\theta_j)^2 + (\partial_x \theta_j)^2 \right) \\ &\quad + \frac{U_{12} a_L}{\pi^2 v \hbar} \partial_x \theta_1 \partial_x \theta_2 + \frac{2 g_\sigma}{(2\pi r_0)^2} \cos(2\theta_1 - 2\theta_2)] \end{aligned} \tag{3.3}$$

The first line of the action is characterized by a Luttinger parameter K and a velocity v, contained in $\mathbf{r} = (v\tau, x)$. This part of the action, without the coupling between the two fields $\theta_a(x)$, generates a linear dispersion $\omega = v|k|$, where . v should therefore be interpreted as the phonon velocity. The Luttinger parameter K is a measure of the intra-species interaction U. We will be interested in the regime $U \gtrsim t$, in which we have approximately [63]

$$K \quad \approx \quad 1 + \frac{8t}{U}\frac{\sin \pi\nu}{\pi}. \tag{3.4}$$

The velocity v can also be related to the parameters of the underlying Hubbard model by

$$v \approx v_F(1 - 8t\nu \cos \pi\nu / U) \tag{3.5}$$

where v_F is the 'Fermi velocity' of an identical system of fermions, $v_F = 2(a_L t/\hbar)\sin \pi\nu$, and k_F is the 'Fermi wave vector', $k_F = \pi n$. Here, $\hbar$ is the Planck constant.

The two fields $\theta_a(x)$ are coupled by the inter-species interaction. The interaction term $U_{12}n_1n_2$ in the underlying Hubbard model generates both the term containing $\partial_x\theta_1\partial_x\theta_2$, as well as the backscattering term [24, 59] containing $\cos(2\theta_1 - 2\theta_2)$. The action S is only well-defined with a short-range cut-off r_0. It is proportional to $1/n$. At this scale, g_σ is approximately given by

$$g_\sigma \quad = \quad U_{12}a_L/(v\hbar). \tag{3.6}$$

We diagonalize the quadratic part of the action by switching to the symmetric and antisymmetric combinations $\theta_{S/A} = \frac{1}{\sqrt{2}}(\theta_1 \pm \theta_2)$. For the two sectors we find

$$K_{S/A} \quad = \quad (1/K^2 \pm U_{12}a_L/(v\hbar\pi K))^{-1/2} \tag{3.7}$$

as effective Luttinger parameters. To lowest order in U_{12} this gives $K_{S/A} \approx K \mp U_{12}a_LK^2/(2\pi v\hbar)$. The effective velocities are $v_{S/A} = v\sqrt{1 \pm U_{12}a_LK/(\pi v\hbar)}$. Collapse (phase separation) of the superfluid phase is when $v_{S/A}$ is imaginary. We note that K_S diverges when collapse (CL) is approached, and that K_A diverges as the system approaches phase separation (PS).

The anti-symmetric sector contains the nonlinear backscattering term $\cos(2\sqrt{2}\theta_A)$. To study its effect, we use an RG approach. We renormalize the short-range cut-off r_0 to a slightly larger value, and correct for it at one-loop order. The resulting flow equations are given by [24]:

$$\begin{aligned} \frac{dg_\sigma}{dl} &= (2 - 2K_A)g_\sigma && (3.8) \\ \frac{dK_A}{dl} &= -\frac{g_\sigma^2}{2\pi^2}K_A^3 && (3.9) \end{aligned}$$

The flow parameter l is given by

$$l = \log_e\left(\frac{r_0'}{r_0}\right), \qquad (3.10)$$

where r_0' is the new cut-off that has been created in the RG process.

The flow equations 3.8 and 3.9 have two qualitatively different fixed points: Either g_σ diverges, which in turn renormalizes K_A to zero, or g_σ is renormalized to zero for finite $K_A = K_A^*$. In the latter case, the action S is quadratic in θ_S and θ_A. For the parameter K_S, we use the bare value given in Eq. 3.7.

As mentioned in the introduction, we can determine the phase diagram by studying the long-range scaling behavior of correlation functions, $\langle O^\dagger(x)O(y)\rangle$, of various order parameters $O(x)$. In particular, the single-particle superfluid order parameter is $O_{SF} = b_a(x)$ with $a = 1, 2$. The CDW order is related to the $2k_F$ wavevector component of the density operator, $O_{CDW} = n_a$. PSF is described by $O_{PSF} = b_1(x)b_2(x)$, and CFSF by $O_{CFSF} = b_1^\dagger(x)b_2(x)$. In the homogeneous system, it suffices to study

$$\begin{aligned} G(x) &= \langle b_a^\dagger(x)b_a(0)\rangle, a = 1, 2 && (3.11) \\ R_{n,a}(x) &= \langle n_a(x)n_a(0)\rangle, a = 1, 2 && (3.12) \\ R_S(x) &= \langle b_1^\dagger(x)b_2^\dagger(x)b_1(0)b_2(0)\rangle && (3.13) \end{aligned}$$

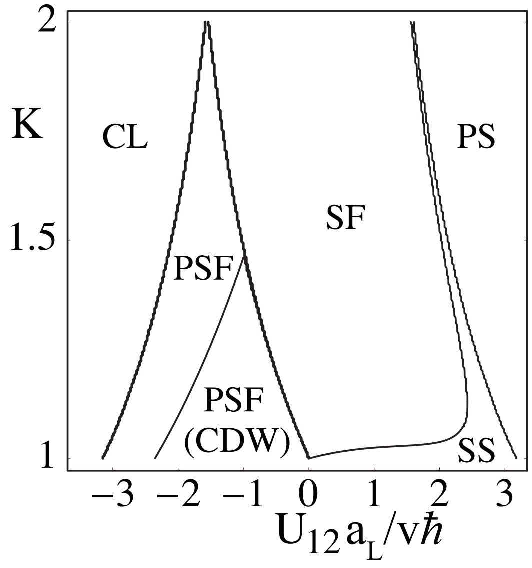

Figure 3.3: Phase diagram of a bosonic mixture at non-unit and non-half-filling. For attractive interactions U_{12} and $K < 2$ the system can form a paired superfluid state, in the regime labeled PSF and PSF(CDW). This phase can coexist with CDW order for weaker interactions. For large repulsive (attractive) interactions U_{12} the system phase separates (PS) (collapses (CL)). For the remaining regime the system shows single particle superfluidity (SF). This can coexist with CDW order, resulting in a quasi-supersolid (SS) regime.

$$R_A(x) \quad = \quad \langle b_1^\dagger(x) b_2(x) b_1(0) b_2^\dagger(0)\rangle. \tag{3.14}$$

We find that away from collapse (CL) and phase separation (PS), the correlation functions scale either algebraically or exponentially. For algebraic scaling, we have

$$\begin{aligned}
G(x) &\sim |x|^{\alpha_{SF}-2}, \\
&\quad \alpha_{SF} = 2 - 1/(4K_S) - 1/(4K_A) && (3.15)\\
R_{n,a}(x) &\sim \cos(2k_F x)|x|^{\alpha_{CDW}-2}, \\
&\quad \alpha_{CDW} = 2 - K_S - K_A && (3.16)\\
R_S(x) &\sim |x|^{\alpha_{PSF}-2}, \alpha_{PSF} = 2 - 1/K_S && (3.17)\\
R_A(x) &\sim |x|^{\alpha_{CFSF}-2}, \alpha_{CFSF} = 2 - 1/K_A. && (3.18)
\end{aligned}$$

where the scaling exponents α_O are determined by K_S and K_A after the RG flow. For the case that g_σ diverges in Eqs. 3.8 and 3.9 and K_A is undefined, these expressions can still be used. We set K_A to zero, and find that α_{CDW} and α_{PSF} are well defined. Hence $R_{n,a}$ and R_S still show algebraic scaling. On the other hand, α_{CFSF} and α_{SF} become $-\infty$ and G and R_A scale exponentially.

We can identify regimes where different scaling exponents are positive based on the relationship between the scaling exponents and $K_{S/A}$ after the flow. This determines the different quasi-long range orders that are present. The resulting phase diagram is shown in Fig. 3.3, as a function K and $U_{12}a_L/(v\hbar)$, as appearing in the action in Eq. 3.3. These two parameters determine the initial values of the flow equations through equations 3.7 and 3.6.

We can estimate the phase boundary between PSF and SF. For small $U_{12}a_L/(v\hbar)$ this boundary is near the point $K_A = 1$ and $g_\sigma = 0$. For that limit, Eq. (3.9) can be linearized to

$$\frac{dK_A}{dl} = -\frac{g_\sigma^2}{2\pi^2} \tag{3.19}$$

and the expression $A = \pi^2(1 - K_A)^2 - g_\sigma^2/4$ becomes an invariant of the flow. From the properties of the RG flow of a Berezinskii-Kosterlitz-Thouless transition (see e.g. [24, 27]), the phase boundary is given by $A = 0$ and $g_\sigma < 0$. Using the expressions of K_A and v in terms of the Hubbard parameters, we estimate the critical interaction U_{12} for PSF to occur at

$$\left.\frac{U_{12}}{U}\right|_c = -32\frac{t^2}{U^2}\sin^2(\pi\nu). \tag{3.20}$$

The phase boundary between supersolid (SS) and SF has been derived in Ref. [39].

Half-filling. In the case of half-filling, another non-linear term has to be introduced in the action

$$S_{uk} = \frac{2g_{uk}}{(2\pi r_0)^2}\int d^2r\cos(2\theta_1 + 2\theta_2). \tag{3.21}$$

This term describes Umklapp scattering. At the initial cut-off $r_0 \sim 1/n$, g_{uk} is approximately given by $U_{12}a_L/v$. In addition to the RG flow in the antisymmetric sector we now

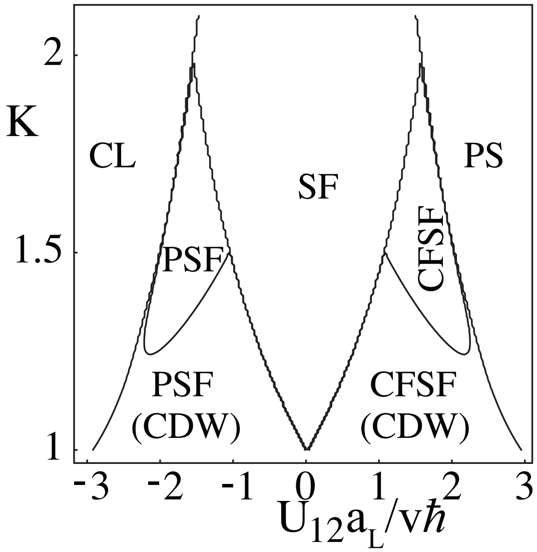

Figure 3.4: Phase diagram of a bosonic mixture at half-filling. In addition to the phases that appear in Fig. 3.3, the system now develops a counterflow superfluid (CFSF) phase, which can coexist with CDW order.

also have

$$\frac{dg_{uk}}{dl} = (2 - 2K_S)g_{uk} \tag{3.22}$$

$$\frac{dK_S}{dl} = -\frac{g_{uk}^2}{2\pi^2}K_S^3 \tag{3.23}$$

in the symmetric sector. Proceeding along the same lines as for the non-commensurate case, we find the phase diagram shown in Fig. 3.4.

We estimate the SF-CFSF phase boundary in the same way as the PSF-SF boundary. We find

$$\left.\frac{U_{12}}{U}\right|_c = 32\frac{t^2}{U^2}\sin^2(\pi\nu). \tag{3.24}$$

Unit-filling. At unit-filling we have to introduce a term of the form

$$S_1 = \frac{2g_1}{(2\pi r_0)^2}\int d^2r\,(\cos(2\theta_1) + \cos(2\theta_2))\,. \tag{3.25}$$

The resulting RG flow for this system is given by

$$\begin{aligned}
\frac{dg_{uk}}{dl} &= (2-2K_S)g_{uk} + \alpha_3 \frac{g_1^2(K_A-K_S)}{2\pi} && (3.26)\\
\frac{dg_{\sigma}}{dl} &= (2-2K_A)g_{\sigma} + \alpha_3 \frac{g_1^2(K_S-K_A)}{2\pi} && (3.27)\\
\frac{dg_1}{dl} &= (2-\frac{K_S+K_A}{2} + \alpha_3 \frac{g_{uk}K_S + g_{\sigma}K_A}{\pi})g_1 && (3.28)\\
\frac{dK_A}{dl} &= -\frac{g_{\sigma}^2}{2\pi^2}K_A^3 - \frac{g_1^2}{16\pi^2}(K_S+K_A)K_A^2 && (3.29)\\
\frac{dK_S}{dl} &= -\frac{g_{uk}^2}{2\pi^2}K_S^3 - \frac{g_1^2}{16\pi^2}(K_S+K_A)K_S^2 && (3.30)
\end{aligned}$$

where α_3 is some non-universal parameter [64]. The behavior of this set of equations depends strongly on the initial value of g_1. For small values of g_1, four phases can be stable: Single-particle superfluidity, CFSF, PSF and a Mott phase. For large values only single-particle SF and MI are stable. We determine with our numerical approach, that the Hubbard model falls into the second category, i.e. there is only a single-particle SF and a Mott state at unit-filling.

Having established the universal behavior of the system from Tomonaga-Luttinger liquid theory, we now want to connect the phase diagram with the parameters in the Hubbard model. The expressions 3.4 and 3.5, which relate the Luttinger parameter K and the velocity v to microscopic parameters of the Hubbard model, are only approximate, no full analytic expression is known. In addition, only some phase boundaries are predicted reliably, because we use perturbative RG in the g_{σ}. We expect that the analytic calculation only predicts the general structure of the phase diagram, as well as the decay behavior of the correlation functions. To obtain the phase diagram in terms of the parameters in the Hubbard model, we need to use numerical methods. The next section describes the numerical determination of the phase diagram.

3.4 Numerical approach

We use the time-evolving-block-decimation (TEBD) method to obtain an approximate ground state solution. We consider N lattice sites with hard-wall boundary conditions and express

	$R_S(x)$	$R_A(x)$	$G(x)$	$R_{n,a}(x)$
MI	E	E	E	A
SF	A	A	A	A
CFSF	E	A	E	A
PSF	A	E	E	A
CDW	A or E	A or E	A or E	A ($\alpha < 2$)

Table 3.1: Definitions of MI, SF, CFSF and PSF orders in terms of the large x behavior of the correlation functions $R_S(x)$, $R_A(x)$, and $G(x)$, $R_{n,a}(x)$. A: algebraic decay of the form $x^{-\alpha}$; E: exponential decay of the form $e^{-\beta x}$. A correlation function is said to exhibit quasi-order when it is subject to algebraic decay with $\alpha < 2$. In this system, the algebraic decay for R_S, R_A and G always has $\alpha < 2$, while $R_{n,a}$ can have $\alpha \geq 2$. CDW quasi-order exists only when $R_{n,a}$ is described by $\alpha < 2$.

the Hubbard parameters in units of the intra-species interaction U. The number of sites N is equal to 80, unless otherwise noted. In our numerical analysis, we limit the particle number on each site and each species to two for filling $\nu \leqslant 0.8$ and four otherwise. Once we obtain the ground state, we calculate the energy, density distributions, correlation functions, and the structure factor to identify the quasi-long range order and other properties of the ground state.

For example, to determine whether a SF, PSF, or CFSF is present, we study the decay behavior of the correlation functions, $G(x)$, $R_A(x)$, and $R_S(x)$, defined in Eqs. 3.11, 3.14, and 3.13, respectively. If both R_A and R_S decay algebraically, the system is in a single-particle superfluid (SF) state. If both are exponential, the system is in a Mott insulator(MI) state. If R_S or R_A decays algebraically, the system is in the PSF or CFSF state, respectively. These relationships are summarized in Table 3.1.

In Fig. 3.5(a) and (b), we show the decay behavior of the correlation functions in the PSF and CFSF phase, respectively. As the Hamiltonian is discrete, the correlation functions are calculated as discrete functions: $G(i,j) = \langle b^\dagger_{a,i} b_{a,j} \rangle$, $R_S(i,j) = \langle b^\dagger_{1,i} b^\dagger_{2,i} b_{1,j} b_{2,j} \rangle$, and $R_A(i,j) = \langle b^\dagger_{1,i} b_{2,i} b_{1,j} b^\dagger_{2,j} \rangle$. For the PSF phase, $R_A(i,j)$ decays exponentially, while R_S decays algebraically. It is also worthwhile to notice that the single-particle Green's function decays *exponentially*, implying the absence of single-particle superfluidity. For the CFSF phase, R_A decays algebraically while R_S decays exponentially. Single-particle superfluidity is again absent.

Behavior of K_S and K_A: We study the decay behavior of R_S and R_A in more detail. Using

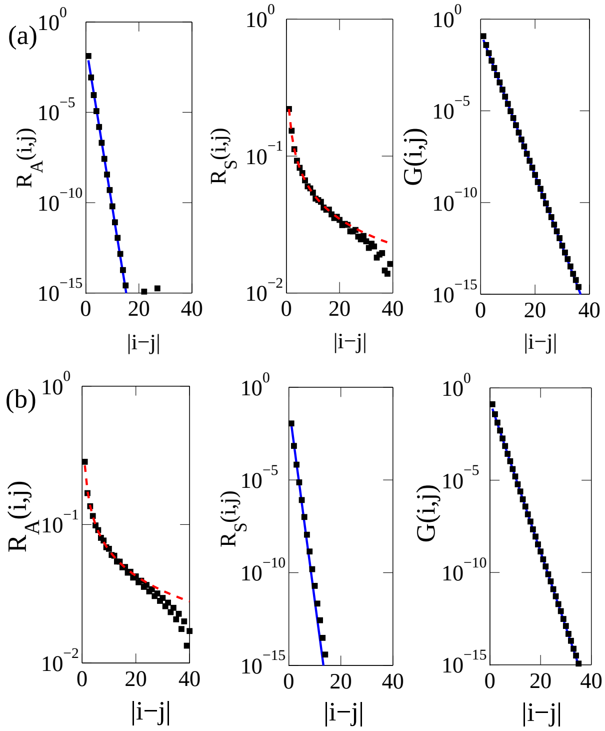

Figure 3.5: Correlation functions R_A, R_S, and G on a logarithmic scale as a function of distance $|i-j|$. The index i is 40, the center of the 80 lattice sites. The squares are the numerical data. The blue lines are exponential fits to the data and red dotted lines are algebraic fits. Note that the scale of the vertical axis of the graphs differs by orders of magnitude. In (a), we show an example for the paired superfluid phase at ν=0.3, $t = 0.02U$, and $U_{12} = -0.16U$. R_A decays exponentially and R_S decays algebraically. The single-particle correlation function decays exponentially, implying the absence of single-particle superfluidity. In (b), we show an example for the counterflow superfluid phase at $\nu = 0.5$, $t = 0.02U$, and $U_{12} = 0.2U$. The anti-pair correlation function R_A decays algebraically, while the pair correlation function decays exponentially. Single-particle superfluidity is again absent. The algebraic fits deviate from the data around $|i-j| \approx 40$, due to the boundary conditions of our numerical calculations.

the fit function, $c \cdot |i-j|^{\alpha-2}$, where c and α are the fitting parameters, we obtain the power-law exponent α and, hence, the Luttinger parameters K_S and K_A based on Eqs. 3.17 and 3.18. In Fig. 3.6(a), we show these K_S and K_A as a function of U_{12}, for non-commensurate filling. A Luttinger parameter is formally set to zero when its correlation function decays exponentially.

For $U_{12} < -0.06U$, R_A decays exponentially, while for $U_{12} > -0.06U$, R_A decays algebraically, and K_A. increases as U_{12} increases. The system undergoes a PSF to SF transition at $U_{12} = -0.06U$. On the other hand, K_S decreases monotonically for $U_{12} > -0.6U$. For $U_{12} < -0.6U$ the numerics failed to converge to a homogeneous state. This indicates that the system collapses, and we therefore cannot extract a Luttinger liquid parameter. We can observe charge density wave (CDW) order for a range of U_{12}/U in Fig. 3.6. According to Eq. 3.16, this order exists when $K_S + K_A < 2$. In fact, it co-exists with the SF, PSF or CFSF order. At half-filling, K_S will go to zero at a critical, positive value of U_{12}. This indicates the transition from the SF to CFSF phase.

Finite-size effect: The behavior of $K_{A/S}$ stated above is affected by the size of the system. Finite size effects can 'smooth out' a sudden change in $K_{A/S}$ at the phase transition. This effect can be estimated from the RG flow calculation by integrating Eqs. 3.8 and 3.9 out to a finite value l rather than to infinity. In Fig. 3.6(b), we show an example of a finite-l RG calculation in the vicinity of the PSF-to-SF transition. We see that as l increases, K_A dramatically changes for the attractive U_{12}. In the limit of $l \to \infty$, K_A becomes discontinuous and 'jumps' from 0 to 1 at $U_{12} \approx -0.01U$. This is where the PSF-to-SF transition occurs. This transition is a Berezinskii-Kosterlitz-Thouless transition [27, 24]. In order to compare the RG result with our TEBD result, we associate the system size N with the flow parameter l, based on the relation in Eq. 3.10. The cut-off r_0 is the lattice constant a_L and $r_0' = Na_L$. For $N = 80$ we have $l = 4.4$ and we find that the RG and TEBD are in good agreement. The regime between $U_{12}/U \approx -0.06$ and -0.01 is a cross-over regime due to the finite size of the system.

Collapse and phase separation: For large $|U_{12}|$, the system approaches collapse or phase separation. According to Tomonaga-Luttinger liquid theory, $K_S \to \infty$ as the system approaches collapse and $K_A \to \infty$ as the system approaches phase separation. As seen in

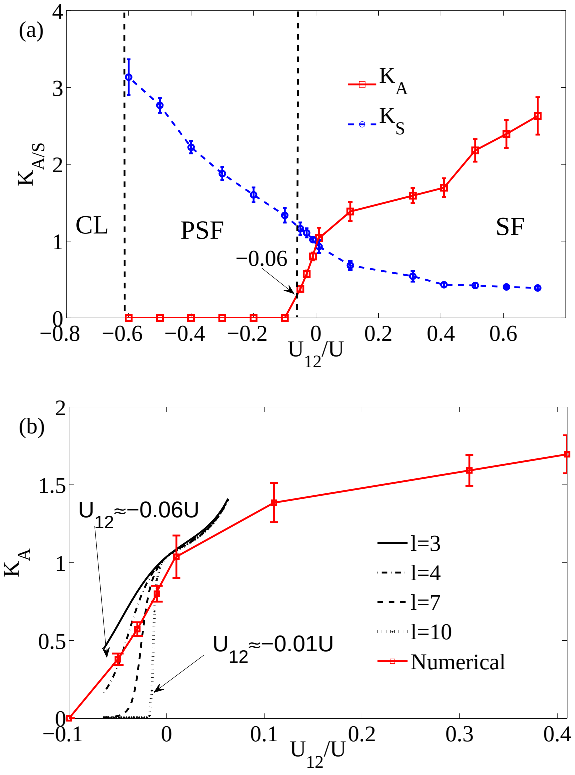

Figure 3.6: (a) K_S and K_A as a function of U_{12} as extracted from the fit of the correlation functions, R_S and R_A. The filling ν is 0.7 and t/U is 0.02. Around $U_{12}/U \approx -0.06$, the anti-pair correlation function changes from algebraic to exponential decay. This corresponds to the transition from the PSF to SF phase. When R_A decays exponentially, K_A is formally set to zero. For $K_a + K_s \lesssim 2$, the system has CDW order. Error bars are one standard deviation uncertainties obtained from the power-law fit to the numerical data. (b) Comparison of K_A obtained from our RG and TEBD calculations. The red square connected by lines are the TEBD results while all other lines are determined from the RG flow with flow parameter $l = 3, 4, 7$, and 10, where l is defined in Eq. 3.10. The error bars are as in panel (a). The PSF-to-SF transition obtained from TEBD is around $U_{12}/U \approx -0.06$, while the RG calculation shows that for $l = 10$, the transition occurs near $U_{12}/U \approx -0.01$. We interpret the regime between $U_{12}/U \approx -0.06$ and -0.01 the cross-over region.

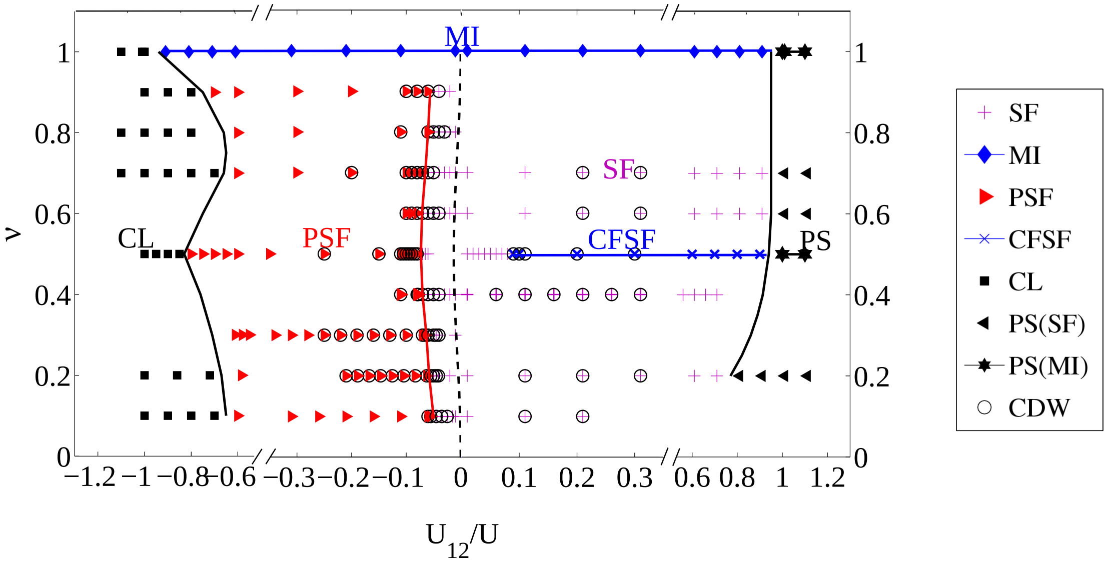

Figure 3.7: Phase diagram for a homogeneous system with 80 sites and the hopping parameter $t = 0.02$U as a function of filling ν and inter-species interaction U_{12}/U. The horizontal axis shows three disconnected regions in U_{12}/U. The solid lines are the estimated phase boundaries based on the TEBD results and the dotted line is the PSF-to-SF phase boundary predicted by our RG calculation (see Eq. 3.20). For attractive interaction $U_{12} \lesssim -0.06U$, the system forms a paired-superfluid (PSF). The state collapses(CL) for $U_{12} \lesssim -0.7U$. For $U_{12} \gtrsim -0.06$ and $U_{12} \lesssim U$ the system shows single-particle superfluidity (SF). The system phase-separates (PS) for $U_{12} \gtrsim 1$ and forms two single-particle superfluids (SF). Open circles are the points where $K_S + K_A < 2$ and charge density wave (CDW) order coexists with a superfluid phase (SF,PSF, or CFSF). At half and unit filling there exist special phases. For repulsive interaction $U_{12} \gtrsim 0.08U$ and half-filling, the system forms a counterflow superfluid (CFSF). For unit filling, we find a Mott-Insulator (MI) phase for interactions $|U_{12}| \lesssim U$. Finally, in the PS region at half- and unit-filling, the system forms two individual MI states.

Fig. 3.6, we indeed find such a tendency in our TEBD calculations. For $U_{12} > 0.8U$ (not shown), K_A increases rapidly to values around 10, indicating a possible phase separation. For $U_{12} < -0.6U$, due to the slow decay of the correlation function R_S and the finite-size of our system, we are unable to extract an accurate K_S from the numerical result. On the other hand, we observe a peaked density distribution for $U_{12} < -0.6U$, indicating a collapse. In the phase separation regime, $G(x)$ has algebraic decay except for $\nu = 0.5$ or 1, where it has exponential decay. An algebraic decay implies two spatially-separated single-species superfluids while the exponential decay implies two spatially-separated Mott insulators.[65].

3.4.1 Phase diagram

We study the phase diagram as a function of filling ν and parameters of the Hubbard Hamiltonian. Assuming a positive U, the system can be fully characterized in terms of ν, t/U, and U_{12}/U. Our results are shown in Fig. 3.7 for a fixed hopping parameter and in Fig. 3.8 for half filling.

3.4.1.1 Phase diagram at a fixed hopping parameter

In Fig. 3.7 we show the phase diagram for filling fractions between 0 and 1 and the interaction U_{12}/U between -1.1 and 1.1. The symbols correspond to numerical data points at which the phases have been characterized. Different markers represent the different orders. The orders are determined from the decay behavior of the three correlation functions R_A, R_S, and G.

For weak attractive inter-species interaction, $-0.06 < U_{12}/U < 0$, the system is in a SF state. As U_{12} grows more attractive, paired superfluidity (PSF) occurs. The critical U_{12} is largest, $\sim -0.08U$, at half-filling and gradually decreases away from half-filling. This phase boundary differs from that predicted by our RG calculation (Eq. 3.20), plotted as the dotted line in Fig. 3.7. This discrepancy is the result of the finite-size effect discussed in Fig. 3.6(b). In the SF to PSF cross-over regime, charge density wave (CDW) order can coexist. According to the phase diagram Fig. 3.3, for attractive interaction, CDW order can co-exist only with PSF order. In our numerical work, we observed the CDW order slightly outside the numerical phase boundary of PSF but within the RG phase boundary of PSF. The sub-regime where CDW and PSF coexist ends when $U_{12}/U \lesssim -0.4$. When the inter-species attraction is comparable to the intra-species repulsion, $U_{12} \lesssim -U$, the system collapses (CL) and no long-range order is present.

For repulsive inter-species interaction and $U_{12} < U$, the system is in a SF state for all non-commensurate fillings. Within the SF regime, there is a smaller parameter region where CDW order coexist with the SF order. This subregime is a quasi-supersolid regime. The boundary between a normal superfluid and a quasi-supersolid is estimated by RG calculation in Ref. [39]. At half-filling, counterflow superfluidity (CFSF) occurs when $0.08 \lesssim U_{12}/U \lesssim 1$. Within the CFSF regime, the CDW order can coexist, forming a quasi-supersolid of anti-pairs. It also worthwhile to point out that at half-filling, CDW order only exists within the PSF and CFSF regimes.

At unit filling, our numerical results do not show evidence of PSF or CFSF for any U_{12}. We find a Mott insulator (MI) state for $|U_{12}| < U$.

3.4.1.2 Phase diagram at half-filling

In Fig. 3.8, we show the phase diagram at half filling as a function of U_{12}/U and t/U. From this diagram, we find that the border between PSF and SF and the border between PSF and CL approach each other as t increases. Similarly, the border between the CFSF and SF and the border between CFSF and PS approach each other. In fact, the PSF and CFSF phases end around $t \sim 0.16U$. Within the PSF and CFSF regimes, CDW order can co-exist. In the phase separated regime, the separated single-species ensembles form two individual Mott insulating states for $t \lesssim 0.14U$ and two individual SF states for $t > 0.14U$.

We can compare this phase diagram with the half-filling phase diagram in Fig. 3.4 obtained from Tomonaga-Luttinger liquid theory. Especially, we can compare the location of the phase boundary between SF and PSF(CFSF). To do so, we plot the RG phase boundaries, described by Eqs. 3.20 and 3.24, onto our phase diagram. The area near the two boundaries is interpreted as the cross-over regime where finite-size effects modify the phase boundary.

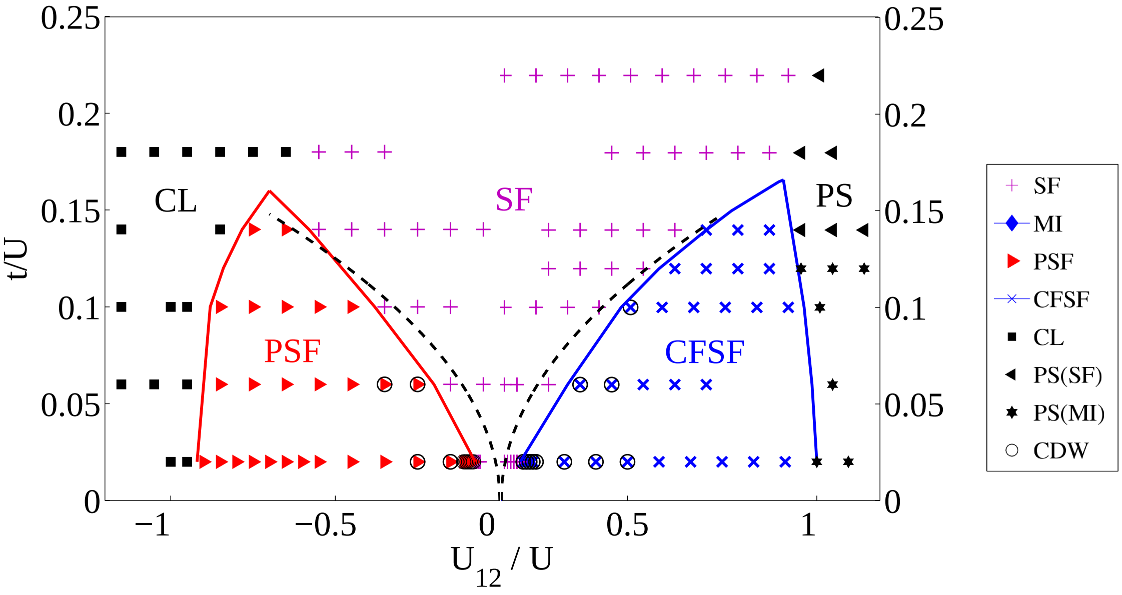

Figure 3.8: Phase diagram at half-filling as a function of U_{12}/U and t/U. The solid lines are estimated phase boundaries from the TEBD calculation and the dotted lines are the phase boundaries predicted by the RG calculation (see Eqs. 3.20 and 3.24). For large repulsive interaction, the system phase separates (PS) and for large attractive interaction, the system collapses (CL). For moderate interactions and for $t/U \lesssim 0.2$, the system shows paired superfluidity (PSF) on the attractive side and counterflow superfluidity on the repulsive side. Both PSF and CFSF can coexist with charge density wave (CDW) order when $t \lesssim 0.1U$.

3.4.2 Realization and detection

Having established the phase diagram for the homogeneous system, we now discuss how to realize and detect the PSF and CFSF phases. First, we need to modify the Hubbard Hamiltonian in Eq. 3.1 because in any ultra-cold atom experiment an additional trapping potential is present. We add a harmonic potential, $\Omega(j - j_c)^2(n_{1,j} + n_{2,j})$, where j is the site index and j_c is the index at the center of the system. The TEBD method is used to find the ground state. We consider a system of 80 lattice sites and adjust the total number of particles and the trap frequency so that the number of particles is negligible at the edge of the lattice.

We again determine the orders of the system by studying the correlation functions in Table 3.1. We find that, in spite of the presence of the trap, the correlation functions still show exponential or algebraic scaling away from the edge of the lattice. In fact, a correlation function can have different decay behavior in different parts of the trap. We also find that SF, PSF, and CFSF still exist. The remainder of this article focuses on experimental signatures that distinguish between these orders by calculating the density distribution, the time-of-flight image after an expansion, or the structure factor for Bragg spectroscopy.

Density distribution: We find that in a trapped system PSF and CFSF can only exist when the density distribution satisfies certain conditions. For PSF, the density of each species at the center of the trap, n_{center}, must be less than one atom per site or equivalently per lattice constant a_L. (The density is largest at the center.) For CFSF, n_{center} must satisfy $n_{\mathrm{center}} a_L = 1/2$. Once such conditions are satisfied, the critical value of U_{12} for PSF and CFSF is close to the one for a homogeneous system (See Figs. 3.7 and 3.8).

In Fig. 3.9(a) we show density distributions for three attractive interactions U_{12} and a hopping parameter equal to the one used for Fig. 3.7. For all attractive interactions, the density distributions of each species are the same. For more attractive inter-species interaction, the density distribution concentrates near the center of the trap. There is no discontinuous change in the density distribution when the system goes from SF to PSF.

In Fig. 3.9(b) we show the density distribution for $U_{12} = 0.2U$. In this case in the center of the trap, where the density distribution is constant or has a "plateau", the system is in a

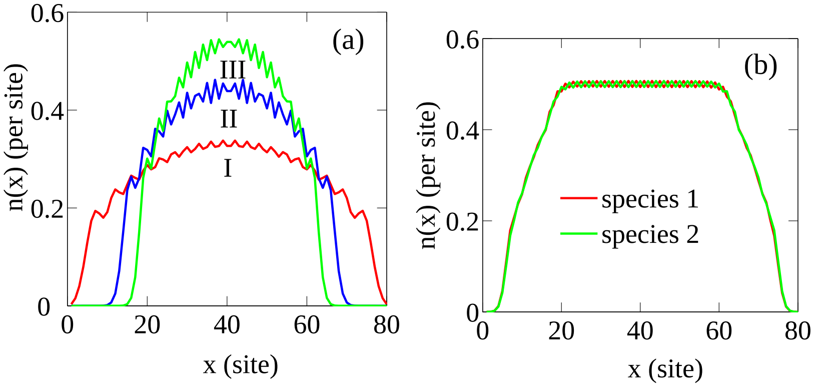

Figure 3.9: Density distribution of a trapped system for $t = 0.02U$. (a) Attractive interaction U_{12}. The trap frequency is $\Omega = 1 \times 10^{-5}U$ and the number of atoms is 20 for each species. For attractive interactions, the density distributions of the two species are identical. For $U_{12} = -0.01U$ (curve I) the system is superfluid. For $U_{12} = -0.11U$ (curve II) and $U_{12} = -0.21$U (curve III), the system is in the paired superfluid (PSF) state. As U_{12} becomes more negative the distribution gradually shrinks in size. (b) Repulsive interaction $U_{12} = 0.2U$ with $\Omega = 8 \times 10^{-5}U$ and 30 atoms of each species. The red and green curves correspond to the species, respectively. The density distribution has a 'plateau' with half-filling in the center of the trap. The system is in a counter-flow superfluid (CFSF) state. The two species have weak interlocked density modulations around half filling.

CFSF state. The “plateau” is at half-filling consistent with predictions from a local density approximation and noting that in Fig. 3.7 CFSF only occurs at $\nu = 1/2$. Towards the edge, where the density is decreasing sharply, it is in a SF state. The plateau implies that the system is incompressible in the center.

Time of flight measurement: A widely used measurement technique in the field of ultracold atoms is measuring the density of atoms after a time-of-flight (TOF) expansion. The 1D optical lattice potential and the harmonic trap are abruptly turned off at time $T = 0$ and the atoms expand freely afterwards. We calculate the density at time T, according to

$$n_a(x,T) = \langle c_a^\dagger(x,T) c_a(x,T)\rangle \tag{3.31}$$

with $a = 1, 2$. The operators $c_a(x,T)$ are related to the lattice operator $b_{a,j}$ according to

$$b_a(x,T) = \sum_{j=1}^{N} w(x - r_j, T) b_{a,j}, \tag{3.32}$$

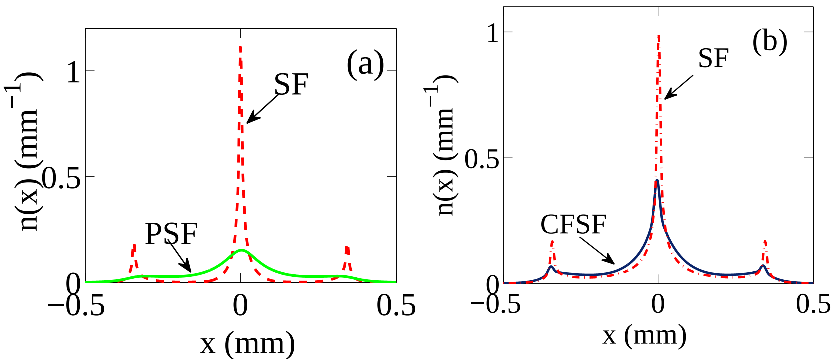

Figure 3.10: Density distribution after a time-of-flight expansion. We assume ^{87}Rb atoms and use an expansion time of 0.03s. The hopping energy is $t = 0.02U$. Panel (a): For attractive interaction U_{12}, we show the TOF expansion of a SF state at $U_{12} = -0.01U$ (red line) and of a PSF state at $U_{12} = -0.21U$ (green line). The two curves correspond to the expansion of the densities shown as curve I and III in Fig. 3.9(a) The trap frequency is $\Omega = 1 \times 10^{-5}U$. Panel (b): For repulsive interaction, we show a TOF expansion of a SF state at $U_{12} = 0.01U$ and of a CFSF state at $U_{12} = 0.21U$. The trap frequency is $\Omega = 8 \times 10^{-5}U$.

where $w(x,T) = \sqrt{d/\sqrt{2\pi}\Delta(T)^2}\exp(-x^2/(4\Delta(T)^2))$ describes the free expansion from the initial Gaussian wave-function of an atom in a lattice site and $\Delta(T)^2 = d^2 + iT\hbar/(2m)$. The parameter d is the width of the initial Gaussian state and m is the atomic mass. The density distribution $n_a(x,T)$ is then given by

$$n_a(x,T) = \sum_{j_1,j_2=1}^{N} w^*(x - r_{j_1}, T)w(x - r_{j_2}, T)G(j_1, j_2),$$

where $G(j_1, j_2)$ is the single-particle Green's function. In Fig. 3.10 we show examples of TOF expansions of PSF, CFSF, and SF order. For the SF phase, we find a strongly peaked interference pattern, reflecting the single-particle quasi-long range order. For both PSF and CFSF phases, the TOF density shows a broad Lorentzian distribution, which is due to the exponential decay of the single-particle Green's function.

Feshbach ramp: In order to detect the superfluidity of pairs, we consider applying a Feshbach ramp to pairwise project the atoms onto molecules formed by one atom from each species, which is similar to detection of fermionic pairs in the BCS regime [55]. In those experiments, a fast ramp across a Feshbach resonance was used, followed by a time-of-flight expansion. The density distribution of the molecules showed the superfluidity of fermionic pairs. We propose a similar detection for bosonic pairs in PSF.

To give a simple estimate of a TOF image after a Feshbach ramp, we imagine that bosons of different species on the same lattice site are converted into molecules. This leads to the replacement $b_{1,j}b_{2,j} \to M_j$, where M_j is the molecule annihilation operator. A TOF density of the molecules at position x and time T is given by

$$n_M(x,T) = \sum_{j_1,j_2=1}^{N} w^*(x - r_{j_1}, T) w(x - r_{j_2}, T) R_s(j_1, j_2). \tag{3.33}$$

In the expanding wave function $w(x,T)$, the mass m is replaced by the mass of the molecule. We assume the same initial width d. In a more realistic estimate, the conversion efficiency to molecules would not be 100%, but approximately given by the square of the overlap of the molecular wave function and the single-atom wave functions. This leads to a reduced signal. The spatial dependence, however, remains the same. In Fig. 3.11, we see an example of the density of molecules after TOF and, for comparison, the atomic density after TOF for the PSF state. The strongly peaked molecular distribution indicates the quasi-condensate of the bosonic pairs. The single-atom density is a broad Lorentzian distribution, indicating the absence of single-particle SF.

Bragg spectroscopy: To detect the presence of CDW order, one can use Brag spectroscopy [66, 67]. The quantity that is measured in those experiments is either the dynamic or static structure factor. Here we calculate the static structure factor $S_a(k)$ for species $a = 1, 2$. It is defined as

$$\begin{aligned} S_a(k) &= \frac{1}{N} \sum_{j_1,j_2} e^{-ika_L(j_1-j_2)} (\langle n_a(j_1) n_a(j_2) \rangle \\ &\qquad - \langle n_a(j_1) \rangle \langle n_a(j_2) \rangle) \, . \end{aligned} \tag{3.34}$$

For wave vectors k near twice the "Fermi wavevector" k_F, the structure factor $S(k) \sim ||k| - 2k_F|^{1-\alpha_{CDW}}$ with $\alpha_{CDW} = 2 - K_S - K_A$ [24]. In our system, $K_S + K_A$ is always larger than 1 and, thus, $1 - \alpha_{CDW}$ is positive. Consequently, the structure factor does not diverge. In the CDW regime with $K_S + K_A < 2$ the power $1 - \alpha_{CDW}$, however, is less than one.

This gives $S(k)$ cusps at $\pm 2k_F$ when CDW quasi-long range order is present. In Fig. 3.12 we show examples of $S(k)$ for a case with and without CDW.

Bragg Spectroscopy preceded by a π/2 pulse: To detect CFSF order, we propose the following detection method. It applies to the case that the mixture is composed of atoms in different internal states rather than different atomic species. First, we apply a $\pi/2$ pulse, which transfers the atoms into the superpositions $b_{1/2,i} \rightarrow b_{\pm,i} = (b_{1,i} \pm b_{2,i})/\sqrt{2}$. We then measure the structure factor, which now corresponds to the Fourier transform of the density correlations $R_{n\pm}(i,j) = \langle n_{\pm,i} n_{\pm,j} \rangle - \langle n_{\pm,i} \rangle \langle n_{\pm,j} \rangle$. In terms of the original $b_{1/2,i}$ operators these density correlations are given by

$$\begin{aligned} R_{n\pm}(i,j) &= \frac{1}{4}\langle (n_{1,i}+n_{2,i})(n_{1,j}+n_{2,j})\rangle \\ &\quad -\frac{1}{4}(\langle n_{1,i}\rangle + \langle n_{2,i}\rangle)(\langle n_{1,j}\rangle + \langle n_{2,j}\rangle) \\ &\quad +\frac{1}{2}\langle b^\dagger_{1,i} b_{2,i} b^\dagger_{2,j} b_{1,j}\rangle \end{aligned} \tag{3.35}$$

The last term in the above equation is the correlation function $R_a(i,j)$ of the order parameter of CFSF, $b_{1,j} b^\dagger_{2,j}$. In Fig. 3.13, we show the structure factor $S_+(k)$, the Fourier transform of Eq. 3.35, as well as the Fourier transform of $R_a(i,j)$. Both $S_+(k)$ and the Fourier transform of $R_a(i,j)$ have a cusp around $k=0$. The cusp is due to the long-range correlations of the anti-pairs in the CFSF. The two functions are nearly identical near $k=0$, indicating that the momentum distribution of anti-pairs can be measured by determining the structure factor $S_+(k)$.

3.5 Summary

We have studied ground state properties of one-dimensional Bose mixtures in an optical lattice using both Tomonaga-Luttinger liquid theory and the time-evolving block decimation method. We first discussed the zero-temperature phase diagram in a homogeneous system at different filling fractions and different parameter regimes. We have shown that 1D Bose mixtures in an optical lattice can have quasi-long range orders that include superfluid, paired superfluid (PSF), counterflow superfluid (CFSF), and Mott insulator. We also found that each type of superfluid order can coexist with charge density wave (CDW) order and that in both PSF and CFSF phases single particle superfluidity (SF) is absent.

In addition, we discussed ways of realizing and detecting these phases experimentally. We propose using a Feshbach ramp to probe the momentum distribution of pairs in the PSF, which shows signatures of the quasi-condensate of pairs. To detect the CFSF for a mixture composed of two atomic hyperfine states, we propose to measure the static structure factor by using Bragg spectroscopy preceded by a $\pi/2$ pulse. A sharp peak in the structure factor was shown to be dominated by the contribution from the momentum distribution of anti-pairs in the CFSF phase. Finally, we suggest to detect CDW order with Bragg spectroscopy.

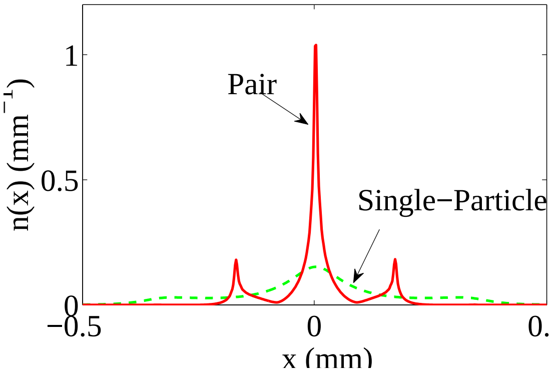

Figure 3.11: Density distribution of molecules after time-of-flight expansion of state III in Fig. 3.9(a). The expansion time is 0.03s. We assume two hyperfine states of ^{87}Rb. These are converted into Feshbach molecules at $T = 0$ via a fast ramp across a resonance. We assume a complete conversion. The strongly peaked interference pattern of molecules indicates the presence of a quasi-condensate of pairs. For comparison, we also show the TOF expansion of atoms in the PSF phase for the same parameters. The broad Lorentzian distribution demonstrates the absence of single-particle SF.

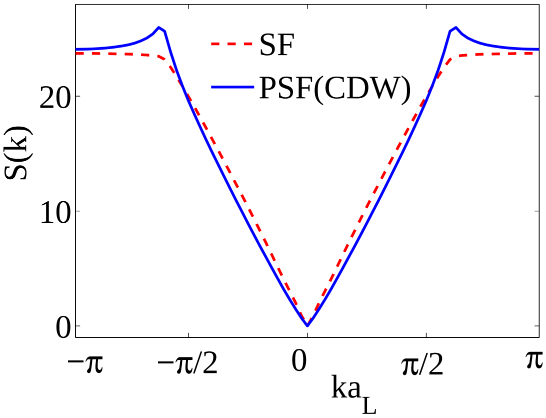

Figure 3.12: Structure factor at filling $\nu = 0.3$. For $U_{12} = -0.01U$ the system is in the SF regime (dashed line) and for $U_{12} = -0.07U$ the system is in the PSF regime (continuous line). Cusps at $|k| = 2\pi\nu$ only occur for $U_{12} = -0.07U$ indicating the coexistence of CDW with PSF order.

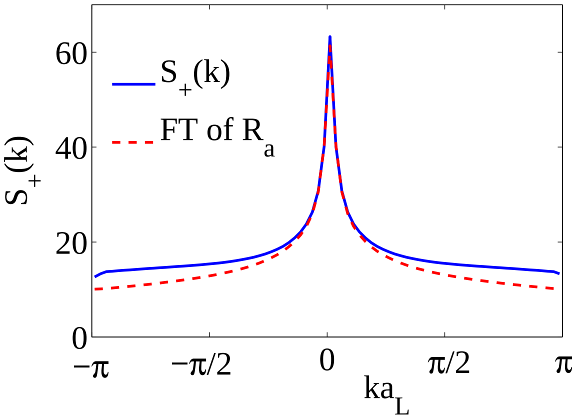

Figure 3.13: Structure factor $S_+(k)$ (blue line) after applying a $\pi/2$ pulse in the CFSF phase. The quasi-condensate of anti-pairs generates an algebraic peak at $k = 0$. The cusp also appear in the Fourier transform of the anti-pair correlation function $R_a(i,j) = \langle b_{1,i}^\dagger b_{2,i} b_{2,j}^\dagger b_{1,j} \rangle$(red dashed line).

Chapter 4

One dimensional binary Bose mixtures in optical lattices (II): noise correlation

In Chapter 1, we have discussed the study of noise correlations as a way of probing ultracold atom systems. The noise correlations are measured as the spatial correlations of the density in the fully expanded atomic cloud after turning off the trap. If atomic interactions during the expansion can be ignored, one can use the noise correlation measurements to infer momentum space correlations in the initial state. Such an analysis has been used to demonstrate the phase transition between superfluid (SF) and Mott insulator (MI) states [31, 32], as well as the formation of fermionic pairs [33]. In Refs. [38, 36], noise correlations were shown to be an effective probe of such orders in 1D Fermi systems, for both one- and two-component systems. Similar studies have been done for 1D bosonic systems, either in the hard-core limit [40] or using Luttinger liquid (LL) theory [35]. In Ref. [35], the signature of condensates and quasi-condensates was discussed in detail.

Noise correlations can also be used to study the phases of binary bosonic mixtures. In the previous chapter, we established the phase diagram of a binary mixture exhibiting SF, PSF, CFSF and MI orders, and we showed that each of the superfluid orders can coexist with the CDW order. We also show that because the PSF and CFSF orders are the result of inter-species pairing, they do not provide a signature in the momentum distributions of the individual atomic species. In this paper, we show that noise correlation measurements provide *distinctive* signals of both the PSF and CFSF orders. Ref. [71] shows that noise correlations characteristic of the PSF/CFSF orders can be observed even in a system of only four atoms. Here we calculate the noise correlation spectra from the ground state obtain by the TEBD method, which is supported by analytical calculations based on LL theory. We make appropriate comparisons between results for homogeneous and trapped systems.

To evaluate the noise correlations, we first assume ballistic expansion and long expansion time and define the noise correlations as the density correlations in momentum space,

$$\mathcal{G}_{aa'}(k,k') \quad = \quad \langle n_{a,k}n_{a',k'}\rangle - \langle n_{a,k}\rangle\langle n_{a',k'}\rangle \tag{4.1}$$

where a, a' are species indices ($a, a' = 1, 2$), k, k' are momenta, and $n_{a,k}$ and $n_{a',k'}$ are the occupation operators in momentum space. We also consider the derived quantities $C_{aa'}(q)$ and $D_{aa'}(q)$, defined as

$$C_{aa'}(2q) = \int dk \frac{\langle n_a(k+q)n_{a'}(k-q)\rangle}{\langle n_a(k+q)\rangle\langle n_{a'}(k-q)\rangle}, \tag{4.2}$$

and

$$D_{aa'}(2q) = \int dk \frac{\langle n_a(k+q)n_{a'}(q-k)\rangle}{\langle n_a(k+q)\rangle\langle n_{a'}(q-k)\rangle}. \tag{4.3}$$

Each of these quantities can capture the main features of the noise correlations for particular types of order and can be directly measured in experiments [32]. We will present all our results first in the form of $\mathcal{G}_{aa'}(k,k')$ and then use $C_{aa'}(q)$ and $D_{aa'}(q)$ to highlight the key features.

This chapter is organized as follows: in Sec. 4.1, we first summarize the different quasi-orders discussed in the previous chapter and introduce the noise correlations in such mixture; in Sec. 4.2, we show our LL results and predict the generic signature of the noise correlations for different orders. In Sec. 4.3, we present our numerical calculation of noise correlations for both homogeneous and trapped systems. In Sec. 4.4 we summarize the main features of the noise correlations for 1D binary Bose mixtures.

4.1 Noise correlations and quasi-orders

In previous chapter, we discuss the phase diagram for the binary Bose mixtures in optical lattices and show that the single-species superfluid (SF) has the order parameter $b_a(x)$ ($a = 1, 2$) and its corresponding correlation function $G(x) = \langle b_a^\dagger(x)b_a(0)\rangle$; the paired superfluid (PSF) has the order parameter $b_1(x)b_2(x)$ and its corresponding correlation function $R_S(x) = \langle b_1^\dagger(x)b_2^\dagger(x)b_1(0)b_2(0)\rangle$; the counter-flow superfluid (CFSF) has the order parameter $b_1(x)b_2^\dagger(x)$ and its corresponding correlation function $R_A(x) = \langle b_1^\dagger(x)b_2(x)b_1(0)b_2^\dagger(0)\rangle$. The CDW order parameter is $n_a(x)$ ($a = 1, 2$) and the corresponding correlation function $R_{n,a}(x) = \langle n_a(x)n_a(0)\rangle$. The asymptotic behavior of the correlation functions at large x is listed in Table. 3.1.

We calculate the noise correlations from the four-point correlation function:

$$\mathcal{G}_{aa'}(k,k') = \sum_{j_1,,j_2,j_3,j_4=1}^{N} \mathcal{L}_{aa'}(j_1,j_2,j_3,j_4)e^{i[kj_{12}+k'j_{34}]} - \langle n_a(k)\rangle\langle n_{a'}(k')\rangle, \tag{4.4}$$

$$\tag{4.5}$$

where $j_{12} \equiv j_1 - j_2$, $j_{34} \equiv j_3 - j_4$ and $\mathcal{L}_{aa'}$ is the four-point correlation function,

$$\mathcal{L}_{aa'}(j_1,j_2,j_3,j_4) = \langle b_{a,j_1}^\dagger b_{a,j_2} b_{a',j_3}^\dagger b_{a'j_4}\rangle. \tag{4.6}$$

It is easy to see that the correlation functions R_S, R_A and $R_{n,a}$ are the special cases of $\mathcal{L}_{aa'}$,

$$\begin{aligned}
\mathcal{L}_{12}(j_1,j_2,j_1,j_2) &= R_S(j_1,j_2), \\
\mathcal{L}_{12}(j_1,j_2,j_2,j_1) &= R_A(j_1,j_2), \\
\mathcal{L}_{aa}(j_1,j_2,j_2,j_1) &= R_{n,a}(j_1,j_2) + n_{a,j_1}.
\end{aligned} \tag{4.7}$$

The noise correlation $\mathcal{G}_{12}$, therefore, contains the Fourier transform of R_S and R_A,

$$g_S(k,k') = \sum_{j_1,j_2} R_S(j_1,j_2)e^{i(k+k')(j_1-j_2)} \tag{4.8}$$

and

$$g_A(k,k') = \sum_{j_1,j_2} R_A(j_1,j_2) e^{i(k-k')(j_1-j_2)} \tag{4.9}$$

and $\mathcal{G}_{aa}$ contains the Fourier transform of $R_{n,a}$,

$$g_{n,a} = \sum_{j_1,j_2} R_{n,a}(j_1,j_2) e^{i(k-k')(j_1-j_2)}. \tag{4.10}$$

If $R_S(j_1,j_2)$ decays as $|j_1 - j_2|^{-1/K_S}$, we find that g_s scales as $|k+k'|^{-1/K_S}$. Similarly, if R_A decays as $|j_1 - j_2|^{-1/K_A}$, g_A scales as $|k-k'|^{-1/K_A}$. For the PSF phase, we find that $g_s(k,k')$ is the dominant term of $\mathcal{G}_{12}(k,k')$ with a strong peak around $k = -k'$. This peak is the signal of the PSF order. Similarly, for the CFSF phase, we find that the function $g_A(k,k')$ becomes dominant around $k = k'$ in $\mathcal{G}_{12}(k,k')$. The peak around $k = k'$ is the signal of the CFSF order. These remarks are made to give the reader an intuitive interpretation of the relationship between the noise correlations and the long-range orders. In the following section, we will explain the calculation of the noise correlations via LL theory and show that the features mentioned above are indeed reflected in the LL calculation results.

4.2 Luttinger liquid approach

In this section we determine the generic behavior of the noise correlations using a Luttinger liquid approach. This formalism has been applied to one-dimensional Fermi systems in Ref. [36], and additionally to single-species bosonic systems in Ref. [35], where a detailed description of these calculations was given. Here, we use an analogous derivation for the case of a bosonic mixture. We outline key steps of the derivation, but refer the reader to Ref. [35] for a detailed description of the method.

As described in Chapter 3, we use the Luttinger liquid theory to construct the field operator for both species [Eq. (3.2)] and obtain the action of Eq. 3.3. We calculate the noise correlations at the Gaussian fixed point, corresponding to the SF phase. Here, the system separates into symmetric and anti-symmetric degrees of freedom, defined as $\theta_{S,A} = (\theta_1 \pm \theta_2)/\sqrt{2}$ and $\phi_{S,A} = (\phi_1 \pm \phi_2)/\sqrt{2}$. The action can be written either in terms of the

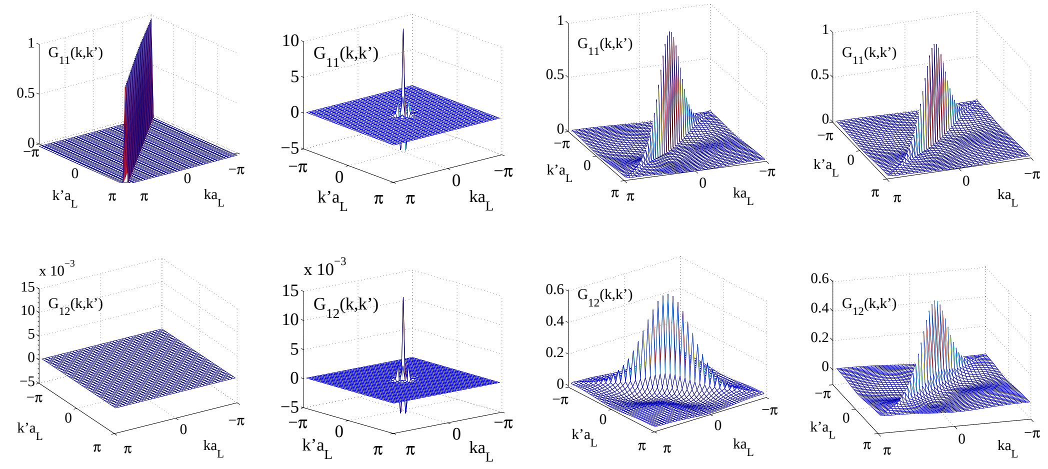

(a) MI (b) SF (c) PSF (d) CFSF

Figure 4.1: Noise correlations in different phases, derived from Luttinger liquid theory. In the MI state (column (a)), δ-function like correlations along $k = k'$ in $\mathcal{G}_{11}(k, k')$ are visible, whereas $\mathcal{G}_{12}$ nearly vanishes. In the SF state (column (b)), with Luttinger parameters $K_A = 1.03$ and $K_S = 0.96$, we find various contributions in $\mathcal{G}_{11}$, especially δ- function along $k = k'$. In Fig. 4.2, we show the contour plots for $\mathcal{G}_{11}$ and $\mathcal{G}_{12}$ for the same state, where we can see the negative correlations at $k = 0$ and $k' = 0$, as well as pairing correlation along $k = -k'$, which is similar to the single-species result in Ref. [35]. $\mathcal{G}_{12}$ shows similar features, but the bunching contribution is an algebraic peak, rather than a δ-function. In (c) we show an example for the PSF phase, with $K_A = 0.01$ and $K_S \simeq 1.3$, in (d) an example for the CFSF phase, with $K_S = 0.01$ and $K_A \simeq 1.2$. In the PSF state, the inter-species correlation $\mathcal{G}_{12}(k, k')$ has strong correlations along $k = -k'$, a reflection of pairing. In the CFSF state, the peak is formed along $k = k'$ direction, an indication of the anti-pairing (particle-hole) formation in the CFSF state.

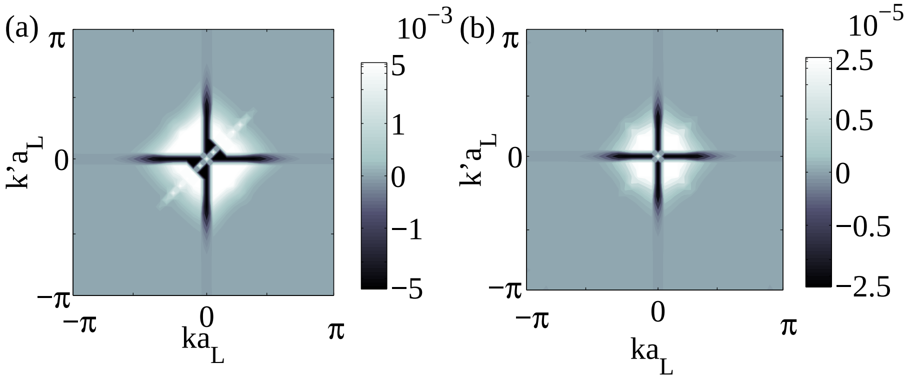

Figure 4.2: Noise correlations, $\mathcal{G}_{11}(k, k')$ (a) and $\mathcal{G}_{12}(k, k')$ (b), in the SF state. The data used here are the same as those used in Fig. 4.1 (b). We create the non-linear gray scales by plotting functions $\tanh(500\mathcal{G}_{11})$ (a) and $\tanh(10^5\mathcal{G}_{12})$ (b), in order to magnify the details around $k = k' = 0$. The labels of the color-bar reflect the values of $\mathcal{G}_{11}(k, k')$ and $\mathcal{G}_{12}(k, k')$. In these plots, we can clearly see the negative correlations between the quasi-condensate ($k = 0$ and $k' = 0$) and the higher momentum states at the quantum depletion, as well as the anti-pairing correlation along $k = k'$ and the pairing correlation along $k = -k'$.

phase fields

$$S = \sum_{j=S,A} \int d^2 r_j \Big[\frac{K_j}{2\pi}[(\partial_{v_j\tau}\phi_j)^2 + (\partial_x\phi_j)^2]\Big], \tag{4.11}$$

or in terms of the fields $\theta_{S,A}$

$$S = \sum_{j=S,A} \int d^2 r_j \Big[\frac{1}{2\pi K_j}[(\partial_{v_j\tau}\theta_j)^2 + (\partial_x\theta_j)^2]\Big]. \tag{4.12}$$

The velocities $v_{S,A}$ are the phonon velocities of the symmetric/anti-symmetric modes, and $\mathbf{r}_{S,A} = (v_{S,A}\tau, x)$. The parameters $K_{S,A}$ are the Luttinger parameters of the symmetric/anti-symmetric sector. To calculate the noise correlations away from the SF regime, we take the limits $K_{S,A} \to 0$ to describe the phases in which either or both $R_{S/A}$ have short-ranged correlations (exponential decay). This approximation corresponds to the limit that the length scale of the exponential decay is much smaller than any other length scale of the system. Our calculation could be extended in a straightforward way to include a finite decay length of the exponential decay.

We start out by calculating $\langle n_{a,k}\rangle$ for small momentum $k \approx 0$, for which the Bose operators are given by $b_a \sim \sqrt{n}e^{i\phi_a}$. For $\langle n_{a,k}\rangle$ we find:

$$\langle n_{a,k}\rangle \sim n\int dx_{12} e^{ikx_{12}} e^{-\frac{1}{2}\langle(\phi_a(2)-\phi_a(1))^2\rangle}, \tag{4.13}$$

where $\phi_a(1)$ refers to $\phi_a(x_1)$, and similarly for $\phi_a(2)$, and $x_{12} = x_1 - x_2$. The correlation function $\langle(\phi_a(2)-\phi_a(1))^2\rangle$ can be rewritten in terms of correlation functions for $\phi_{S,A}$. Using the Gaussian action above, we find

$$\langle(\phi_{S/A}(2) - \phi_{S/A}(1))^2\rangle = \frac{1}{2K_{S/A}} \log\frac{r_0^2 + x_{12}^2}{r_0^2}, \tag{4.14}$$

where r_0 is a short-range cut-off. With that we find

$$\langle n_k \rangle \sim n \int dx_{12} e^{ikx_{12}} \mathcal{F}(x_{12}), \tag{4.15}$$

where

$$\mathcal{F}(x) \quad = \left(\tfrac{r_0^2}{r_0^2+x^2}\right)^g. \tag{4.16}$$

The exponent g is given by $g = 1/8K_S + 1/8K_A$. Next we evaluate the expectation value $\langle n_k n_{k'} \rangle$ along the same lines. We obtain:

$$\langle n_{1,k} n_{1,k'} \quad \rangle \sim \quad n^2 \int e^{ikx_{12}+ik'x_{34}} \mathcal{F}(x_{12}) \mathcal{F}(x_{34}) \mathcal{A}, \tag{4.17}$$

where

$$\mathcal{A} \quad = \quad \left(\frac{(r_0^2 + x_{14}^2)(r_0^2 + x_{23}^2)}{(r_0^2 + x_{13}^2)(r_0^2 + x_{24}^2)} \right)^h, \tag{4.18}$$

and Eq. 4.17 is a volume integral over the spatial variables x_{12}, x_{23}, x_{34}. The exponent h is given by $h = -1/8K_S - 1/8K_A$. We combine these expressions to get the correlation function $\mathcal{G}_{11}(k,k')$:

$$\mathcal{G}_{11}(k,k') \quad \sim \quad n^2 \int e^{ikx_{12}+ik'x_{34}} \mathcal{F}(x_{12}) \mathcal{F}(x_{34}) (\mathcal{A} - 1). \tag{4.19}$$

For $\mathcal{G}_{12}(k,k')$ we proceed analogously, and find $h = -1/8K_S + 1/8K_A$. For the finite-size systems that we treat here, we evaluate these integrals numerically, by choosing a finite length L of the system, and by replacing each spatial variable x by $(L/2\pi)\sin(2\pi x/L)$ (see Ref. [24]). To compare with the TEBD calculations of a homogeneous system in the next section, we choose the values of the Luttinger parameters, K_A and K_S to those obtained from the TEBD calculations and they are listed in Table. 4.1.

In Fig. 4.1 (b) and 4.2, we show an example for the SF regime. In the upper panel of Fig. 4.1 (b), we show $\mathcal{G}_{11}(k,k')$, in the lower panel $\mathcal{G}_{12}(k,k')$. The Luttinger parameters are $K_A = 1.03$ and $K_S = 0.96$. The ratio L/r_0 was chosen as $L/r_0 = 20$, corresponding to the particle number of each species in the numerical example. The shape of $\mathcal{G}_{11}(k,k')$ is the same as the noise correlation function for a single bosonic SF, which was discussed in Ref. [35]. It has the characteristic features of a superfluid: positive correlations along $k = -k'$, which indicates pairing correlations; negative correlations for the axes $k = 0$ and $k' = 0$, indicating the negative correlations between the quasi-condensate and the higher momenta due to pair fluctuations; and bunching correlations along $k = k'$. For $\mathcal{G}_{12}(k,k')$ we find qualitatively a similar shape, with the main difference, that the bunching along $k = k'$ does not have a δ-function contribution, but only algebraic terms. We note that for a system of two non-interacting species, i.e. for $U_{12} = 0$, $K_S = K_A$, and $\mathcal{G}_{12}$ vanishes.

In Figs. 4.1 (c) and (d) we show the noise correlations for the PSF and the CFSF phase, respectively. For the PSF example, the Luttinger parameters are $K_S = 1.3$ and $K_A = 0.01$. For L/r_0 we again pick $L/r_0 = 20$. For the CFSF phase, the parameters are $K_A = 1.2$ and $K_S = 0.01$. In the PSF regime, we find a strong pairing signature in $\mathcal{G}_{12}$, similar to the pairing signature in Fermi mixtures [36, 35]. In the CFSF example, an strong anti-pairing signature is found in $\mathcal{G}_{12}$.

We can obtain the functional form of these signatures in the limit $L \to \infty$, by applying similar arguments to what has been given in Ref. [35]. In the PSF region, We rewrite the noise correlation integral in terms of $z = (x_{12} - x_{34})/2$, $h_+ = (x_{14} + x_{23})/2$ and $h_- = (x_{14} - x_{23})/2$. We then note that for $\mathcal{G}_{12}$ and for $K_A \to 0$, the exponent $h = -1/8K_S + 1/8K_A$ diverges. This enforces the integrand to be negligible away from z, $h_+ \approx 0$. Thus the integral evaluates to

$$\mathcal{G}_{12} \quad \sim \quad |k + k'|^{-1/K_S}. \tag{4.20}$$

This is the shape that would be approached in an infinite system by the noise correlations shown in Fig. 4.1 (c), lower panel. The deviation from the pure power law is due to the finite size of the system. With similar arguments one can show that in the CFSF regime the inter-species noise correlation approaches

$$\mathcal{G}_{12} \sim |k-k'|^{-1/K_A}, \tag{4.21}$$

for $L \to \infty$. Again, the deviation from a pure power law is due to the finite size of the system. Furthermore, one can show that for both PSF and CFSF orders, $\mathcal{G}_{11}(k,k')$ approaches $\delta(k-k')$, in the limit of infinite size. Equations 4.20 and 4.21 show that there is a simple relationship between $\mathcal{G}_{12}$ and K_S in the PSF regime and $\mathcal{G}_{12}$ and K_A in the CFSF regime. This suggests that a careful measurement of $\mathcal{G}_{12}$ can be used to extract the value of the Luttinger parameters appropriate to the system. This is further confirmed by our numerical calculations for a trapped system, where we show that the algebraic relationship described by Eqs. 4.20 and 4.21 remains valid in the presence of a harmonic trap. We discuss prospects for experimental determination of Luttinger parameters in Sec. 4.3.3.

The MI result in Fig. 4.1 (a) is obtained by setting both K_A and K_S to 0.01. In this case, the ground state closely approximates a simple product of MI states of each species. Thus, $\mathcal{G}_{11}$ approaches a δ-function, whereas $\mathcal{G}_{12}$ nearly vanishes.

Next we calculate the noise correlations for the case $k \approx 0$ and $k' \approx 2k_F$, where k_F is the Fermi wavevector defined above. Essentially the same calculation can be done for $k' \approx -2k_F$, and $k' \approx 0$ and $k \approx \pm 2k_F$. $n_{a,k}$ is still given by the expression (4.15), but $n_{a,k'}$ now needs to be calculated with the operator representation $b(x) = \sqrt{n}\exp(2i\Theta(x))\exp(i\phi(x))$. With that we find

$$\langle n_{q'+2k_F} \rangle \sim n \int dx_{12} e^{iq'x_{12}} \mathcal{F}'(x_{12}), \tag{4.22}$$

where $\mathcal{F}'(x_{12})$ has the same form as before but with an exponent $g' = 1/8K_S + 1/8K_A + (K_S+K_A)/2$. The noise correlations take the form

$$\mathcal{G}_{11}(k,q') \sim n^2 \int e^{ikx_{12}+iq'x_{34}} \mathcal{F}(x_{12})\mathcal{F}'(x_{34})(\mathcal{A}-1). \tag{4.23}$$

Parameter setting	Order	Luttinger Parameters
(a) $U_{12}/U = 0.01, \nu = 1$	MI	$K_A = K_S = 0$
(b) $U_{12}/U = 0.01, \nu = 0.5$	SF	$K_A \simeq 1.03, K_S \simeq 0.96$
(c) $U_{12}/U = -0.11, \nu = 0.5$	PSF	$K_A = 0, K_S \simeq 1.3$
(d) $U_{12}/U = 0.11, \nu = 0.5$	CFSF	$K_A \simeq 1.2, K_S = 0$
(e) $U_{12}/U = 0.26, \nu = 0.2$	SF & CDW	$K_A \simeq 1.4, K_S \simeq 0.57$

Table 4.1: The parameters used in the numerical examples and the Luttinger parameters extracted from the algebraic fit of correlation functions, R_A and R_S. The Luttinger parameters are set to zero when the correlations decay exponentially. The hopping parameter t is $0.02U$ for all cases. The parameters are chosen to represent different orders that can exist in this system.

We therefore note that around the points $k \approx 0$ and $k' \approx \pm 2k_F$, and $k \approx \pm 2k_F$ and $k' \approx 0$ the integrand is multiplied by a contribution that is of the form of the integrand of the static structure factor

$$S(q) \sim \int e^{iqx_{12}} \left(\frac{r_0^2}{r_0^2 + x_{12}^2} \right)^{(K_S+K_A)/2} , \tag{4.24}$$

which can create cusps in the noise correlation when the system is in the CDW regime. These cusps are found in our numerical calculations and are discussed in the next section.

4.3 Numerical approach

The calculation of noise correlations is based on the ground state generated by the TEBD method. We set the Schmidt rank $\chi = 100$ and the local dimension $d = 5$. We use imaginary-time propagation to generate the ground state. After obtaining the ground state, we calculate the correlation functions, R_A, R_S, $R_{n,a}$ and G, and determine the quasi-long range order present in the system based on the relationship shown in Table. 3.1. Furthermore, we can extract the value of the Luttinger parameters, K_A and K_S, from the numerically calculated correlation functions. We use these parameters in a Luttinger Liquid calculation to compare the numerical and the analytical results.

The main challenge of determining the noise correlation functions is the high computational cost of calculating the four-point function, $\mathcal{L}_{aa'}(j_1, j_2, j_3, j_4)$ (Eq. 4.6), which is estimated to scale as $\chi^3 d^3 N^4$. For the system sizes used in this paper, we use parallel com-

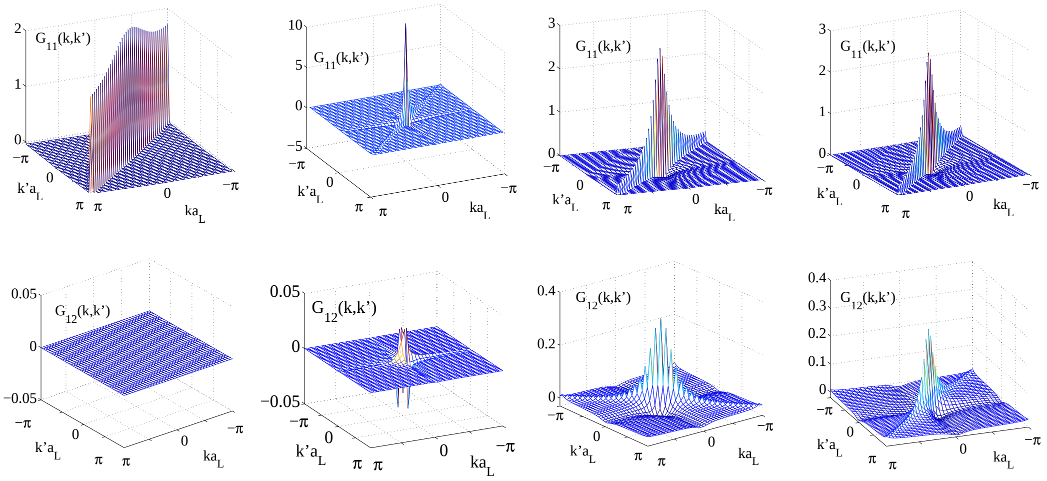

(a) MI (b) SF (c) PSF (d) CFSF

Figure 4.3: Noise correlations for a homogeneous system of 40 lattice sites, calculated with the TEBD method. The frames (a) – (d) correspond to the examples (a) – (d) in Table 4.1. In (a), we show the noise correlations of a MI state. In the plot of $\mathcal{G}_{11}(k,k')$, there is a strong correlation along the direction $k = k'$, whereas the noise correlation function $\mathcal{G}_{12}(k,k')$ essentially vanishes. In (b), we show the noise correlations of a SF state. Here, we can see the peak around $k = k'$ corresponding to the δ- function bunching peak predicted by Luttinger Liquid theory (see also Fig. 4.1 (b)). For $\mathcal{G}_{12}$, we find negative value at $k = k' = 0$, which is different from the Luttinger Liquid result (Fig. 4.1 (b)). Other structures predicted by Luttinger Liquid theory can be seen in Fig. 4.4, where $\mathcal{G}_{12}$ and $\mathcal{G}_{11}$ are plotted in a non-linear color scale to magnify the structures around $k = k' = 0$. In (c) and (d), we show the noise correlations of the PSF and CFSF state, respectively. In the PSF state (c), the inter-species correlation $\mathcal{G}_{12}(k,k')$ has strong correlations along $k = -k'$, a consequence of pairing (see also Fig. 4.1 (c)). In the CFSF state (d), the peak is formed along the direction $k = k'$, an indication of anti-pairing in the CFSF state (see also Fig. 4.1).

puting algorithms to speed up the calculation by parallelization the computation of $\mathcal{L}_{aa'}$ along the indices j_i.

4.3.1 Homogeneous systems

In this section we discuss the numerical results for noise correlations of a homogeneous system of 40 lattice sites, subject to the hard-wall or "open" boundary condition, in which the wave function is required to vanish on the fictitious sites of index 0 and $N + 1$ implied by Eq. 3.1. We consider five parameter sets listed in Table 4.1, representing different regimes of the phase diagram of 1D Bose mixtures.

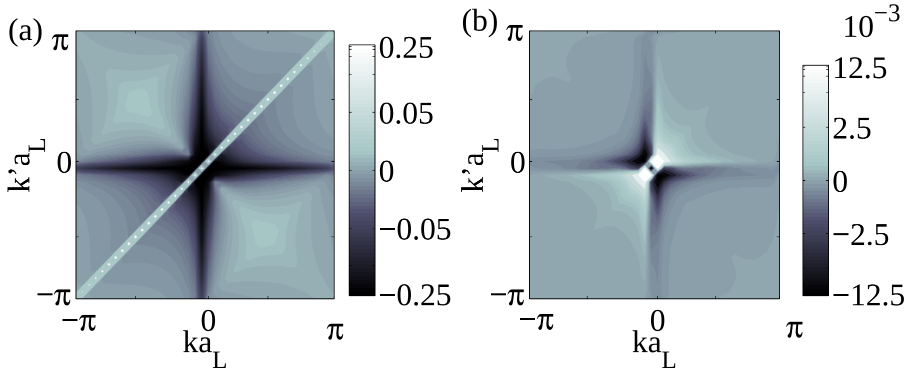

Figure 4.4: Noise correlations, $\mathcal{G}_{11}(k,k')$ (a) and $\mathcal{G}_{12}(k,k')$ (b), in the SF state of a homogeneous system. The values of $\mathcal{G}_{11}(k,k')$ and $\mathcal{G}_{12}(k,k')$ are exactly the same as in Fig. 4.3 (b). We create non-linear gray scales by plotting $\tanh(10\mathcal{G}_{11})$ and $\tanh(200\mathcal{G}_{12})$ in linear scales. The labels of the color-bar reflects the values of $\mathcal{G}_{11}(k,k')$ and $\mathcal{G}_{12}(k,k')$. The features around $k=k'=0$ are magnified as a result of the non-linear scale. In (a), we find the features predicted by LL calculations (4.2 (a)). In addition, we can see a weak correlation at around $k=k'\pm 2k_F$, where $k_F=\nu\times\pi/a_L=0.5\pi/a_L$. This is where a strong correlation (cusps) will develop if CDW order is present. This feature can also been shown in Luttinger Liquid calculations at around $k\approx 0$ and $k'\approx 2k_F$ (Eq. 4.23). In (b), we find that the structures along $k=k'$ is similar with the ones in Luttinger Liquid calculations, however, the structures along $k=-k'$ is negative, different from the Luttinger Liquid predictions (see also Fig. 4.2). The difference may be understood as a result of different boundary conditions used for the finite-size calculations: the numerical calculations use a "hard-wall" boundary condition, whereas the Luttinger Liquid calculations assume a periodic boundary condition.

For the Hamiltonian of Eq. 3.1, in the non-interacting case, $U_{12} = 0$, SF and MI are the only two possible orders. In the interacting case, SF and MI orders are still encountered, when the inter-species interaction is weak. For the Hamiltonian of Eq. 3.1 with $t \ll U$, the MI state exists for any $|U_{12}| \lesssim U$, until the occurrence of collapse ($U_{12} \lesssim -U$) or phase separation ($U_{12} \gtrsim U$). The SF state however exists only when $|U_{12}| \ll U$. In either of SF or MI phases, the quasi-order is formed in each individual species and the cross-species correlation is weak.

For the MI state (Fig. 4.3 (a)) we find that $\mathcal{G}_{11}(k', k)$ shows strong correlations along the direction $k' = k$, in agreement with the LL theory result shown in Fig. 4.1 (a). We also find that the correlations along $k' = k$ are not uniform and that the peak along $k' = k$ resembles a Lorentzian distribution in k imposed upon a constant. This Lorentzian is due to the characteristic scale of the correlation functions. This contribution was ignored in the before-mentioned approximation in the LL calculation, but could be included in a straightforward manner. The cross-species noise correlation, $\mathcal{G}_{12}(k, k')$, on the other hand, is essentially zero, indicating the absence of cross-species correlations in the MI state. For the SF state (Fig. 4.3 (b) and Fig. 4.4), we consider the case where there is weak repulsion between the two species (Table 4.1 (2)). The Luttinger parameters are $K_A = 1.03$ and $K_S \simeq 0.96$, which were extracted from the correlation functions R_S and R_A by numerical fitting. From the upper panel in 4.3 (b), we see that $\mathcal{G}_{11}$ has the characteristic features of a quasi-condensate [35]: the positive correlations along $k = -k'$, which indicate pairing; the negative correlations between $k = 0$ and finite k', as well as between $k' = 0$ and finite k; and a δ-function like correlation along $k = k'$, corresponding to bosonic bunching. The lower panel in Fig. 4.3 (b), we see $\mathcal{G}_{12}$, which shows similar features, except for the δ-function along $k = k'$, which is "softened" into a power-law divergence and a slight negative value at $k = k' = 0$. For a system of two non-interacting superfluids, i.e. $U_{12} = 0$, we have $K_S = K_A$, and $\mathcal{G}_{12} = 0$.

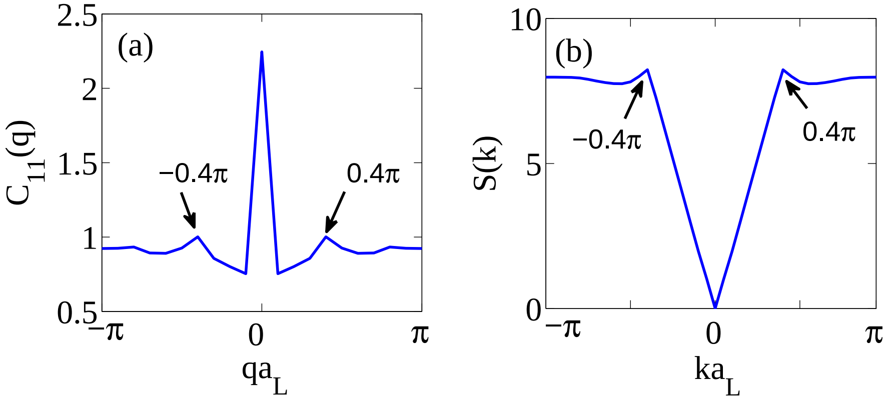

Figure 4.5: Left : The correlation function $C_{11}(q)$, as defined in Eq. 4.2; right: the structure factor $S(k)$ for a quasi-supersolid state. The parameters are given in example (5) of Table. 4.1. The Luttinger parameters are $K_A \approx 1.4$ and $K_S \approx 0.57$. The filling fraction is $\nu = 0.2$, hence the "Fermi wave vector" k_F is $\pi \times 0.2$. At momentum $2k_F$, both quantities develop cusps, indicating the presence of CDW order.

Paired superfluid and counter-flow superfluid

We now discuss the noise correlations of the PSF and CFSF states. The noise correlation $\mathcal{G}_{12}(k,k')$ is particularly important for these two phases, because it can verify the existence of PSF and CFSF orders. Unlike SF and MI states, PSF and CFSF states are characterized by order parameters that contain both species and therefore cannot be reflected in any single-species observables, such as the single-particle Green's function, $G_a(x)$ or the single-particle momentum distribution [70]. The noise correlation function $\mathcal{G}_{12}(k,k')$ measures the correlations between the momentum occupancies of the two species, and thus provides a direct probe of these orders. We have shown in the previous section, that the peak along $k=-k'$ in $\mathcal{G}_{12}(k,k')$ indicates the PSF order and that along $k=k'$ indicates the CFSF order. These features are verified in our numerical calculation of $\mathcal{G}_{12}$ from the ground state.

In Fig. 4.3 (c), we show the noise correlations in the PSF state. The parameters are listed in (c) of Tab. 4.1. The existence of PSF order is - as usual - determined by the behavior of the $R_S(x)$ and $R_A(x)$. $R_A(x)$ decays exponentially and $R_S(x)$ algebraically with Luttinger parameter $K_S \simeq 1.3$. For the noise correlation function $\mathcal{G}_{12}(k,k')$, we find that a peak is formed along $k=-k'$, which is a consequence of the pairing correlations. In Fig. 4.3 (d), we show our numerical results for the CFSF example (d) in Table 4.1. Based on the behavior of the $R_S(x)$ and $R_A(x)$ we verify that the system is in a CFSF state with $K_A \simeq 1.2$, and an exponentially decaying $R_S(x)$. For $\mathcal{G}_{12}$ we find that a peak is formed along the diagonal direction, as a result of correlations of anti-pairs ($b_1 b_2^\dagger$). These findings are consistent with the predictions of LL theory (see Fig. 4.1). We note that $\mathcal{G}_{12}(k, k')$ is enhanced in magnitude in the PSF and the CFSF phase compared to the MI and the SF phase, with a strongly altered functional form.

Charge density wave

In certain parameter regimes of the phase diagram, charge density wave (CDW) order can coexist with each of the three superfluid orders, SF, PSF and CFSF. In Sect. 4.2, we use LL theory to show that CDW order can be reflected in the function $\mathcal{G}_{11}$ and that the behavior of $\mathcal{G}_{11}$ around $k = k' \pm 2k_F$ resembles the structure factor $S(k)$. The reason for the resemblance can be understood in a simple way, by recalling the definition of the structure factor

$$S(k) = \frac{1}{N} \sum_{j_1, j_2} e^{-ik(j_1 - j_2)} (\langle n_{j_1} n_{j_2} \rangle - \langle n_{j_1} \rangle \langle n_{j_2} \rangle). \tag{4.25}$$

As mentioned in Sect. 4.1 the density correlation function is "contained" in the noise correlations and the term ,

$$\sum_{j_1, j_2 = 1}^{N} \langle b_{1,j_1}^\dagger b_{1,j_2} b_{1,j_2}^\dagger b_{1,j_1} \rangle e^{i[k(j_1 - j_2) + k'(j_2 - j_1)]},$$

is part of the full sum that needs to be taken for $\mathcal{G}_{11}$. This term can also be written as a function of the density operator, $n_j = b_j^\dagger b_j$, as

$$\sum_{j_1, j_2 = 1}^{N} \langle n_{j_1} n_{j_2} \rangle e^{-i(k' - k)(j_1 - j_2)} + \delta(k - k') \langle n_{j_1} \rangle e^{-i(k' - k) j_1}$$

This shows that $\mathcal{G}_{11}$ and $S(k)$ (Eq. 4.25) have the same Fourier transform of the density correlation function. If $S(k)$ develops cusps at $\pm 2k_F$, where $k_F = \pi\nu$ [70], when CDW order is present, we expect $\mathcal{G}_{11}$ to have similar cusps at $k = k' \pm 2k_F$. In Fig. 4.5, we show one example of a quasi-supersolid (SS) state [39], where CDW order coexists with SF order.

The parameters are listed in (e) of Table 4.1. In the plot, the correlation function $C_{11}(q)$, an integration of $\mathcal{G}_{11}(k,k')$ along the direction $k=k'$ (Eq. 4.2), is compared with the structure factor $S(k)$ of the same state. In both functions, we can see cusps appearing at $\pm 2k_F$.

4.3.2 Trapped systems

We now discuss how the different types of order are affected by the presence of a trapping potential. To simulate the effect of a trap, we add a harmonic potential, $\Omega(j-j_c)^2(n_{1,j}+n_{2,j})$ to the Hamiltonian in Eq. 3.1, where j is the site index and j_c is the index at the center of the system. We then use the TEBD method to calculate the ground state. We also increase the system size to 80 lattice sites, and choose the total number of particles and the trap frequency to ensure that the boundary effect is negligible.

One interesting feature of a trapped system is that different orders can coexist in the trap. A well-known example is the MI plateau at the center of the trap surrounded by a SF at the edge [72]. For repulsive inter-species interaction, we find coexistence of a CFSF plateau with a SF at its edge and a MI plateau with PSF at the edges for attractive inter-species interactions [70]. Despite the potential complication of coexistence of orders, we find clear signals for the pairing correlations of the PSF phase and the anti-pairing correlations of the CFSF phase.

In Fig. 4.6, we show the behavior of $\mathcal{G}_{12}(k,k')$ in four different cases, where the orders at the center of the trap are SF, MI, PSF and CFSF respectively. We find that the general behavior of the noise correlation in a trap is very similar to its homogeneous counterpart. In Fig. 4.6 (c) and (d), $\mathcal{G}_{12}$ shows clearly the feature of pairing correlations in the PSF state and the anti-pairing correlations in the CFSF state. In addition, we see some minor features attributed to the coexisting orders. In the case of CFSF in a trapped system, we can see the "dip" along $k=0$ and $k'=0$ because of the coexistence with the SF order. On the other hand, in the case of a MI in a trap, we can see pairing correlations as a result of the residual PSF state at the edges. This pairing signal is much smaller than when the whole system is in the PSF state.

To show that the peaks along $k=k'$ and $k=-k'$ in $\mathcal{G}_{12}$ are detectable in experiments,

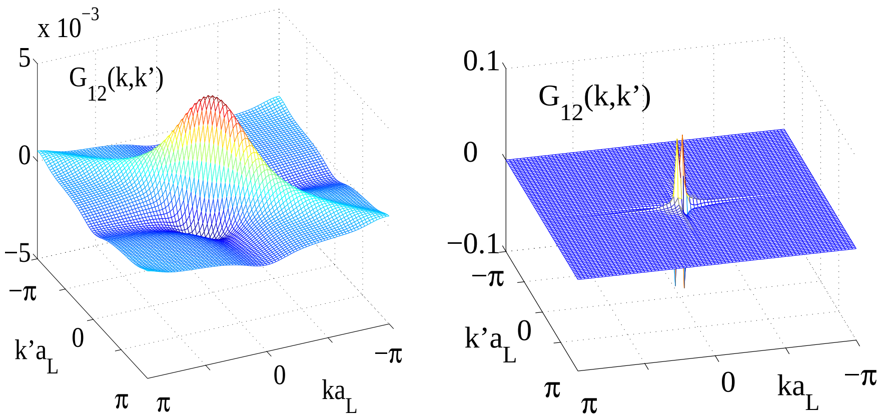

(a) MI (b) SF

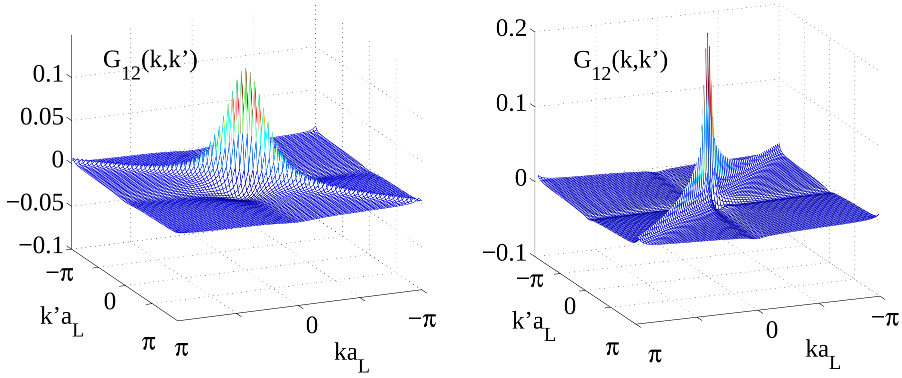

(c) PSF (d) CFSF

Figure 4.6: Noise correlations in the trapped system. The system size is 80 sites and $t/U = 0.02$. In (a), the system is in the SF state. The particle number of each species is 30, the trap frequency $8 \times 10^{-5}U$ and $U_{12}/U = 0.01$. In (b), the particle number of each species is 40, the trap frequency $1 \times 10^{-4}U$ and $U_{12}/U = -0.11$. The system has both MI and PSF orders. The MI state forms a plateau at unit-filling at the center of the trap and the PSF is formed at the edge. The PSF state at the edge causes the small peak along the $k = -k'$ direction, similar to the one in (c). However, this peak is at a much smaller amplitude than the one shown in (c), where the whole system is a PSF state. In (c), the particle number of each species is 20, the trap frequency $1 \times 10^{-5}U$ and $U_{12}/U = -0.11$. The whole system is in the PSF state. A strong pairing correlation is formed along $k = -k'$ direction. In (d), the particle number of each species is 30, the trap frequency is $8 \times 10^{-5}U$ and $U_{12}/U = 0.2$. The system has both CFSF and SF order. The CFSF order forms a plateau at half-filling at the center of the trap and the SF state towards the edges of the trap. The CFSF order causes a strong anti-pairing (particle-hole) correlation along $k = k'$direction. At the same time, the SF order adds to the "dips" along $k = 0$ and $k' = 0$.

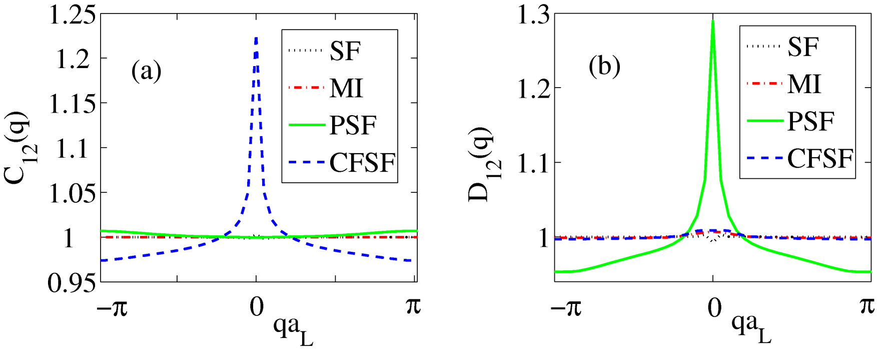

Figure 4.7: Correlations $C_{12}(q)$ and $D_{12}(q)$ for the states that are described in Fig. 4.7. In (a), we show the behavior of $C_{12}(q)$ (Eq. 4.2) in SF, MI, PSF and CFSF states. The strong anti-pairing (particle-hole) correlations in the CFSF state gives a strong signal around $q = 0$ in $C_{12}(q)$. This strong signal is also unique to the CFSF state and therefore can be used to detect to the CFSF order. In (b), we show the behavior of $D_{12}(q)$ (Eq. 4.3) in SF, MI, PSF and CFSF states. The strong pairing correlation in the PSF state is the reason for the high peak around $q = 0$ in $C_{12}(q)$. This suggests measuring $C_{12}(q)$ is a good way of detecting the PSF order.

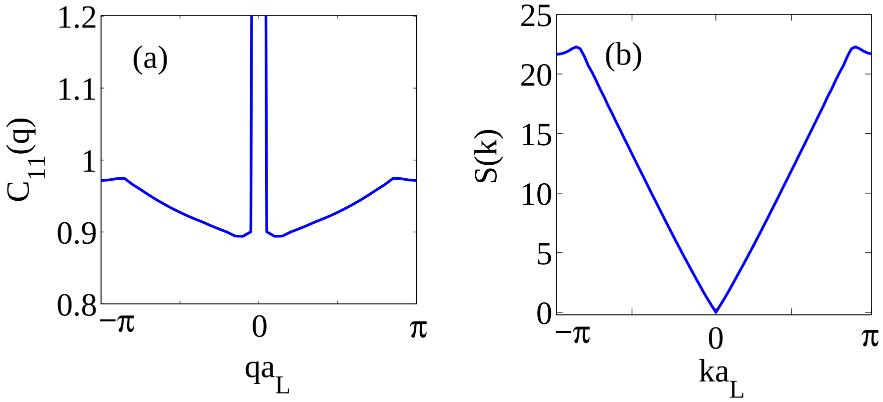

Figure 4.8: Noise correlation $C_{11}(q)$ and structure factor $S(k)$ in a PSF/CDW state. The system size is 80 sites and there are 20 particles of each species ($\nu = 0.25$). The trap frequency is $\Omega = 10^{-5}U$, the hopping $t = 0.02U$ and the inter-species interaction is $U_{12} = -0.11U$. The density at the center of the trap is roughly 0.45 per site and the cusps are developed around $\pm 0.9\pi$. The inhomogeneity of a trapped system means that the "Fermi wave vector" k_F is no longer $\pi\nu$, where ν is the average filling of the system. Instead, k_F can be evaluated as πn_{center}, where n_{center} is the density at the center of the trap,

we also calculate $C_{12}(q)$ (Eq. 4.2) and $D_{12}(q)$ (Eq. 4.3) for the four states. In the correlation $C_{12}(q)$ (Fig. 4.7 (a)), a high peak at $q = 0$ *only* appears in the case of the CFSF state. This peak corresponds to the peak in $\mathcal{G}_{12}$ along $k = k'$ in the CFSF state and is a reflection of the anti-pair correlation in the CFSF state. Similarly, in $D_{12}(q)$, the high peak at $q = 0$ *only* appears in the PSF state, as a result of the strong pairing correlations in the PSF state. A similar measurement has been performed for fermionic mixtures to detect the pairing of fermions [33].

In addition to the PSF and CFSF order, we also look for the signal of CDW order in $\mathcal{G}_{11}(k, k')$ in the trapped system. In a trapped system, the CDW order is more difficult to establish especially in the PSF and SF states, because the varying local density makes the "Fermi wave vector" πn a spatially varying quantity. However, we can still see weakened cusps forming at the momentum roughly corresponding to $2\pi n_{center}$, where n_{center} is the density at the center of the trap. This may indicate that in the trapped system, the CDW order in PSF and SF states has a wave vector corresponding to the density at the center of the trap. For the CFSF state, because the system has a plateau at half filling, the wave vector $2k_F$ is π/a_L. Compared to the homogeneous case, this feature is slightly diminished due to the effect of the coexisting SF state in the trapped system. In Fig. 4.8, we show one case where CDW order coexists with PSF order in a trap. The system size is 80 sites and there are 20 particles of each species. The trap frequency $\Omega = 10^{-5}U$, $t = 0.02U$ and $U_{12} = -0.11U$. The density at the center of the trap is roughly 0.45 per site. The cusps are developed around $\pm 0.9\pi$, which is roughly $2\pi n_{center}$.

4.3.3 Determination of Luttinger parameters from experimental data

Another important question is whether we can use the noise correlation $\mathcal{G}_{12}$ to measure the Luttinger parameters, K_S and K_A, in the PSF and CFSF regimes. The LL calculation shows that as the system size approaches infinity, the noise correlation $\mathcal{G}_{12}$ approaches a power law decay with the power $-1/K_S$ in the PSF regime and with $-1/K_A$ in the CFSF regime (see Eqs. 4.20 and 4.21). In our numerical results for $C_{12}(q)$ and $D_{12}(q)$, we indeed find that the decay from the peak at $q = 0$ satisfies the algebraic decay. To find out the power of the algebraic decay, we fit the function $C_{12}(q)$ in the PSF regime and $D_{12}(q)$ in the CFSF regime with the fitting function,

$$F(q) = A|\sin(2q)|^{-1/K} + B, \tag{4.26}$$

where B is the minimum value of $C_{12}(q)$ or $D_{12}(q)$ and A and K are the fitting parameters. In the PSF case ($U_{12}/U = -0.11$), we find that K is 1.3 ± 0.1. This is indeed very close to the value of K_S, which is estimated at 1.4 ± 0.1 obtained by the algebraic fit of R_S. In the CFSF case ($U_{12}/U = 0.2$), we find that K is roughly 1.48 ± 0.1, while the value of K_A extracted from the algebraic fit of R_A is also at 1.48 ± 0.12. Because of the singularity at $q = 0$, a reasonable values of K can be obtained by a simple algebraic decay function, $Aq^{-1/K}+B$, around small q. This shows that even in a trapped system, one can still assume a algebraical relationship predicted in the LL theory (Eqs. 4.20 and 4.21) and estimate the values of the Luttinger parameters by studying the power of the decay from the peak at $q = 0$.

4.4 Summary

What's most interesting in the behavior of the noise correlation is that it provides a *complete* set of signatures for all the phases that can possibly exist in the 1D binary Bose mixtures. These includes distinctive signatures for SF, MI, PSF, CFSF and CDW orders. In particular, we show the *direct* measurement of pairing order and the anti-pairing order through noise correlations, which can not be detected through the averaged time-of-flight density distribution. These features still can be observed even for a harmonically trapped system and we show that the modifications induced by the inhomogeneity understood in terms of the results for the homogeneous system. Even with the presence of a trap, the noise correlations in the PSF/CFSF regime still have distinctive peak structure that are being related with the Luttinger parameters, $K_S/\ K_A$. This suggests that one can use the noise correlation to estimate the Luttinger parameters in these two regimes.

Chapter 5

One dimensional binary Bose mixtures in optical lattices (III): transport properties

In [73], the transport property of an one-dimensional single-species Bose gas in a harmonic trap and a periodic potential is studied through the dipole oscillation of the center of mass of the atoms excited by suddenly displacing the total harmonic trap of the gas. Depending on the depth of the periodic potential, the dipole oscillation can change from undamped when the periodic potential is zero, to heavily damped when the periodic potential is relatively weak and the gas is in the strongly interacting superfluid (SF) state, and to overdamped when the periodic potential is strong. In [74, 75], the dipole oscillation of 1D Bose gas is studied numerically and have found good agreement with the experiment.

Here, we consider the transport properties for one-dimensional binary Bose mixtures. As studied in the two previous chapters, there are two additional phases in the mixtures: the paired superfluid and the counter-flow superfluid. In addition to their distinctive signals in the noise correlation (Chap. 4), we will show that the pairing (anti-pairing) mechanism in PSF (CFSF) states leads to very different transport properties. For the PSF state, because the particles are bounded as pairs, two species tend to behave the same way under perturbations, even when the kinetic energy injected into the two species are different. This is reflected as the suppression of the relative motion and the enhancement of the total motion of the particles. The opposite case can be found for the CFSF state, where because of the anti-pairing correlation, different species tend to avoid each other and move in exactly the opposite directions. The total motion in this state is strongly suppressed and the relative motion much enhanced.

It also important to notice that the pairing and anti-pairing ordering can exist in other systems as well. If we assume that each particle carries the same amount of charge and the two species are distinguished by up and down spins, the total (relative) motion discussed here corresponds to the charge (spin) mobility of the system. If we consider the case that the two species are distinguished by their location (like the case atoms localed on different lattice planes interacting through dipolar interactions [60]), the total (relative) motion here corresponds to the correlated (anti-correlated) motion between planes.

5.1 Dynamics after a trap displacement

5.1.1 Model and parameters

We consider two independently controllable traps for the two species and let Ω_a be the trapping frequency of species a and $j_{a,c}(t)$ are the location of the trap minimum, which we allow to be time dependent. This corresponds to a time-dependent term in the Hamiltonian (Eq. 3.1),

$$\sum_{j=1}^{N} \sum_{a=1,2} \Omega_a (j - j_{a,c}(t))^2 n_{a,j}. \tag{5.1}$$

Here, $n_{a,j}$ is the number operators and j is the lattice site with index j. For this calculation, we assume a system of 80 lattice sites and both traps are initially centered at the trap, $j_{a,c}(t=0) = 40.5$. The displacement is the location of the trap with regard to the center of the lattice,

$$D_a(t) = j_{a,c}(t) - j_{a,c}(0). \tag{5.2}$$

Both $D_a(t)$ and $j_{a,c}(t)$ are written in units of the lattice site. The parameter J is used to replace the hopping parameter t in the Hamiltonian of Eq. 3.1 to avoid the confusion with time t.

We consider four parameter sets as listed in Table 5.1. The sets correspond to the SF, PSF and CFSF states respectively. The hopping parameters are rather large in the PSF and CFSF region. This choice is made in order to exclude the influence of the CDW order that coexists with the PSF and CFSF order for smaller hoppings. The inter-species interactions are based on the phase diagram in Figs. 3.7 and 3.8. The particle number and the trap frequency of either species are chosen to make sure that the density at the center of the

	SF	PSF	CFSF
U_{12}/J	-0.1	-5.6	5.6
Ω_a/J	2×10^{-3}	2×10^{-4}	8×10^{-3}
N_a	20	20	21
N_a(Fig. 5.3)	10	10	21

Table 5.1: Parameters used to represent the SF, PSF and CFSF states. The hopping parameter is set at $U/J = 8$ for all cases. The particle number of each species is the same and denoted as N_a. stands for the particle number of either species.

trap can not be greater than 1 and the density is far from the edge of the lattice to minimize the boundary effects. The particle number and trap frequency chosen for the CFSF state also ensure that the density at the center can be higher than 0.5. We also consider one additional low density case for the PSF state in order to present the general feature of the PSF for all different fillings.

5.1.2 Simulation of the real time evolution

The initial state for the time evolution is the ground state of the system generated by the imaginary time propagation of the TEBD method. Details about the method can be found in Chap. 2. The trap is displaced at $t = 0$ and the real-time propagation with the TEBD method is used. Even although the Hamiltonian is time dependent, it is a close system and we can assume that for the propagation step from t to $t + \delta t$, where δt is sufficiently small, the Hamiltonian is time independent,

$$|\Psi(t + \delta t)\rangle = e^{-i\hbar H(t)\delta t}|\Psi(t)\rangle. \tag{5.3}$$

This real-time propagator is applied on to the state in the same way as the imaginary-time propagation (see Chap. 2 for details), except that the time step now is real. Similar to the imaginary-time propagation calculation, we use the second order Trotter-expansion to decompose the propagator for a small time step δt. Here, δt is set as $\delta t J/\hbar = 0.05$, where $\hbar$ is the Plank constant and is set to 1 in the simulation. The error introduced the expansion is estimated as $\sim O\left[(\delta t J/\hbar)^3\right] \sim 10^{-4}$. The real time propagator is a unitary transformation and the total number and total energy are constant during the propagation. Because of the Trotter-expansion, however, errors are introduced. We use the number conservation algorithm (explained in Chap. 2) in the propagation to ensure that the total number is conserved. The total energy is monitored during the propagation and we find it stays closely to a constant, with fluctuations on the order of the expansion error, throughout the whole propagation.

In addition to the total energy, several other observables, such as the density and correlations, are calculated along the propagation. In this chapter, we focus on the behavior of the density distribution $\langle n_{a,j}(t)\rangle$ as a function of time. To capture the collective behavior of each species, we calculated the center of mass for each species, defined as

$$x_{c,a}(t) \quad = \quad \sum_j \frac{j\langle n_{a,j}(t)\rangle}{N_a}. \tag{5.4}$$

At $t = 0$, both centers of mass are at the center of the trap, $x_{c,a}(t = 0) = 40.5$. After the displacement, the center of mass starts oscillating, which is a reflection of the collective response to the displacement of the corresponding species.

5.2 Result

In Chap. 3, we have discussed our numerical calculation of the density distributions in the SF, PSF and CFSF states in a trap (see Fig. 3.9). We have shown that both PSF and SF are compressible, while the CFSF state is incompressible. For a trapped system, the PSF order exists for the whole system. The CFSF state, however, exists only near the center of trap where a plateau at half-filling is formed and a SF state coexists with the CFSF state at the edge of the trap.

To probe the dynamical response of the PSF and CFSF state to an external perturbation, we consider two different type of the displacement. The first is a very brief displacement and the trap is brought back to the center. The second is a small displacement and the traps are placed in the new position for the rest of the time-evolution. Physically speaking, the brief displacement is like inject a small impulse and the constant displacement is like placing the system in a new potential configuration.

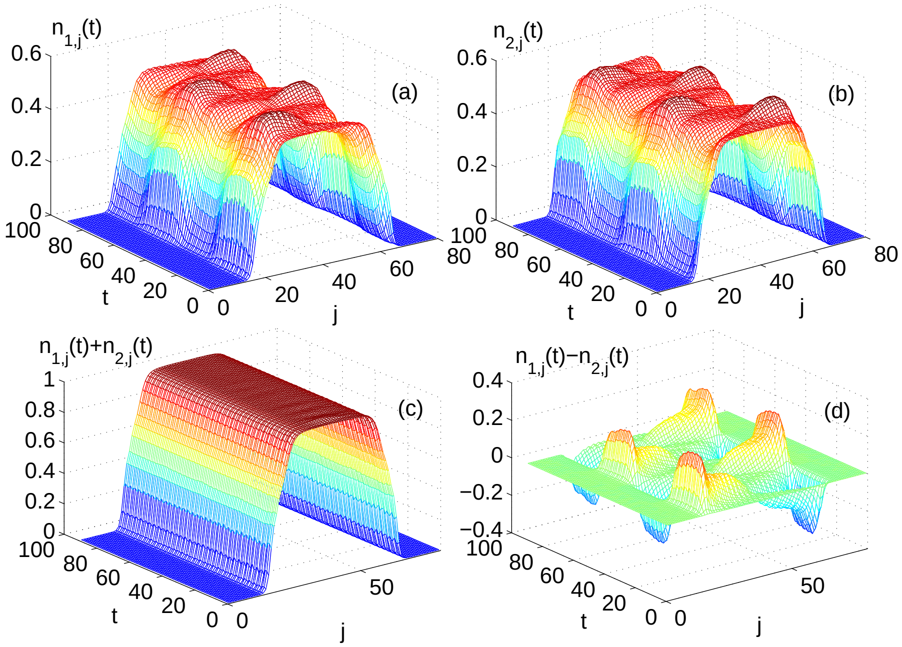

Figure 5.1: Dipole oscillation in the CFSF state. Note that time t is in the unit of $\hbar/J$ for all plots. At $t = 0$, the density distributions of both species have the same plateau at half-filling and then the trap of species 1 is briefly perturbed by a displacement of one lattice site [see Fig. 5.2 (a)]. In (a) and (b), we show the density distributions of species 1 and 2 as a function of time after the brief displacement. Species 1 and 2 have exactly opposite oscillation. In (c), we show the time evolution of the total density of both species. There is no oscillation in the total density and the plateau at the center is fixed at one. In (d), we show the time evolution of the relative density between the two species. The relative density reflects the oscillatory motion in species 1 and species 2.

5.2.1 Brief displacement

In this section, we would like to start the discussion with a compelling example for the *counter-flow* property in the CFSF phase (In Fig. 5.1). Here, *only* the trap of species 1 is displaced for a very brief time Δt (see Fig. 5.2(a)). The species 1 response to the displacement with oscillations that can be observed in its density distribution $\langle n_{1,j} \rangle$. Interestingly, atoms of species 2 instantaneously start to move in exactly the opposite way, even though their trap has not been displaced. What's more interesting is that the distribution of the total density in the CFSF state stays unchanged throughout [Fig. 5.1 (c)] and the oscillatory motion is completely captured in the relative motion [Fig. 5.1 (d)]. This mechanism of moving with fixed total density can be understood intuitively from the anti-pairing (or particle-hole) order. The particle-hole pairing requires that the local density of individual

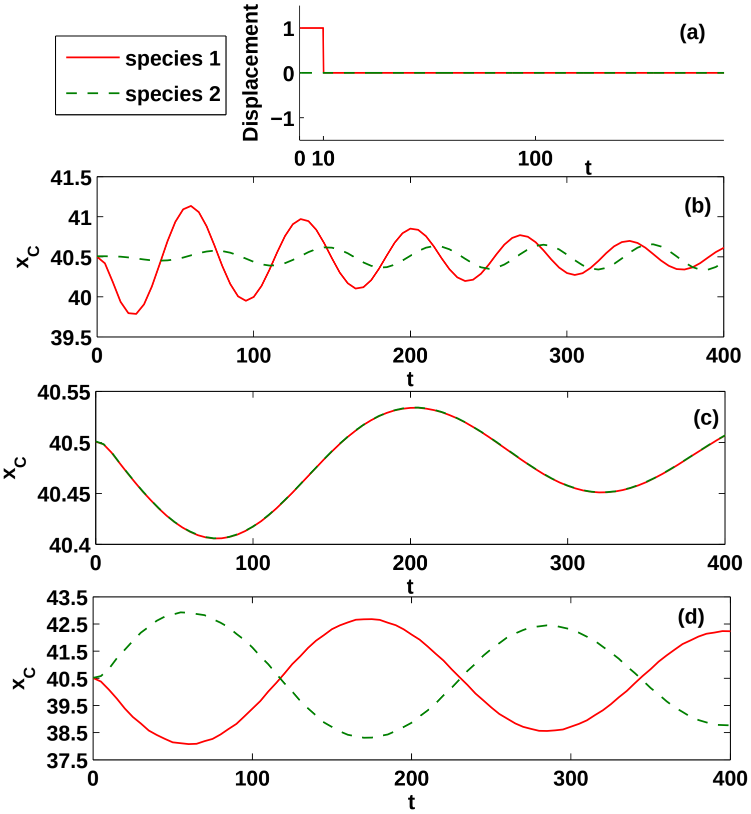

Figure 5.2: (a) Trap displacement as a function of time. Only the trap of species 1 is displaced at $t = 0$. The displacement is one lattice site and is removed at $t = 1J/\hbar$. (b)-(d) Dipole oscillation of the center of mass in SF, PSF and CFSF states induced by the displacement of species 1's trap. In the SF state (b), only species 1 are excited at $t = 0$ as a result of displacement. In PSF (c) and CFSF (d) states, both species are excited at $t = 0$ as a result of their pairing and anti-pairing order respectively. The red(green) color stands for species 1(2) for all plots in this chapter.

species satisfy $n_{j,1} = 1 - n_{j,2}$, where $1 - n_{j,2}$ represents the *density of the hole* of species 2 for at site j. This relationship does not restrict the behavior of the individual species, rather it puts a condition on the collective behavior of the two species.

Although the density distribution gives an intuitive picture of the oscillation, the amplitude of the oscillation can be too small to be visible in the density distribution. To study the oscillatory motion systemically, we consider the motion of the center of mass. In Fig. 5.2, we show the time-evolution of the center of mass for individual species in the SF, PSF and CFSF states. The trap displacement considered here is the same as the one in the previous paragraph. In Fig. 5.2 (b) we show the response of a SF state. Here, we see the excitation of only species 1 in the beginning. As a result of weakly attraction between the two species interact, the oscillatory motion of species 2 is induced gradually in a later time. In Fig. 5.2 (c), we show the response of the PSF state. In this case, due to the pairing order, both species start moving instantaneously and the time evolution of the two centers of mass are identical. The energy injected into species 1 is transformed into the total motion of both species. In Fig. 5.2 (d), we consider the CFSF case, the density distribution of which is discussed in the previous section. From the center of mass motion, we can clearly see that the oscillatory motion of species 1 is perfectly matched by an counter-flowing motion of species 2 and the total center of mass $x_{c,1}(t) + x_{c,2}(t)$ is kept almost constant.

From Fig. 5.2 c) and d) it is apparent that a characteristic feature of the transport in the CFSF (PSF) phase is that the total (relative) density oscillations are strongly suppressed. If we adopt a pseudo-spin language in which species 1 corresponds to spin-up and species 2 to spin-down, we can say that in the PSF state, the perturbation of the system leads to excitations in the charge sector of the system and in the CFSF state, the perturbation leads to excitation in the spin sector. If we apply the opposite type of impact for the two phases, i.e. total motion excitation for the CFSF state and relative motion excitation for the PSF state, the motion of the atoms will be entirely inhibited. To illustrate such effects, we consider displacing the traps in the same and opposite directions. The same displacements *only* excite the total motion. In this case, we expect only the PSF state be excited. For the opposite displacement, all energy is injected in the relative motion. Therefore only the CFSF state is excited. This is indeed what we find in our simulation. In Fig. 5.3, we show

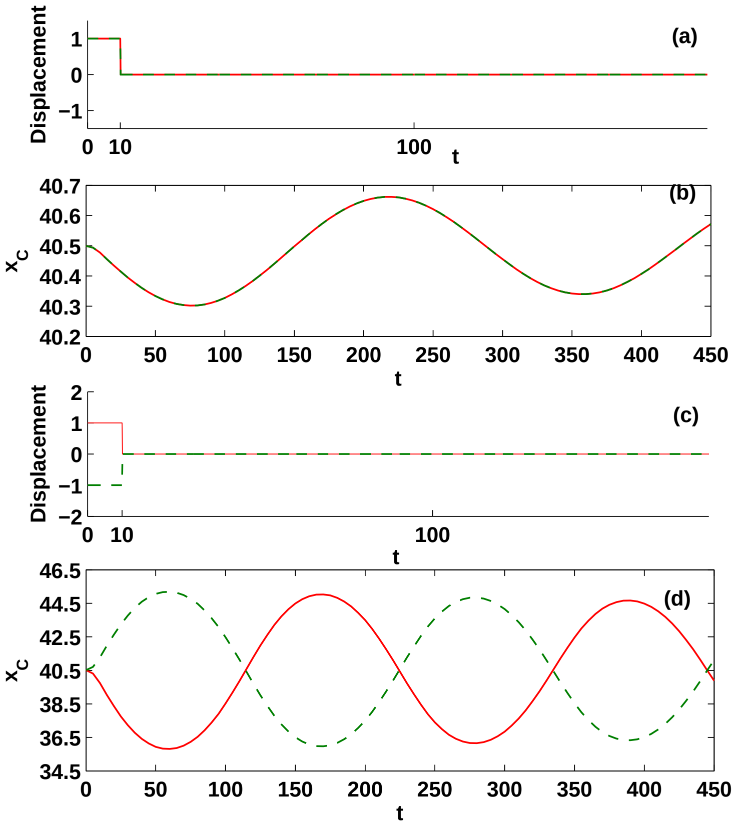

Figure 5.3: (a) Trap displacement as a function of time. Here, two traps are displaced by 1 lattice site at $t = 0$ and brought back to the original place at $t = J/\hbar$. (b) Dipole oscillation in the PSF state after the same displacement. (c) Trap displacement as a function of time. Here, two traps are displaced by ± 1 lattice site from the center and brought back to the center at $t = J/\hbar$. (d) Dipole oscillation of center of mass in the CFSF state after the opposite displacement. The parameters used are shown in Table. 5.1. Note that there is no dipole oscillation for the CFSF state under the same displacement and for the PSF state under the opposite trap displacement.

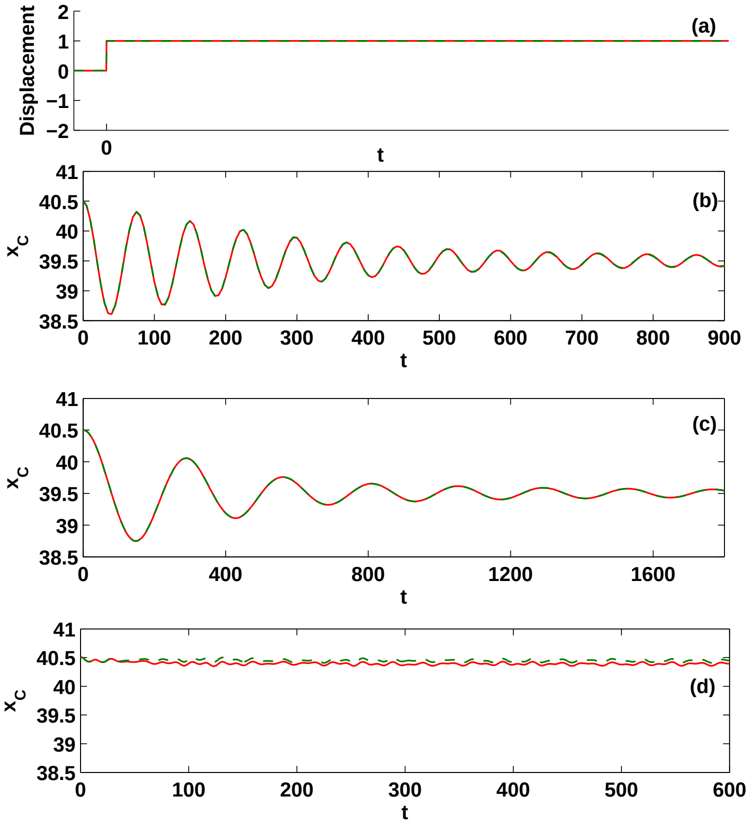

Figure 5.4: (a) Trap displacement as a function of time. Both traps are displaced by 1 lattice site at $t = 0$. In (b), the system is at SF state. Both species show the heavily damped dipole oscillation. In (c), the system at the PSF state and the two species show identical heavily damped dipole oscillations. In (d), the system is in a CFSF state. The dipole oscillation is overdamped in this case and the center of mass stays near the original equilibrium position before the displacement.

an example of the excitation of the total motion of the PSF state and the relative motion of the CFSF state under the same and opposite oscillation respectively. The inhibition of motion is also found in the constant displacement, which is discussed in the following section.

5.2.2 Constant displacement

Besides a brief, temporary displacement of the trap to impart an impulse on the atoms, we also consider displacing the trap permanently. To demonstrate the CFSF and PSF orders, we consider simultaneous displacements in the same and in opposite directions. In Fig.

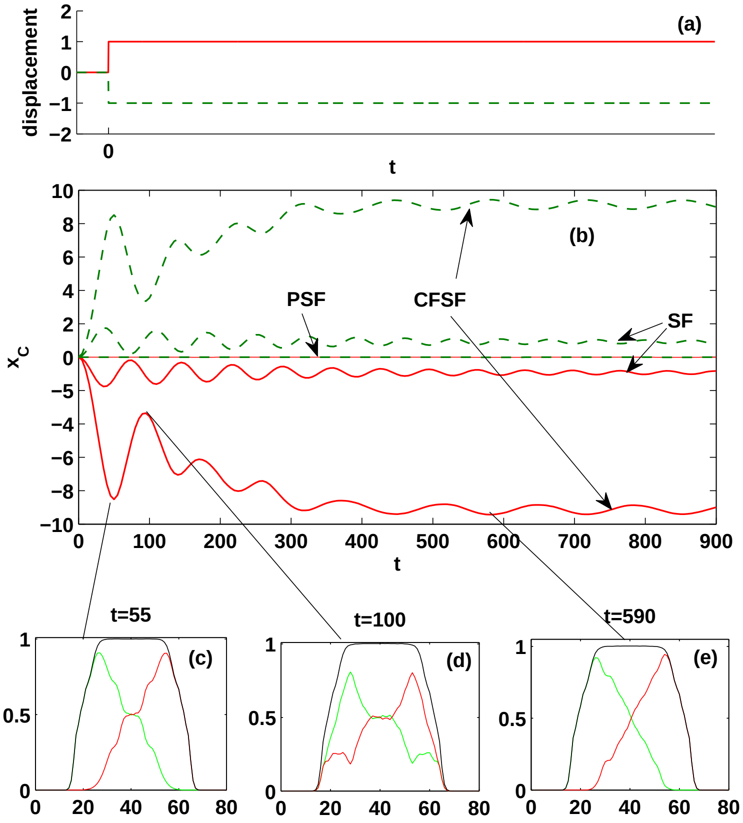

Figure 5.5: (a) Trap displacement as a function of time. The traps are displaced in the opposite direction by 1 lattice site at $t = 0$. (b) Dipole oscillation of the center of mass induced by the trap displacement. In this case, the PSF state prohibit the separation of the two species and the center of mass stays at the original equilibrium position of the trap before the displacement. For both CFSF and SF states, the center of mass of each species moves apart from each other under the displacement. In the SF case, the oscillation converges to the new equilibrium position of the traps after the displacement. But, in the CFSF case, each species keep moving away from each other, until they reach the edge of the CFSF state. In (c)-(e), we show the density distribution at different times for the CFSF state.

5.4 we consider the time-evolution under a constant displacement of the same amplitude. The response of three phases is markedly different. Both the SF and the PSF state exhibit oscillatory motion around the new minimum of the trap. However, the frequencies differ not only because of the different trapping frequencies but also because of the higher effective mass of the pairs in the PSF state. The motion of the CFSF state is almost entirely inhibited. The atoms stay essentially at the original location and the transport of the total density is suppressed. The small oscillations that are visible in the time evolution of $x_{c,1}(t)$ and $x_{c,2}(t)$ are due to oscillations of the superfluid fraction at the edges.

In Fig. 5.5 we consider displacing the traps in opposite directions. For the SF state, the two atomic species oscillate around the new trap minimum. The PSF state shows essentially no response, because the formed pairs are not broken up by the force imparted by the trap displacement. The most dramatic response is in the CFSF state. Here, the displacement of one lattice site leads to roughly ten-lattice-site relative displacement of the center of mass of each species. The small displacement in opposite directions is enhanced by the counter-propagating character of anti-pairing. To illustrate the response of the state further, we show density distributions of each of the two species as well as the total density. The total density distribution is again essentially fixed throughout the entire evolution. It is worth noting that the separation between the two species is limited by the size of the trap. It is reasonable to expect that the equilibrium position for the two species after the trap displacement will always be at the opposite edges of the CFSF plateau. If the one dimensional lattice is connected like a ring, this may lead to persistent counter-propagating flow.

5.3 Summary

The different responses of the PSF and CFSF states to a potential shift (Figs. 5.4 and 5.5), as well as to impulses (Fig. 5.2 and 5.3) vivid illustrate the defining features of the PSF and CFSF order, where the cross-species correlation leads to novel transport properties of the system. Under certain perturbations, the suppression of the individuality leads to similar transport properties as a Mott insulator state of a single-species system. However, for other perturbations, the PSF and CFSF states manifests their superfluid transport properties. Because such a selective excitation pattern is purely the result of pairing and anti-pairing ordering, it is reasonable to expect that very similar transport properties can be found for all the systems where the pairing (or anti-pairing) order is dominant. We therefore consider the transport properties based on the total/relative motion be generically true for PSF/CFSF order and is not limited for 1D binary Bose mixtures. Because the trap displacement can be easily controlled in the experiment, the transport properties predicted here should be realizable in the experiments once the PSF/CFSF order is present in the system. By increasing the displacement amplitude in the opposite way for the PSF state, it could potentially break pair ordering and therefore recover the individual oscillation. The displacement amplitude then becomes an indicator of the binding energy of the pairs. Similarly, large displacements in the same direction can break the anti-pairs in the CFSF state and provide information about the energy spectrum in the CFSF state.

Chapter 6

Two dimensional Bose-Fermi mixtures in optical lattices: pre-formed molecules and novel thermometry

6.1 Introduction

In Chaps. 3-5, we focus on discuss the new orders induced by the inter-species interaction in a mixture of bosonic atoms. Here, we would like to consider another different systems and the work discussed here is mostly motivated by the growing interests of ultra-cold polar molecules [76],

as they have the promise for being a new state of quantum degenerate matter, with unique properties. In order to have a large dipole moment, the polar molecules must be in their rovibrational ground state, where further cooling can ultimately lead to quantum degenerate dipolar matter [77]. Such polar molecules can have long-range, anisotropic or three-body interactions [78], which may lead to novel quantum phases [58, 80] and new applications in quantum information science [81]. In most ultra-cold polar molecule experiments, one starts with a mixture of ultra-cold gases of atoms of different species, for example various isotopic combinations of K and Rb [85, 84, 86, 83, 82]. These atoms can form a weakly bound state through a magnetic field sweep over the Feshbach resonance [87, 86]. To create molecules with significantly higher dipolar moments, the loosely bound Feshbach molecules are coherently transferred to a ground state with very high efficiency through stimulated Raman adiabatic passage (STIRAP) [88, 89, 90, 91].

Although the rate of transferring a Feshbach molecule to the ground state is very high, the overall efficiency for forming dipolar molecules is still low due to the low efficiency of forming the loosely bound Feshbach molecules during the field sweep. In Ref. [90], the fermionic ^{40}K and the bosonic^{87}Rb atoms are trapped by an optical trap. The efficiency to form the Feshbach molecule depends on the phase-space density of the two species. But, because the Fermi cloud stops shrinking once it reaches the quantum degenerate regime, and the Bose cloud continues to shrink as it Bose condenses, this phase space density is low at low temperature, and never reaches appreciable sizes at higher temperatures, as the clouds become more diffuse. On the other hand, if the mixture is first loaded onto an optical lattice, the motion of the atoms can be more strongly confined, and it is possible to create a large area where exactly one atom of each species sits at the same lattice site, leading to a reduced three body loss [87] and almost unit efficiency [92] for pre-forming the molecules.

When mixtures of ^{40}K and ^{87}Rb are loaded into an optical lattice, the atoms of each species are influenced by the optical lattice differently[**?**]. With the same optical lattice depth, the heavy atoms usually have much lower tunneling rate than the light atoms because of their significantly larger mass. In Ref. [92], it was shown that for sufficient lattice depths, the hopping rate of Rb is more than an order of magnitude less than that of K. It is therefore reasonable to ignore the quantum effects of the tunneling of the heavy bosonic atoms while allowing the light fermionic atoms to hop between nearest neighbors (a classical effect of the motion of the Rb atoms is taken into account by averaging over all energetically favorable distributions of Rb atoms). Such systems can be described by the Fermi-Bose Falicov-Kimball model [93, 94, 95]. Using this model, we quantitatively determine the probability of having exactly one atom of each species per lattice site in order to optimize the formation of dipolar molecules.

For the Falicov-Kimball model, the phenomena of pre-forming molecules has been discussed for Fermi-Fermi mixtures or Fermi-hard-core-Bose mixtures [96] on a homogeneous lattice and Fermi-Fermi mixtures in a harmonic trap [97]. In previous work [92], we considered the Fermi-soft-core-Bose mixtures in a harmonic trap and determined the efficiency for pre-forming molecules as the probability to have exactly one atom of each species per site. We used inhomogeneous dynamical mean-field theory (IDMFT) and Monte Carlo (MC) techniques to calculate the efficiency as well as the density profile and the entropy per particle. Both of these methods have advantages and disadvantages. The IDMFT approach is approximate for two-dimensional systems, but it can calculate both the efficiency and the entropy per particle. The MC method is numerically exact after it reaches thermal equilibrium, but it can not calculate the contributions to entropy coming from the heavy particles. Both methods require large computational times to calculate properties of a trapped system of reasonable size. Using these methods, we have shown that the efficiency is significantly increased by first loading onto an optical lattice before forming the molecules and near unit efficiency can be achieved with parameters that are realistic for current experiments.

The efficiency of pre-formed molecules is also likely to be affected by the heating (the temperature increase) induced by loading onto an optical lattice [1, 99, 98]. Considering that thermal fluctuations generally destroy the ordering and the localization of the particles, it is reasonable to expect that the efficiency of having exactly one Rb atom and one K atom per site should be reduced if the temperature becomes too high. On the other hand, if the temperature is low enough, the presence of the lattice significantly increases the efficiency, almost to unity in the case of deep lattices. The temperature of the lattice system, however, remains difficult to measure in experiment [104, 100, 102, 103, 101]. Instead, it is often assumed that the process of loading atoms onto optical lattices is adiabatic and therefore the total entropy of the system is conserved [98, 106, 1, 99, 105]. Determined based on the thermal properties of the gas before adding lattices, the *entropy per particle* is then used as an effective temperature scale for the lattice system [107, 1]. There are also several proposals for directly determining the temperature for systems of bosonic atoms [109, 108, 110], fermionic atoms [111] or the magnetic systems [112]. In Ref. [104], a general thermometry scheme is derived based on the fluctuation-dissipation theorem. Through quantum MC simulation, this proposal is shown to be applicable to the non-interacting fermionic systems [104] and interacting bosonic systems [113].

In our paper, we discuss light-Fermi-heavy-Bose mixtures in optical lattices based on the strong-coupling (SC) expansion method (perturbation theory in the hopping). The calculation is oriented to develop an efficient way of estimating the efficiency of pre-forming molecules for a given experimental system. With the SC expansion method, we obtain analytical expressions for the efficiency of pre-forming molecules, the entropy per particle and the local charge compressibilities. The behavior of the efficiency is studied both as a function of entropy per particle and temperature. The determination of temperature is further studied by applying the thermometry proposal in Ref. [104] to the Fermi-Bose mixture. To benchmark the accuracy, we compare the SC calculation with the IDMFT and MC calculations for all parameters considered. Overall, we find excellent agreement between the three methods. Such agreement even extends to the low temperature region when the interaction is strong enough. This is particularly useful, given the fact that the SC expansion calculation is significantly faster than the IDMFT and MC calculations. Such a speedup makes it possible to consider much larger lattice sizes to eliminate the boundary effects, to scan the large parameter space for optimal parameter regions for pre-formed molecules and to estimate the density fluctuations and other properties.

6.2 Fermi-Bose Falicov-Kimball model

For mixtures of heavy bosons and light fermions, such as ^{87}Rb/^{40}K mixtures, the hopping parameter for the heavy bosons (^{87}Rb) is usually more than an order of magnitude less than the hopping parameter for the light fermions (^{40}K) when one takes reasonable lattice depths (greater than 15 Rb recoil energies) [92]. In this case, we can ignore the quantum-mechanical effects of the hopping of the heavy bosons and describe such mixtures with the Fermi-Bose Falicov Kimball model in the presence of a trap potential. The Hamiltonian of this model is written as

$$H = H_0 + H_h = \sum_j H_{0j} + H_h, \tag{6.1}$$

with

$$\begin{aligned} H_{0j} &= (V_j - \mu_f) f_j^\dagger f_j + U_{bf} f_j^\dagger f_j b_j^\dagger b_j \\ &+ (V_j - \mu_b) b_j^\dagger b_j + \frac{1}{2} U_{bb} b_j^\dagger b_j (b_j^\dagger b_j - 1), \end{aligned} \tag{6.2}$$

and

$$H_h = -\sum_{jj'} t_{jj'} f_j^\dagger f_{j'}. \tag{6.3}$$

Here, j, j' label the sites of a two-dimensional square lattice, with a lattice constant, a. The symbols $f_j^\dagger$ and f_j denote the creation and annihilation operators for the fermions at lattice site j, respectively. The symbols $b_j^\dagger$ and b_j denote the creation and annihilation operators for the bosons at lattice site j, respectively. The fermionic operators satisfy the canonical anticommutation relation $\{f_j, f_{j'}^\dagger\} = \delta_{j,j'}$ and the bosonic operators satisfy the canonical commutation relation $[b_j, b_{j'}^\dagger] = \delta_{j,j'}$. The quantity V_j is the trap potential, which is assumed to be a simple harmonic-oscillator potential centered at the center of the finite lattice. We assume that the jth site has the coordinate (x_j, y_j), so that V_j can be written as

$$V_j = t\left[\frac{\hbar\Omega}{2ta}\right]^2\left(x_j^2 + y_j^2\right), \tag{6.4}$$

where Ω is the trap frequency. The quantity μ_f is the chemical potential for fermions and μ_b is the chemical potential for bosons. Combining the trap potential and the chemical potentials, we can define an effective position dependent local chemical potential for the fermions, $\mu_{f,j} = \mu_f - V_j$, and for the bosons, $\mu_{b,j} = \mu_b - V_j$. U_{bf} is the interaction energy between fermions and bosons and U_{bb} is the interaction energy between the soft-core bosons. The symbol $-t_{jj'}$ is the hopping energy for fermions to hop from site j' to site j. We consider a general $t_{jj'}$ for the formal developments in the earlier part of the next section, but later specialize to the case of nearest-neighbor hopping with amplitude t, which we will take to be the energy unit. We also set the lattice constant, a equal to one.

The efficiency for pre-forming molecules is defined as the averaged joint probability of having exactly one boson and exactly one fermion on a lattice site,

$$\mathcal{E} = \frac{1}{N}\sum_j \langle \hat{P}_{1,1}^j \rangle = \frac{1}{N}\sum_j \mathrm{Tr}\left(\hat{P}_{1,1}^j e^{-\beta H}\right), \tag{6.5}$$

with $\beta = (k_B T)^{-1}$ the inverse temperature. We define the projection operator $\hat{P}_{1,1}^j$ for having exactly one boson and one fermion at site j,

$$\hat{P}_{1,1}^j = |n_{b,j} = 1, n_{f,j} = 1\rangle\langle n_{b,j} = 1, n_{f,j} = 1|, \tag{6.6}$$

and N is the smaller value in the total numbers of bosons and fermions, N_b and N_f. In our case, we assume equal number of bosons and fermions, therefore $N = N_b = N_f$.

In general, one can obtain $\mathcal{E}$ directly from Eq. (6.5) for a readily diagonalized Hamiltonian. In our case, the efficiency $\mathcal{E}$ is derived by distinguishing the contribution from terms corresponding to $n_{b,j} = 1$ in the expression for the density of fermions. We assume that the density of bosons and fermions at site j, $\rho_{b,j}$ and $\rho_{f,j}$, can be both be written as a series in terms of the occupation number of bosons at site j in the following way,

$$\rho_{b,j} = \langle b_j^\dagger b_j \rangle = \sum_{n_{b,j}} \mathcal{W}_j(n_{b,j}) n_{b,j}, \tag{6.7}$$

and

$$\rho_{f,j} = \langle f_j^\dagger f_j \rangle = \sum_{n_{b,j}} \mathcal{W}_j(n_{b,j}) \widetilde{n}_{f,j}(n_{b,j}). \tag{6.8}$$

Here $n_{b,j}$ is the occupation number of bosons on site j, $n_{b,j} = 0, 1, ...$ The coefficient $\mathcal{W}_j(n_{b,j})$ is the *probability* of having exactly $n_{b,j}$ bosons at site j and the coefficient $\widetilde{n}_{f,j}(n_{b,j})$ is the probability for having one fermion on site j for the occupation number $n_{b,j}$. The joint probability of having exactly one boson and one fermion at site j can be written as

$$\mathcal{E}_j = \mathcal{W}_j(n_{b,j} = 1) \widetilde{n}_{f,j}(n_{b,j} = 1), \tag{6.9}$$

and the efficiency $\mathcal{E}$ is the average of $\mathcal{E}_j$ over all sites,

$$\mathcal{E} = \frac{\sum_j \mathcal{E}_j}{N} = \frac{\sum_j \mathcal{W}_j(n_{b,j} = 1) \widetilde{n}_{f,j}(n_{b,j} = 1)}{N}. \tag{6.10}$$

It can be shown that the expression for the efficiency obtained in this way is the same as from Eq. (6.5). Now, the efficiency is obtained directly from the density of bosons and fermions, which can be easily derived from the partition function $\mathcal{Z}$ by taking derivatives with respect to the appropriate chemical potentials,

$$\rho_{b,j} = \frac{1}{\beta}\frac{\partial \ln(\mathcal{Z})}{\partial \mu_{b,j}}, \tag{6.11}$$

and

$$\rho_{f,j} = \frac{1}{\beta}\frac{\partial \ln(\mathcal{Z})}{\partial \mu_{f,j}}. \tag{6.12}$$

To study the behavior of the efficiency as a function of the entropy per particle, we evaluate the entropy per particle by dividing the total entropy by the total number of particles,

$$\begin{aligned} s &= S/(N_b + N_f) \\ &= \left(k_B \ln(\mathcal{Z}) - \beta k_B \frac{\partial \ln(\mathcal{Z})}{\partial \beta}\right)/(N_b + N_f). \end{aligned} \tag{6.13}$$

It is worthwhile noticing that the formalism development in this section is based on the grand-canonical ensemble. This ensemble is appropriate because we assume that in the lattice system both the energy and the number of particles fluctuate. This may seem in contradiction with the use of the entropy per particle as an effective temperature scale, because strictly speaking entropy is used as a parameter only for the micro-canonical ensemble. This contradiction is resolved because the entropy per particle is assumed to be conserved *during* the process of turning on the optical lattice. It is a conserved quantity when comparing the systems before and after turning on the optical lattice, which is particularly useful from the experimental point of view, since the experiments often start without the optical lattices. For the lattice system itself, assuming it is in thermal equilibrium, it is more reasonable to consider it with the grand-canonical ensemble, allowing the energy and number fluctuations. The difference between the different ensembles of course is not problematic if we assume the system is large enough to be in the thermodynamical limit, where all three ensembles are equivalent.

6.3 Strong coupling expansion formalism

In this section, we explain the SC expansion formalism. We first discuss the evaluation of the partition function $\mathcal{Z}$, approximated by the second-order expansion in terms of the hopping, H_h. From the partition function, we derive the expressions for the density of fermions shown in Eqs. (6.32) to (6.34), the density of bosons in Eqs. (6.35) to (6.37), the efficiency in Eqs. (6.38) to (6.40) and the entropy per particle in Eqs. (6.44) to (6.47). For readers who prefer to see the final expressions, we suggest skipping the following derivation and referring to the equations listed above for the corresponding quantities.

The evaluation of the partition function in the SC approach starts with the exact solution of the atomic Hamiltonian H_0. Hence, we use an interaction picture with respect to H_0, where for any operator $\mathcal{A}$, we define the (imaginary) time-dependent operator $\mathcal{A}(\tau) = e^{\tau H_0}\mathcal{A}e^{-\tau H_0}$. The partition function is written using the standard relation,

$$\mathcal{Z} = \mathrm{Tr}\left(e^{-\beta H}\right) = \mathrm{Tr}\left(e^{-\beta H_0}\mathcal{U}(\beta,0)\right). \tag{6.14}$$

Here, $\mathcal{U}(\beta,0) = \mathcal{T}_\tau \exp\left[\int_0^\beta H_h(\tau)d\tau\right]$ is the evolution operator with $\mathcal{T}_\tau$ being the time-ordering operator for imaginary times. Expanding the exponential in $\mathcal{U}(\beta,0)$ up to second order in $H_h(\tau)$ and evaluating the resulting traces with respect to equilibrium ensembles of H_0, we have

$$\begin{aligned} \mathcal{U}(\beta,0) &\simeq 1 + \\ &+ \frac{1}{2}\int_0^\beta d\tau_1 \int_0^\beta d\tau_2 \mathcal{T}_\tau H_h(\tau_1)H_h(\tau_2). \end{aligned} \tag{6.15}$$

Here, we note that the first order correction to the partition function vanishes because the hopping connects different sites. Substituting Eq. (6.15) into Eq. (6.14), we can write the partition function as,

$$\mathcal{Z} = \mathcal{Z}^{(0)}(1 + \mathcal{Z}^{(2)}), \tag{6.16}$$

where $\mathcal{Z}^{(0)}$ is the partition function in the atomic limit ($t = 0$),

$$\mathcal{Z}^{(0)} = \mathrm{Tr}\left(e^{-\beta H_0}\right), \tag{6.17}$$

and $\mathcal{Z}^{(2)}$ corresponds to the second-order term in the expansion of $\mathcal{U}$ divided by $\mathcal{Z}^{(0)}$,

$$\mathcal{Z}^{(2)} = \frac{1}{2\mathcal{Z}^{(0)}}\mathrm{Tr}\left[e^{-\beta H_0}\int_0^\beta\int_0^\beta d\tau_1 d\tau_2 \mathcal{T}_\tau H_h(\tau_1)H_h(\tau_2)\right]. \tag{6.18}$$

To simplify the notation, we introduce $\bar{\mu}_{f,j}(n_{b,j})$ to represent the negative of the fermionic part of the Hamiltonian H_{0j} [Eq. (6.2)] when there is a fermion at site j,

$$\bar{\mu}_{f,j}(n_{b,j}) \equiv \mu_f - V_j - U_{bf}n_{b,j}, \tag{6.19}$$

and $\bar{\mu}_{b,j}(n_{b,j})$ for the negative of the bosonic part of the Hamiltonian H_{0j},

$$\bar{\mu}_{b,j}(n_{b,j}) \equiv (\mu_b - V_j)n_{b,j} - U_{bb}n_{b,j}(n_{b,j} - 1)/2. \tag{6.20}$$

Both $\bar{\mu}_{f,j}$ and $\bar{\mu}_{b,j}$ depend on the number of bosons at site j. The effective fugacities for bosonic and fermionic particles can then be written as the exponential of $\bar{\mu}_{f,j}$ and $\bar{\mu}_{b,j}$ respectively,

$$\phi_{f,j}(n_b) = \exp\left[\beta\bar{\mu}_{f,j}(n_{b,j})\right], \tag{6.21}$$

and

$$\phi_{b,j}(n_b) = \exp\left[\beta\bar{\mu}_{b,j}(n_{b,j})\right]. \tag{6.22}$$

The atomic partition function $\mathcal{Z}^{(0)}$ can then be written in terms of the effective fugacities as,

$$\mathcal{Z}^{(0)} \quad = \quad \Pi_j \mathcal{Z}_j^{(0)}, \tag{6.23}$$

where $\mathcal{Z}_j^{(0)}$ is the atomic partition function at site j,

$$\mathcal{Z}_j^{(0)} = \sum_{n_{b,j}} \phi_{b,j}(n_{b,j})(1 + \phi_{f,j}(n_{b,j})). \tag{6.24}$$

Now we evaluate the second term in the partition function, $\mathcal{Z}^{(2)}$ of Eq. (6.31). To satisfy the total number conservation, only terms with $j = k'$ and $j' = k$ in $H_h(\tau_1)H_h(\tau_2)$ are nonzero after the trace and $\mathcal{Z}^{(2)}$ is reduced into a sum of products of the fermionic annihilation and creation operators at the same site,

$$\begin{aligned}
\mathcal{Z}^{(2)} &= \frac{1}{2}\int_0^\beta \int_0^\beta d\tau_1 d\tau_2 \sum_{jk} t_{jk} t_{kj} \\
&\quad \times \mathrm{Tr}\left[\mathcal{T}_\tau e^{-\beta H_{0j}} f_j^\dagger(\tau_1) f_j(\tau_2)\right] / \mathcal{Z}_j^{(0)} \\
&\quad \times \mathrm{Tr}\left[\mathcal{T}_\tau e^{-\beta H_{0k}} f_k(\tau_1) f_k^\dagger(\tau_2)\right] / \mathcal{Z}_k^{(0)}.
\end{aligned} \tag{6.25}$$

Using the cyclic permutation relationship of the trace, the products can be represented by the local atomic Green's function,

$$G_{jj}(\tau) = -\mathrm{Tr}\left[\mathcal{T}_\tau e^{-\beta H_{0j}} f_j(\tau) f_j^\dagger(0)\right] / \mathcal{Z}_j^{(0)}, \tag{6.26}$$

and $\mathcal{Z}^{(2)}$ is expressed as integrations of the atomic Green's functions in terms of their relative times,

$$\mathcal{Z}^{(2)} = -\frac{1}{2}\int_0^\beta \int_0^\beta d\tau_1 d\tau_2 \sum_{jk} t_{jk} t_{kj} G_{kk}(\tau_1 - \tau_2) G_{jj}(\tau_2 - \tau_1). \tag{6.27}$$

Solving the Heisenberg equation of motion for the annihilation operator $f_j(\tau)$,

$$\frac{\partial f_j(\tau)}{\partial \tau} = e^{H_0 \tau} \left[H_0, f_j\right] e^{-H_0 \tau} \tag{6.28}$$

one easily finds the expression for the annihilation operator $f_j(\tau)$ in the interaction picture,

$$f_j(\tau) = e^{\bar{\mu}_{f,j}(n_{b,j})\tau} f_j(0), \tag{6.29}$$

Substituting Eq. (6.29) into Eq. (6.26), we obtain the atomic Green's function in terms of the effective fugacities as,

$$G_{jj}(\tau) = \begin{cases} -\sum_{n_b} \frac{\phi_{b,j}(n_b)}{\mathcal{Z}_j^{(0)}} e^{\tau \bar{\mu}_{f,j}}, & \tau > 0 \\ \sum_{n_b} \frac{\phi_{b,j}(n_b)\phi_{f,j}(n_b)}{\mathcal{Z}_j^{(0)}} e^{\tau \bar{\mu}_{f,j}}, & \tau < 0 \end{cases} \tag{6.30}$$

We now perform the integration over τ_1 and τ_2 in $\mathcal{Z}^{(2)}$ and obtain the final expression for $\mathcal{Z}^{(2)}$,

$$\mathcal{Z}^{(2)} = \frac{1}{2} \sum_{jk} t_{jk} t_{kj} \sum_{n_{b,j} n_{b,k}} \frac{\phi_{b,j}(n_{b,j})\phi_{b,k}(n_{b,k})}{\mathcal{Z}_j^{(0)} \mathcal{Z}_k^{(0)}} \frac{\beta(\phi_{f,j}(n_{b,j}) - \phi_{f,k}(n_{b,k}))}{\bar{\mu}_{f,j}(n_{b,j}) - \bar{\mu}_{f,k}(n_{b,j})}. \tag{6.31}$$

Note that the partition function we derived here is not limited to the case of nearest-neighbor hopping with a uniform hopping parameter t. Eq. (6.31) can be applied to describe hopping between arbitrary sites j and k and the hopping parameter t_{jk} can vary over different sites of the lattice.

Observables are evaluated by taking appropriate derivatives of the partition function. In calculating the derivatives, we truncate all final expressions to include only terms through the order of t_{jk}^2. Also note that because sites j and k are different sites, we do not normally have denominators equal to zero in Eq. (6.31), but in any case, the formulas are always finite as can be verified by l'Hôpital's rule. During numerical calculations of the observables, the denominator, $\bar{\mu}_{f,j}(n_{b,j}) - \bar{\mu}_{f,k}(n_{b,j})$, can become too small and cause numerical errors. In our calculations, we use the Taylor expansion in terms of $\bar{\mu}_{f,j}(n_{b,j}) - \bar{\mu}_{f,k}(n_{b,j})$ around zero when the absolute value of $\bar{\mu}_{f,j}(n_{b,j}) - \bar{\mu}_{f,k}(n_{b,j})$ is less than 10^{-5}.

The density distribution is evaluated by taking the derivative of the partition function with respect to the appropriate local chemical potential [Eqs. (6.12) and (6.11)]. For the density of fermions at site j, the expression constitutes two terms corresponding to derivatives from $\mathcal{Z}^{(0)}$ and $\mathcal{Z}^{(2)}$,

$$\rho_{f,j} = \frac{1}{\beta} \frac{\partial \text{In}(\mathcal{Z})}{\partial \mu_{f,j}} = \rho_{f,j}^{(0)} + \rho_{f,j}^{(2)}, \tag{6.32}$$

where $\rho^{(0)}_{f,j}$ is the density of fermions in the atomic limit,

$$\rho^{(0)}_{f,j} = \frac{1}{\beta}\frac{\partial \mathrm{In}\left(\mathcal{Z}^{(0)}_{j}\right)}{\partial \mu_f} = \frac{\sum_{n_{b,j}} \phi_{f,j}(n_{b,j})\phi_{b,j}(n_{b,j})}{\mathcal{Z}^{(0)}_{j}}, \tag{6.33}$$

and $\rho^{(2)}_{f,j}$ is the total contribution to the density at site j from particles hopping from all possible sites,

$$\begin{aligned} \rho^{(2)}_{f,j} &= \sum_k t_{jk}t_{kj} \sum_{n_{b,j}n_{b,k}} \left\{ \frac{\phi_{b,j}(n_{b,j})\phi_{b,k}(n_{b,k})}{\mathcal{Z}^{(0)}_{j}\mathcal{Z}^{(0)}_{k}} \right. \\ &\times \left[\beta \frac{(1-\rho^{(0)}_{j,k})\phi_{f,j}(n_{b,j}) + \rho^{(0)}_{j,k}\phi_{f,k}(n_{b,k})}{\bar{\mu}_{f,j}(n_{b,j}) - \bar{\mu}_{f,k}(n_{b,j})} \right. \\ &+ \left. \left. \frac{\phi_{f,k}(n_{b,j}) - \phi_{f,j}(n_{b,k})}{[\bar{\mu}_{f,j}(n_{b,j}) - \bar{\mu}_{f,k}(n_{b,j})]^2} \right] \right\}. \end{aligned} \tag{6.34}$$

Similarly, the density of bosons at site j is written as a sum of the atomic density and the hopping contribution as,

$$\rho_{b,j} = \frac{1}{\beta}\frac{\partial \ln(\mathcal{Z})}{\partial \mu_{b,j}} = \rho^{(0)}_{b,j} + \rho^{(2)}_{b,j}, \tag{6.35}$$

where

$$\rho^{(0)}_{b,j} = \frac{1}{\beta}\frac{\partial \mathrm{In}\left(\mathcal{Z}^{(0)}_{\mathrm{j}}\right)}{\partial \mu_{b,j}} = \frac{\sum_{n_{b,j}} n_{b,j}\phi_{b,j}(n_{b,j})\left[1 + \phi_{f,j}(n_{b,j})\right]}{\mathcal{Z}^{(0)}_{j}}, \tag{6.36}$$

and

$$\begin{aligned} \rho^{(2)}_{b,j} &= \sum_k t_{jk}t_{kj} \sum_{n_{b,j}n_{b,k}} \left[(n_{b,j} - \rho^{(0)}_{b,j}) \frac{\phi_{b,j}(n_{b,j})\phi_{b,k}(n_{b,k})}{\mathcal{Z}^{(0)}_{j}\mathcal{Z}^{(0)}_{k}} \right. \\ &\times \left. \frac{\beta[\phi_{f,j}(n_{b,j}) - \phi_{f,k}(n_{b,k})]}{\bar{\mu}_{f,j}(n_{b,j}) - \bar{\mu}_{f,k}(n_{b,j})} \right]. \end{aligned} \tag{6.37}$$

The expression for the efficiency is obtained from the density distributions of the fermions and bosons. Similar to the expression for the densities, the efficiency consists of two terms, one corresponding to the atomic limit and one corresponding to the contributions from the hopping,

$$\mathcal{E}_j = \mathcal{E}_j^{(0)} + \mathcal{E}_j^{(2)}, \tag{6.38}$$

where

$$\mathcal{E}_j^{(0)} = \frac{\phi_{b,j}(n_{b,j})\phi_{f,j}(n_{b,j})|_{n_{b,j}=1}}{\mathcal{Z}_j^{(0)}}, \tag{6.39}$$

and

$$\begin{aligned}
\mathcal{E}_j^{(2)} \;=\; & \sum_k \sum_{n_{b,j},n_{b,k}} \frac{\phi_{b,j}(n_{b,j})\phi_{b,k}(n_{b,k})}{\mathcal{Z}_j^{(0)}\mathcal{Z}_k^{(0)}} \times \\
& \left\{ - \left(\frac{\phi_{b,j}(n'_{b,j})\phi_{f,j}(n'_{b,j})}{\mathcal{Z}_j^{(0)}} \right)_{n'_{b,j}=1} \right. \\
& \times \frac{\beta \left[\phi_{f,j}(n_{b,j}) - \phi_{f,k}(n_{b,k})\right]}{\bar{\mu}_{f,j}(n_{b,j}) - \bar{\mu}_{f,k}(n_{b,j})} \\
& + \delta_{n_{b,j},1} \left[\beta \frac{\phi_{f,j}(n_{b,j})}{\bar{\mu}_{f,j}(n_{b,j}) - \bar{\mu}_{f,k}(n_{b,j})} \right. \\
& \left. \left. + \frac{\phi_{f,k}(n_{b,j}) - \phi_{f,j}(n_{b,k})}{\left[\bar{\mu}_{f,j}(n_{b,j}) - \bar{\mu}_{f,k}(n_{b,j})\right]^2} \right] \right\}.
\end{aligned} \tag{6.40}$$

For the trapped system, the local chemical potential μ_j includes both the global chemical potential μ and the trapping potential V_j. The derivatives with regard to the local chemical potential or the chemical potential leads to different physical quantities. For the Fermi-Bose mixture considered here, the cross-derivatives should also be evaluated. Specifically, the derivative with regard to the global chemical potential $(\mu_b + \mu_f)$ corresponds to the total number fluctuations,

$$\begin{aligned}
\kappa &= \frac{\partial^2 \ln \mathcal{Z}}{\partial^2(\mu_b + \mu_f)} \\
&= \beta\langle \left(\hat{N}_f + \hat{N}_b\right)^2 \rangle - \langle \hat{N}_f + \hat{N}_b \rangle^2.
\end{aligned} \tag{6.41}$$

Here we define the total number operators, $\hat{N}_f = \sum_j f_j^\dagger f_j$ and $\hat{N}_b = \sum_j b_j^\dagger b_j$. The *global* compressibility is introduced as the response of the local density to the change of the global chemical potentials,

$$\begin{aligned}\kappa_j^g &= \frac{\partial^2 \ln \mathcal{Z}}{\partial(\mu_{f,j}+\mu_{b,j})\partial(\mu_b+\mu_f)} \\ &= \beta\left[\langle\left(f_j^\dagger f_j + b_j^\dagger b_j\right)\left(\hat{N}_f+\hat{N}_b\right)\rangle\right. \\ &\quad \left.-\langle f_j^\dagger f_j + b_j^\dagger b_j\rangle\langle\hat{N}_f+\hat{N}_b\rangle\right]. \qquad (6.42)\end{aligned}$$

And the *local* compressibility, or the onsite number fluctuation, is determined from the derivatives with regard to the local chemical potential,

$$\begin{aligned}\kappa_j^l &= \frac{\partial^2 \ln \mathcal{Z}}{\partial^2(\mu_{b,j}+\mu_{f,j})} \\ &= \beta\left[\langle\left(f_j^\dagger f_j + b_j^\dagger b_j\right)^2\rangle - \langle f_j^\dagger f_j + b_j^\dagger b_j\rangle^2\right]. \qquad (6.43)\end{aligned}$$

Both the global and local compressibilities are derivatives of the density distributions and can be obtained from the density expressions above.

Finally, we obtain the expression for the entropy per particle defined in Eq. (6.13) by averaging the total entropy of the system and we again write the entropy per particle in terms of the atomic limit expression and the contributions from the hopping,

$$s = \frac{1}{N}\sum_j S_j^{(0)} + \frac{1}{N}\sum_j S_j^{(2)}. \qquad (6.44)$$

Here $S_j^{(0)}$ is the entropy at site j in the atomic limit,

$$S_j^{(0)}/k_B = \ln\left(\mathcal{Z}_j^{(0)}\right) - \beta\epsilon_j, \qquad (6.45)$$

where the parameter ϵ_j corresponds to the onsite energy at site j in the atomic limit,

$$\begin{aligned}\epsilon_j &= \frac{\partial \ln(\mathcal{Z}^{(0)})}{\partial\beta} \\ &= \frac{1}{\mathcal{Z}_j^{(0)}}\sum_{n_{b,j}}\{\bar{\mu}_{b,j}(n_{b,j})\phi_{b,j}(n_{b,j})\left[1+\phi_{f,j}(n_{b,j})\right]\end{aligned}$$

$$+ \bar{\mu}_{f,j}(n_{b,j})\phi_{b,j}(n_{b,j})\phi_{f,j}(n_{b,j})\} \, . \tag{6.46}$$

The averaged contributions from the hopping at site j is $S_j^{(2)}$,

$$\begin{aligned} S_j^{(2)}/k_B &= \ln(1+\mathcal{Z}^{(2)}) - \beta \frac{\partial \ln(1+\mathcal{Z}^{(2)})}{\partial \beta} \\ &= -\frac{\beta^2}{2}\sum_k \sum_{n_{b,j}n_{b,k}} \frac{\phi_{b,j}(n_{b,j})\phi_{b,k}(n_{b,k})}{\mathcal{Z}_j^{(0)}\mathcal{Z}_k^{(0)}\left[\bar{\mu}_{f,j}(n_{b,j}) - \bar{\mu}_{f,k}(n_{b,j})\right]} \\ &\quad \times \{[\phi_{f,j}(n_{b,j}) - \phi_{f,k}(n_{b,k})] \\ &\quad \times [\bar{\mu}_{b,j}(n_{b,j}) + \bar{\mu}_{b,k}(n_{b,k}) - \epsilon_j - \epsilon_k] \\ &\quad + \bar{\mu}_{f,j}(n_{b,j})\phi_{f,j}(n_{b,j}) - \bar{\mu}_{f,k}(n_{b,k})\phi_{f,k}(n_{b,j})\} \, . \end{aligned} \tag{6.47}$$

This ends the discussion on the derivation of the SC expansion method formulas. In general, the expressions obtained above are accurate in the case when the hopping is much smaller than interaction strength and the temperature is very high (βt is small). In this parameter region, the SC method can evaluate physical quantities, like the density distribution, efficiency, compressibility and entropy, very efficiently. The total number of particles is fixed by varying the chemical potentials, μ_b and μ_f. To maximize the efficiency and reduce three body loss, we consider the low density region with attractive interspecies interactions and repulsive bosonic interactions. For other strong-coupling regions, the formulas developed above are equally applicable but not further discussed in this paper.

6.4 Results

6.4.1 Comparison with the IDMFT and MC calculations

For a perturbative method like the SC expansion method, it is always necessary to determine the parameter regions where the approximation is valid. Here, we use the previous results obtained from IDMFT and MC methods [92] as a reference to determine the accuracy of the SC calculation. It is also worthwhile to notice that the three methods require substantially different computational times. The SC calculation usually takes

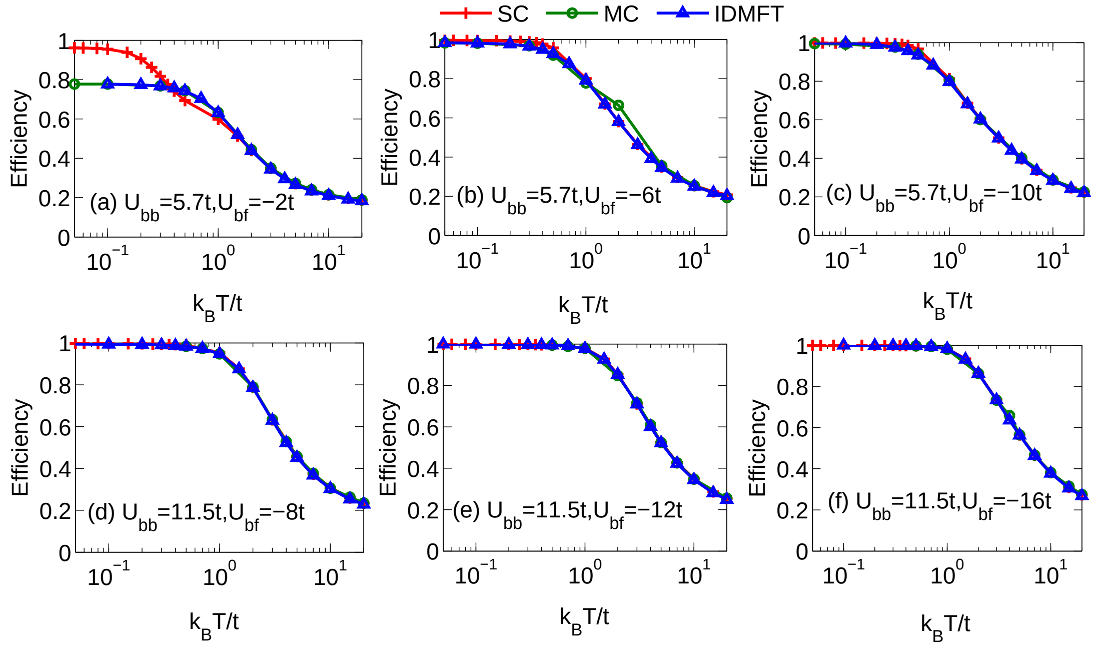

Figure 6.1: (Color on-line) Efficiency $\mathcal{E}$ as a function of temperature calculated by the SC (red cross), IDMFT (blue triangle) and MC (green circle) methods. The interaction parameters, U_{bb} and U_{bf}, are shown in each plot. In (a), the SC calculation differs from the other two methods for $T < 1t/k_B$. For this region, the SC expansion formulas derived here are no longer accurate. In (b)-(f), all three methods give almost identical results. These calculations also show that almost 100% efficiency is reached for relatively strong attraction, $U_{bf} \geq -6t$, at low temperature, $T < t/k_B$.

less than 1 CPU hour while for the same system the IDMFT calculation takes on the order of 10^5 CPU hours. We consider all the parameters used in the previous work [92]. The lattice is 50×50 square lattice with the trap frequency Ω for both species fixed at $\hbar\Omega/2ta = 1/11$. The parameters U_{bf} and U_{bb} are chosen based on a typical experimental setup : $U_{bf}/t = -8, -12, -16$ for $U_{bb}/t = 11.5$ and $U_{bf}/t = -2, -6, -10$ for $U_{bb} = 5.7$. The total number of bosons and fermions are set to be 625. We consider the temperature range $0.05t/k_B$ to $20t/k_B$.

In Fig. 6.1, we show the efficiency as a function temperature calculated with the three methods. Overall, we find excellent agreement between the SC result and the IDMFT and MC calculations and it is clear that high (unit) efficiency can be achieved when the temperature is low ($T \sim 0.1t/k_B$) and the interaction is large compared with t. In the case of $U_{bf} = -2t$ and $U_{bb} = 5.7t$, the SC calculation starts to deviate greatly from the IDMFT and MC calculation when $T \leq 1t/k_B$. It is worth noting that for $T > 1t/k_B$, the SC calculations agree nicely with the other methods even for a relatively weak cross-species interaction, $U_{bf} = -2t$.

The difference between the SC calculation and the other two methods can be understood from the fact that the SC method is a perturbative method based on the atomic limit of the Hamiltonian, $t = 0$ and that the properties derived from the SC expansion are dominated by the atomic-limit behavior with relatively small corrections from the hopping. In the atomic limit, bosons and fermions are completely localized and the only density fluctuations are due to thermal fluctuations. For the low density case considered here, the bosons always form a plateau of unit filling at the center of trap at low temperature and the fermions are attracted by the bosons one by one and form an almost identical plateau. The efficiency therefore always converges to unity as temperature deceases. In Fig. 6.1, we indeed find the efficiency from the SC calculation always goes to one at low temperatures. The convergence to unity is also true for the IDMFT and MC calculations for all the parameters except for $U_{bf}/t = -2$ and $U_{bb}/t = 5.7$. That's where the SC calculation differs from the IDMFT and MC calculation. It is reasonable to assume that the SC calculation can be applied to the region where the ground state of the system is a localized, Mott insulator like state.

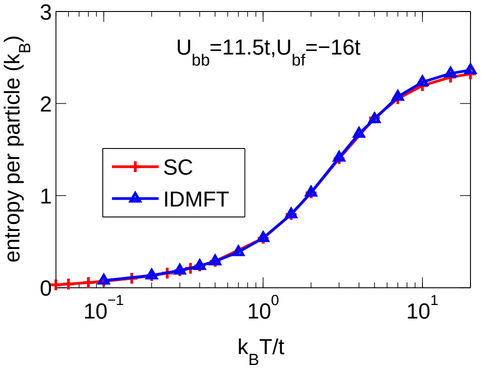

Figure 6.2: (Color on-line) (a) Entropy per particle as a function of temperature T. The SC calculation is marked with red crosses and the IDMFT calculation by the blue line. We find excellent agreement between the SC calculation and the IDMFT calculation.

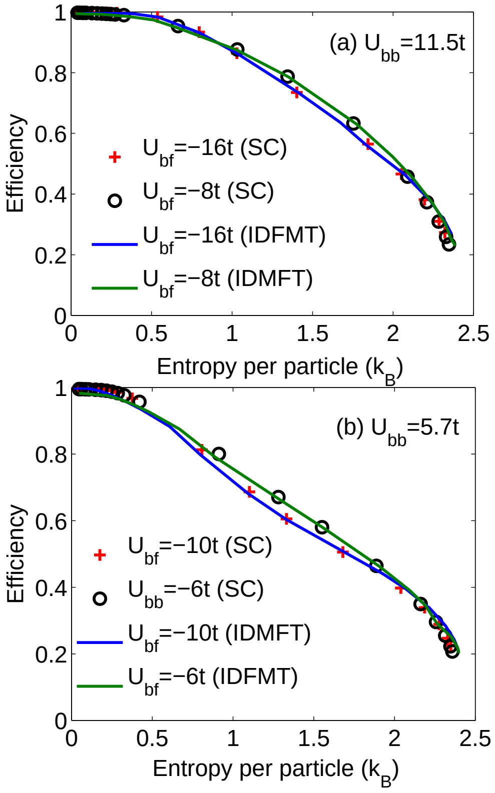

Figure 6.3: (Color on-line) Efficiency as a function of entropy per particle for different interaction parameters. Note here that we didn't include the case of $U_{bf} = -2t$, because it is already shown in Fig. 6.1 that the SC calculation is not accurate for low temperatures in this case. In (a) and (b), we consider two different bosonic interaction strengths and five different inter-species interaction strengths. For all parameters, the efficiency reaches 100% when the entropy is very low. For an intermediate entropy, with an entropy per particle around $1k_B$, the efficiency is around 80%.

The SC calculation of the entropy per particle is also compared with the IDMFT and MC calculations for all the parameters using Eqs. (6.44-6.47). The conclusion of the comparison is similar with the efficiency calculation, that the SC calculation is accurate except for $U_{bf} = -2t$. In Fig. 6.2 we use one example, $U_{bb} = 11.5t$ and $U_{bf} = -16t$, to represent all the cases where the SC calculation agrees with the IDMFT calculation. As the temperature increases, the entropy per particle starts to saturate at around $\sim 2.3k_B$. In the next section, we will show that this saturation is actually the result of finite-size effects.

In Fig. 6.3, we show the behavior of the efficiency as a function of the entropy per particle. This figure can be compared with Fig. 2 in Ref. [92], where the IDMFT calculation is discussed. We verify the findings from the previous work that for strongly attractive inter-species interactions, an efficiency of 100% can be achieved at low temperature (low entropy) region. For an entropy per particle around $1k_B$, a 80% efficiency can still be reached. This efficiency is much higher than what has been achieved in experiment [90].

In the following discussion on the SC calculation result, we no longer consider the case of $U_{bf} = -2t$. This is also based on the consideration that the interaction of $U_{bf} = -2t$ is too weak to achieve the desired high efficiency of pre-formed molecules and therefore is not in the parameter region of the main interest in this paper.

6.4.2 Finite-size effects

In our calculations, we always assume a hard-wall boundary condition at the edge of the lattice. In experiments, however, the atoms are confined only by the trapping potential. This additional confinement imposed by the boundary condition can potentially affect the accuracy of our calculation. This finite-size effect can be neglected if the system is so large that the atoms trapped by the trapping potential almost never reach the edge the system. This, however, is not always the case for the 50×50 lattice. This problem is difficult to address with the IDMFT and MC methods, because of the high computational costs. The SC method, on the other hand, can calculate much larger systems for a fraction of the cost.

In this section, we discuss our calculation for different lattice sizes and discuss finite size effects for different lattice sizes. To benchmark the SC calculations, the trap frequency

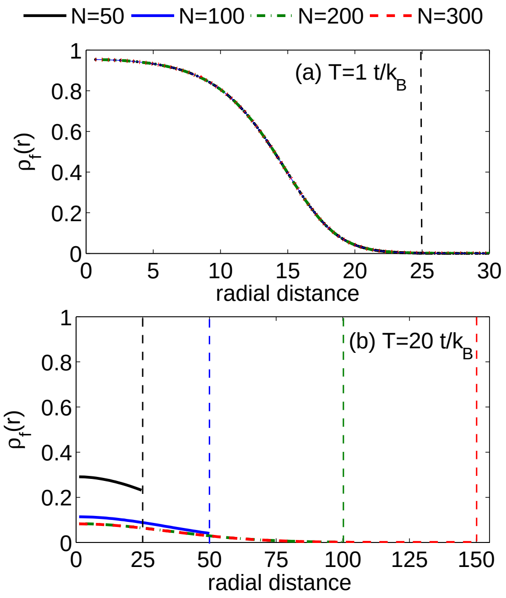

Figure 6.4: (Color on-line) Finite-size effects on the radial density profile. We assume a two-dimensional $N \times N$ square lattice with hard-wall boundary conditions. The dotted lines indicate the boundaries of different lattices.The interaction parameters are $U_{bf} = -16t$, $U_{bb} = 11.5t$. We use the density distribution of the fermionic particle to represent the general dependence of density on the lattice size. In (a), we consider the case of low temperature, $T = t/k_B$. Here, the density distribution is concentrated at the center of the trap and there is no difference between different lattice sizes. In (b), we consider the case of high temperature at $T = 20t/k_B$. Here, the density is confined mainly by the size of the lattice. For $N = 50$, the density is confined at the edge of the lattice, $r = 25$. For $N = 100$, the density is again confined at the edge, $r = 50$. For both $N = 200$ and 300, the density goes to zero before reaching the edge of the lattice and the two distributions overlap with each other. We estimate that finite-size effects are eliminated for the 300×300 square lattice for the trap frequency and number of particles considered here.

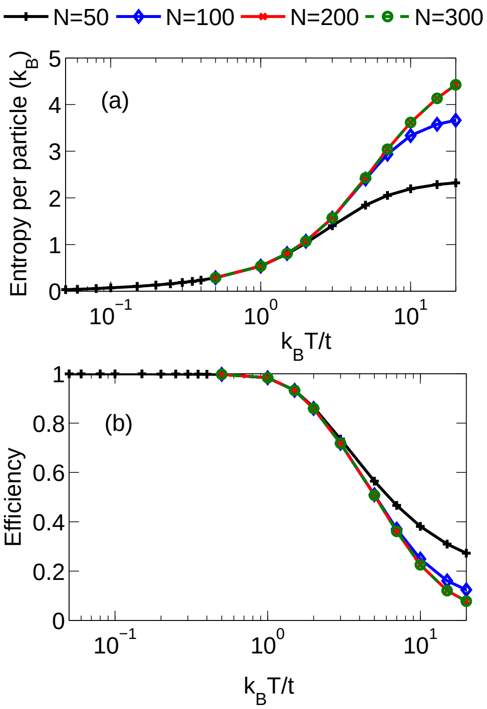

Figure 6.5: (Color on-line) Finite-size effects on the entropy per particle and the efficiency. We assume a two-dimensional $N \times N$ square lattice with hard-wall boundary conditions. The interaction parameters are $U_{bf} = -16t$, $U_{bb} = 11.5t$. In (a), we show the behavior of the entropy per particle as a function of temperature for different system sizes. We see the entropy is significantly affected by the finite size when the lattice is smaller than around 200×200. The finite-size effect is not noticeable at lower temperature ($T < 1t/k_B$).

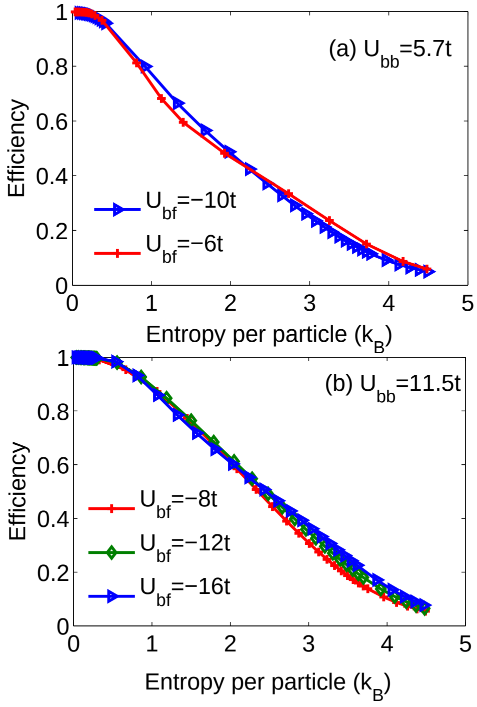

Figure 6.6: (Color on-line) Efficiency as a function of entropy per particle for a 300×300 square lattice system. We consider 625 atoms for each species. Compared with Fig. 6.3, the efficiency is significantly higher for the same value of the entropy per particle in the 300×300 lattice system when the entropy per particle is large. On the other hand, the behavior is similar in both lattice systems when the entropy per particle is less than $1k_B$. The unit efficiency is reached roughly when the entropy per particle is less than $0.5k_B$.

and the total number of particles are fixed for all different lattice sizes. We assume the largest lattice sizes are sufficient to neglect the finite-size effects. In Fig. 6.4, we show the density profile as a function of the lattice size at two temperatures, $T = t/k_B$ (a) and $T = 20t/k_B$ (b). Here Fig. 6.4 (a) represents the scaling behavior in the low temperature region, where there is no significant difference between different lattice sizes and Fig. 6.4 (b) represents the scaling behavior in the high-temperature region, where the system of small lattice size is highly affected by the boundary effect. Note that the horizontal axes are different scales in the two panels. The parameters used in the plots are $U_{bf} = -16t$ and $U_{bb} = 11.5t$. We find similar behavior of the density profile for all the other parameters.

In Fig. 6.5 (a), we show entropy per particle as a function of temperature at different lattice sizes. In this plot, we find that for small lattices, the entropy per particle becomes *saturated* at high temperature, while for large lattices it keep increasing as the temperature increases. The saturation is understood as the result of the finite-size effects. When the temperature is high, atoms tend to expand to a larger area in the trap, which leads to a large cloud size and higher entropy. When atoms expand to the edge of the lattice, the possible occupied sites are now constrained and the entropy stays similar even though the temperature increases, hence the saturation. When the lattice is sufficiently large, atoms can freely expand as the temperature increases and the entropy keeps increasing.

The confinement of the atomic cloud in high temperature also affects the efficiency calculation. In Fig. 6.5 (b), we find that the efficiency saturates to a higher value for smaller lattices. This is because the confinement increases the density overlap between the two species. In the low temperature region, the atoms are close to unit filling at the center of the trap and the efficiency is similar for all difference lattice sizes.

We find that a lattice of 300×300 sites is sufficient to eliminate the finite size effects for our parameter regions. Hence, we use this lattice size for the efficiency and entropy per particle calculations. In fig. 6.6, we show the result for the efficiency as a function of the entropy per particle. We estimate the calculation result from the 50×50 lattice is accurate when the temperature is around or below $T = 1.25t/k_B$.

6.5 Thermometry

6.5.1 Temperature and Density fluctuations

Based on the fluctuation-dissipation theorem, the compressibility can be related to the density fluctuations as [104],

$$\kappa = \frac{\partial \rho(r)}{\partial \mu} = \frac{1}{k_B T}\langle \rho(r) N\rangle - \langle \rho(r)\rangle\langle N\rangle, \tag{6.48}$$

where $\rho(r)$ is the radial density profile, μ is the chemical potential and N is the total number of particles. For a system with a spherically symmetric harmonic trapping potential, $-V_t r^2$, the local chemical potential at a radial distance r is $\mu - V_t r^2$. Within the local density approximation, the trapping potential is interpreted as a variance in the chemical potential and the compressibility in the trapped system can be re-written as a function of the density gradient,

$$\frac{\partial \rho(r)}{\partial \mu} = -\frac{1}{2V_t r}\frac{\partial \rho(r)}{\partial r}. \tag{6.49}$$

These two equations lead to a simple relationship between the density gradient and the density fluctuations in the trapped system,

$$-\frac{1}{2V_t r}\frac{\partial \rho(r)}{\partial r} = \frac{1}{k_B T}\left(\langle \rho(r) N\rangle - \langle \rho(r)\rangle\langle N\rangle\right). \tag{6.50}$$

Based on this relationship, one can determine the temperature from the independently measured density gradient and density fluctuations. For a two dimensional system, a simplified relationship can be found by integrating the above equation over all the two dimensional plane,

$$\frac{\pi}{V_t}\rho(0) = \frac{1}{k_B T}\left(\langle N^2\rangle - \langle N\rangle^2\right). \tag{6.51}$$

Here, $\rho(0)$ stands for the density at the center of the trap.

With the development of *in situ* measurements, it is now possible to measure the den-

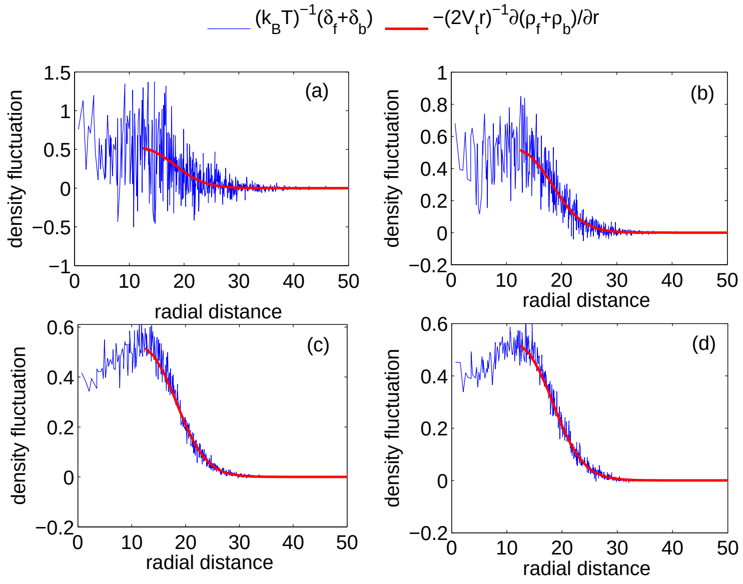

Figure 6.7: (Color on-line) Density fluctuations averaged over different numbers of samples. The density fluctuations shown here are the total density fluctuations divided by the input temperature, $T = 2tk_B^{-1}$. All the fluctuations are compared with $-(2V_tr)^{-1}\partial(\rho_b + \rho_f)/\partial r$. According to Eq. (6.50), these two quantities should equal to each other. In (a)-(c), the total number of configuration generated is 2×10^5, with a different sampling strategy. In (a), one sample is taken at every 10^3 configurations, which gives a total of 200 samples to average over. The statistical error in this case is very large. In (b), one sample is taken at every 100 configurations, which gives a total of 2000 samples. The statistical error is reduced compared with (a). In (c), the total number of samples is 2×10^4. The statistical error is the smallest among (a) to (c). In (d), a total of 2×10^6 configurations are generated and 2×10^4 samples are taken at every 100 configurations.

sity gradient and the fluctuations [111, 47] in experiment and this thermometry scheme has shown promise to be a reliable way of estimating the temperature [104, 113]. Here we test this method for the Bose-Fermi mixtures and Eqs. (6.50 and 6.51) are extended to mixtures by considering the density as the total density of both species and the total number as the total number of both species. With the SC method, we calculate the density gradient directly from the density profile expressions. To simulate the fluctuations measured in the experiments, we use a simplified MC simulation explained in the next section.

6.5.2 Fluctuation calculation

The MC simulation method generates a large collection of states (or configurations) that satisfies the thermal equilibrium criteria. Such collection of states constitutes a thermal ensemble. In the ensemble, each state (or configuration) gives one density distribution, analogous to one single shot image of the density in the experiment. By averaging over all configurations, one obtains the averaged distribution of particles. Deviations between different configurations are the fluctuations. In our simplified MC method, we use the SC method to determine the density distribution for a given temperature and then use the probability as a reference for configuration generation. The ensemble of configurations is decided to be large enough if it can reproduce the input probabilities.

Determining the joint probability : the joint probability, $P^j_{n,m}$, is the joint probability of having n bosons and m fermions at site j. For $m = 1$, the joint probability of having n bosons and 1 fermion at site j can be found from the fermionic density distribution, similar to the calculation of the local efficiency $\mathcal{E}_j$ (indeed, $\mathcal{E}_j = P^j_{1,1}$),

$$P^j_{n,1} = P^{j(0)}_{n,1} - P^{j(1)}_{n,1} + P^{j(2)}_{n,1}, \tag{6.52}$$

where we again write the probability as a sum of the probability in the atomic limit,

$$P^{j(0)}_{n,1} = \frac{\phi_{b,j}(n)\phi_{f,j}(n)}{\mathcal{Z}^{(0)}_j}, \tag{6.53}$$

and the contributions from the hopping,

$$\begin{aligned} P^{j(1)}_{n,1} = \; & \beta \sum_k \frac{\phi_{b,j}(n)\phi_{f,j}(n)}{\mathcal{Z}^{(0)}_j} \times \\ & \sum_{n_{b,j},n_{b,k}} \left[\frac{\phi_{b,j}(n_{b,j})\phi_{b,k}(n_{b,k})}{\mathcal{Z}^{(0)}_j \mathcal{Z}^{(0)}_k} \right. \\ & \left. \times \frac{\phi_{f,j}(n_{b,j}) - \phi_{f,k}(n_{b,k})}{\bar{\mu}_{f,j}(n_{b,j}) - \bar{\mu}_{f,k}(n_{b,k})} \right] \end{aligned} \tag{6.54}$$

$$P^{j(2)}_{n,1} = \sum_k \sum_{n_{b,k}} \frac{\phi_{b,j}(n)\phi_{b,k}(n_{b,k})}{\mathcal{Z}^{(0)}_j \mathcal{Z}^{(0)}_k} \times \left[\frac{\beta\phi_{f,j}(n)}{\bar{\mu}_{f,j}(n) - \bar{\mu}_{f,k}(n_{b,k})} \right.$$

$$+ \frac{\phi_{f,k}(n) - \phi_{f,j}(n_{b,k})}{[\bar{\mu}_{f,j}(n) - \bar{\mu}_{f,k}(n_{b,k})]^2} \Bigg] . \tag{6.55}$$

Once the joint probability $P^j_{n,1}$ is determined, the complementary probability $P^j_{n,0}$ is found based on the relationship in the atomic limit,

$$\sum_n \left[P^{j(0)}_{n,1} + \frac{\phi_{b,j}(n)}{\mathcal{Z}^{(0)}_j} \right] = 1. \tag{6.56}$$

Taking into the account the hopping contributions, we can write $P^j_{n,0}$ as,

$$P^j_{n,0} = \frac{\phi_{b,j}(n)}{\mathcal{Z}^{(0)}_j} + P^{j(1)}_{n,1} - P^{j(2)}_{n,1}. \tag{6.57}$$

We assume each lattice site is independent and the joint probability at site j is sufficient to determine the density distribution at site j. The joint probabilities are evaluated for all the lattice sites and stored in a table before the MC procedure.

Simulation procedure: we use a random number generator to generate configurations with reference to the joint probability table. Specifically the simulation includes the following steps:

1) Create a table for the values of $\widetilde{P}^j_{n,m}$ corresponding to the sum of the joint probability of having *up to* n bosons and up to m fermions at site $j = 1$, i.e.

$$\widetilde{P}^j_{n,m} = \sum_{k=0}^{n} \sum_{l=0}^{m} P^j_{k,l}. \tag{6.58}$$

2) Generate a random number x between 0 and 1.

3) Find the smallest $\widetilde{P}^j_{n',m'}$ that is larger than x. The number of bosons and fermions at site j is then equal to n' and m'.

4) Repeat steps (2) and (3) to another site, $j = 2$, until all the lattice sites are considered. Store the configuration.

5) Repeat steps (2)-(4) $\mathcal{N}$ times to generate $\mathcal{N}$ configurations.

To avoid auto-correlation between adjacent configurations, we choose every other $\mathcal{M} \gg 1$ configurations as samples. The total number of samples is then $N_s = \mathcal{N}/\mathcal{M}$. Averaging over all the samples, we obtain the fermionic and bosonic part of the density fluctuation as

$$\delta_{f(b)}(r) = \langle \rho_{f(b)}(r)(N_f + N_b) \rangle - \langle \rho_{f(b)}(r) \rangle \langle N_f + N_b \rangle, \tag{6.59}$$

and the total density fluctuation is the sum of δ_f and δ_b. The total number fluctuation is defined as

$$\Delta = \langle (N_f + N_b)^2 \rangle - \langle N_f + N_b \rangle^2. \tag{6.60}$$

Here the bracket stands for the averaging over all samples in analogy to the experimental measurement of the fluctuations.

6.5.3 Results

The fluctuation calculation is carried out for a 300×300 lattice with all five sets of parameters. Overall we find very similar behavior for all the parameters and we use parameters $U_{bb} = 11.5t$ and $U_{bf} = -16t$ as an example. In our simulation, the fluctuations between different configurations are from both the random number generator and the thermal fluctuations. The difference between them is that the thermal fluctuations are independent of ensemble sizes and the sampling size. We find that the correct thermal fluctuation calculation requires a large number of samples ($\sim 10^4$) and large ensemble sizes ($\sim 10^6$). Because of the similarity between the simulation and experimental measurement, this may suggest that a large number of shots are needed in the experiments to obtain the correct thermal fluctuations. Note that we consider here the results from a single plane as one shot, not the averaged results over many planes as reported in Ref. [113].

In Fig. 6.7, we discuss the sampling effects by comparing the fluctuations obtained from different samples with the compressibility calculated from the density gradient. When the number of samples are small, the fluctuations are largely random deviations from the average value. In Fig. 6.7 (a), the fluctuations can be equally positive and negative, which does not even satisfy the condition that the total fluctuations should be always positive. As

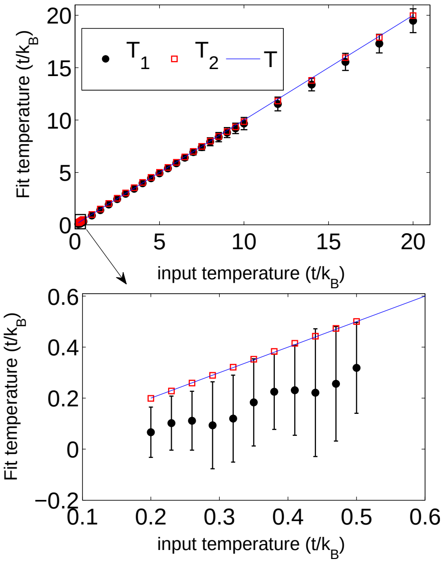

Figure 6.8: (Color on-line) Extracted temperature as a function of the input temperature. The fluctuations are obtained from 2×10^4 samples out of 2×10^6 configurations. The value of T_1 is the mean of $T_1(r)$ averaged over $12 < r/a < 25$ and the error-bar for T_1 is the standard deviation in $T_1(r)$ [Eq. (6.61)]. The value of T_2 is obtained through Eq. (6.62). The input temperature T is drawn as a straight blue line in both plots. In (a), we show our result for the full range of the input temperature, from $T = 0.2t/k_B$ to $20t/k_B$. In this plot, we find very good overall agreement of T_1 and T_2 with the input temperature for the temperature range considered, particularly for $T > 1t/k_B$. In (b), we blow-up the area inside the black square in (a), which corresponds to the low temperature region, where $T = 0.2t/k_B$ to $0.5t/k_B$. In this region, we find that T_1 shows large relative fluctuations (deviation) from the mean value and the mean value of T_1 differs relatively greater from T. The extracted temperature T_2 however still shows excellent agreement with the input temperature.

the number of samples grows, the random noise starts to be averaged out and the fluctuations start to agree with the fluctuation-dissipation theorem. In Fig. 6.7 (c), the fluctuations agree very nicely with the relationship predicted by Eq. (6.50). To show that 10^4 samples are sufficient, we consider an even larger ensemble, with 2×10^6 configurations [Fig. 6.7(d)] and find that the two ensembles produce almost identical results. This shows that the fluctuation calculations obtained in this way are independent of the ensemble size and should correspond to the thermal fluctuations of the system.

With Eqs. (6.50) and (6.51), we define two extracted temperatures, T_1 and T_2. Let $T_1(r)$ be the extracted temperature obtained in terms of the density fluctuations and the density gradient,

$$k_B T_1'(r) = \frac{\delta_f(r) + \delta_b(r)}{(2V_t r)^{-1} \partial(\rho_f(r) + \rho_b(r))/\partial r},\ 12 < r/a < 25. \tag{6.61}$$

Here, we choose the radial distance to be larger than 12 lattice sites because the quantity $(2V_t r)^{-1}\partial(\rho_f(r) + \rho_b(r))/\partial r$ diverges as $r \to 0$ for a finite density gradient and for small r, it goes to zero as the density develops a plateau at unit filling at low temperature. The radial distance is less than 25 lattice sites, because the density is almost zero in the outer regions and that increases the relative error. Together, we find that r between 12 and 25 sites to be the best region to fit the fluctuations and the compressibility with each other. We also note that Eq. (6.50) still holds if one considers just the fermionic or bosonic part of the system, i.e. keep only the index f or b in δ and ρ.

The temperature T_2 is obtained based on Eq. (6.51), which translates into the following expression for the Bose-Fermi mixture,

$$k_B T_2 = \frac{\Delta}{\pi V_t^{-1} \left[\rho_f(0) + \rho_b(0)\right]}. \tag{6.62}$$

Here $\rho_f(0)$ is the density of fermions at the center of the trap and $\rho_b(0)$ the density of bosons at the center of the trap.

In Fig. 6.8, we show T_1 and T_2 as a function of input temperature. Overall, we find very good agreement between T_1 and T_2 with the input temperature [Fig. 6.8 (a)]. We also find in the low temperature region, T_2 generally fits better with the input temperature [Fig. 6.8 (b)]. This finding suggests that the statistical error introduced by the numerically generated ensemble is lower in the calculation of T_2 and this could be because the calculation of T_2 only involves the first-order observable, the density and the total number fluctuation, whereas, for the calculation of T_1, we need to calculate the second-order observable, the density fluctuation, which may be more susceptible to statistical errors in the numerical simulation.

6.6 Summary

The SC expansion method is a very efficient way of studying thermal properties of strongly interacting systems. Through comparison with the IDMFT and MC calculations, we show that the strong coupling expansion method can be used for a wide range of parameters even at low temperature when the attractive interaction between the two species is relatively strong. We use the SC method to evaluate the finite-size effects in our previous calculations. This leads to important modifications of the efficiency and the entropy per particle at high temperature. The SC calculation also provides a way to simulate experimental measurements of the fluctuations. Based on the simulation, we find that the thermometry proposal based on the fluctuation-dissipation theorem is accurate for heavy-bose-light-fermi mixtures. This scheme suggests an effective thermometry scheme that works in the extreme low temperature in the deep lattice region. Overall, our work shows a promising way of creating strongly interacting quantum degenerate dipolar matter by loading the mixtures onto an optical lattice before the molecule formation. In addition to higher efficiency, the molecules created in this way are already situated in the optical lattice and can be directly adjusted to realize the novel quantum phases that require the presence of a lattice. It is also worth noting that the SC approach can be used to study other mixtures with modifications. For Fermi-Fermi mixtures like ^{6}Li-^{40}K, it would require just truncating the heavy bosonic states. For Bose-Bose mixtures like ^{87}Rb-^{133}Cs, the modification requires allowing for the superfluid order to occur.

Chapter 7

Conclusion and further discussions

From the Luttinger liquid theory to the TEBD method to the SC expansion, we have used both theoretical and numerical methods to study quantum many-body phenomena in atomic mixtures in optical lattices.

We start our discussion with a binary bosonic mixture in an optical lattice. We use the Luttinger liquid theory to solve the model in one dimension and determine all the quasi-long range orders that can exist in this model as well as the asymptotic behavior of the correlation functions. The Luttinger liquid calculation is compared with the TEBD calculation which evaluates the exact ground state of the one dimensional system. The study leads to two phase diagrams which include the parameter regions for all the quasi-long range orders.

Using large-scale parallel computing, we are able to calculate the noise correlation functions exactly. We find that every order has its distinctive signals in the noise correlation functions. The result shows again the importance of the fluctuations in studying the higher-order correlations and it is particularly useful in experiment for the detection of orders that can not be detected in the time-of-flight image.

Transport properties of the mixtures are also very different from the single species system because of the inter-species correlation. Here, interesting transport properties are found in the paired superfluid state as a result of the pairing order and in the counter-flow superfluid state as result of the anti-pairing order.

For the last part of the discussion, we consider the light-Fermi-heavy-Bose mixture in an optical lattice. We use a grand canonical ensemble to describe the system and derive analytical expressions for various thermal quantities based on the strong coupling expansion method. By studying the joint probability of having exactly one boson and one fermion on one site as a function of the temperature, the inter-species interaction and the lattice depth, we show how the presence of the optical lattice can significantly increase the efficiency of binding bosonic and fermionic particles. The result also illustrates the phenomena of pre-formed molecules as a many-body effect.

In both mixtures, we find interesting many-body phenomena that can not be explained on the single-particle or few-particle level. Such many-body phenomena are crucial for understanding the behavior of ultra-cold atoms, especially when the interactions are strong. Such many-body phenomena also lead to new properties that have not been observed before. With the rapid experimental progress, many new many-body phenomena are waiting to be explored and new theoretical methods are waiting to be developed.

First, the realization of the synthetic vector potential field [114] and the creation of polar molecules with long range interactions [90] have shown great promise that the atomic systems can simulate novel condensed matter models. From a theoretical point of view, this leads to great interests of predicting novel phase transitions and novel dynamical properties by transforming the condensed matter models into models more applicable for cold atoms. The TEBD method can be easily applied to many of such models in one dimension or quasi-one dimension. Studying the model with a synthetic vector potential field for example is likely to reveal very intriguing many-body energy spectrum and interesting long-range correlations.

Another direction would be to remind ourselves that the system of cold atoms in optical lattices is after all a system of interactive atoms situated in optical and magnetic fields and background thermal gas. The ultra-cold atom experiment is intrinsically a non-equilibrium process. To study the many-body phenomena in such process, one needs to understand the underlying atomic and optical physics. And there are many questions that need to be addressed. For example, is the cold atom system truly a system at the thermal dynamical limit? What kind of role the optical field can play if we treat them dynamically, rather than assume it as a static potential? How to study the loss and other non-equilibrium properties of such systems?

Even although it is difficult to solve the non-equilibrium dynamics of ultra-cold atoms exactly, it is possible to develop various approximated non-equilibrium methods. Numerically for example, it is possible to reconstruct the TEBD method in the reduced density matrix basis to study open quantum systems and thermal properties [115]. Theoretically, various predictions are made about the non-equilibrium steady states that can be realized in ultra-cold atoms.

The extremely accurate control on the atomic level also leads to one other possible direction related to quantum chemistry, that the atoms can be manipulated into bounded states of the lowest rovibrational level and form molecules. Such production of artificial molecules in the extremely low temperature can lead to a series of interdisciplinary questions between chemistry and atomic physics. The study on synthetic molecules productions can also benefit from the understanding of the many-body correlations between the interacting particles, which can lead to the reduction of three-body loss, the increased probability of pre-form molecules, etc.

To summarize, many-body phenomena in ultra-cold atom systems need to be studied with atomic physics, quantum optics and condensed matter physics combined. But to truly combine these fields of physics is not easy. From the point of view of condensed matter physics, the microscopic details of the system can be neglected and only the collective behavior is concerned. From the point of view of atomic physics and optics, the microscopic mechanism of the interactions and the effects of the external fields are important, while the many-body aspects are neglected. The challenge is how to develop models that are simple (from the many-body theory perspective) and sufficient (from the atomic physics perspective) to capture the complex nature of ultra-cold atoms. The truly new many-body phenomena in ultra-cold atoms are still waiting to be discovered.

Bibliography

[1] I. Bloch, J. Dalibard, and W. Zwerger, *Rev. Mod. Phys*. **80**, 885 (2008).

[2] O. Morsch and M. Oberthaler, *Rev. Mod. Phys.* 78, 179 (2006).

[3] S. Giorgini, L. P. Pitaevskii, and S. Stringari, *Rev. Mod. Phys.* **80**, 1215 (2008).

[4] S. Bose, *Z. Phys. 26*, **178** (1924); A. Einstein, *Sitzungsber. K. Preuss. Akad. Wiss., Phys. Math. Kl.*, **261** (1924); *Sitzungsber. K. Preuss. Akad. Wiss., Phys. Math. Kl.*, **3** (1925).

[5] K. B. Davis, M. -O. Mewes, M. R. Andrews, N. J. van Druten, D. S. Durfee, D. M. Kurn and W. Ketterle, *Phys. Rev. Lett.* **75** 3969 (1995); M.H. Anderson, J. R. Ensher, M. R. Matthews, C. E. Wieman and E. A. Cornell, *Science* **269** 198 (1995); C. C. Bradley, C. A. Sackett, J. J. Tollett, R. G. Hulet, *Phys. Rev. Lett.* **75** 1687 (1995).

[6] B. DeMarco, and D. D. Jin, Science 285, 1703 (1999); F. Schreck, , L. Khaykovich, K. L. Corwin, G. Ferrari, T. Bourdel, J. Cubizolles, and C. Salomon, Phys. Rev. Lett. 87, 080403 (2001).

[7] C. Chin, R. Grimm, P. Julienne, and E. Tiesinga, Rev. Mod. Phys. 82, 1225 (2010).

[8] M. Greiner, M. O. Mandel, T. Esslinger, T. Hänsch, and I. Bloch, *Nature* 415, 39 (2002a).

[9] M. Raizen, C. Salomon, and Q. Niu, *Phys. Today* 50, No. 7, 30 (1997)

[10] D. Jaksch, C. Bruder, J. I. Cirac, C. W. Gardiner, and P. Zoller, *Phys. Rev. Lett.* **81** , 3108 (1998).

[11] M. Greiner, O. Mandel, T. Esslinger, T. W. Hänsch and I. Bloch, *Nature* **415**, 39 (2002).

[12] I. B. Spielman, W. D. Phillips, and J. V. Porto , *Phys. Rev. Lett.* **98**, 080404 (2007).

[13] T. Stöferle, H. Moritz, M. Köhl and T. Esslinger, *Phys. Rev. Lett.* **92**,130403(2004).

[14] A. L. Fetter and J. D. Walecka, *Quantum Theory of Many-Particle Systems*, (Dover Publications, 2003).

[15] O. Penrose, *Phil. Mag.* **42**, 1373 (1951); O. Penrose and L. Onsager, *Phys. Rev.* **104**, 576 (1956).

[16] C. N. Yang, *Rev. Mod. Phys.* **34** 694 (1962).

[17] L.N. Cooper, *Phys. Rev.* **104** 1189 (1956); J. Bardeen, L. N. Cooper and J. R. Shrieffer, *Phys. Rev.* **106** 162 (1957); *Phys. Rev.* **108** 1175 (1957).

[18] G. G. Batrouni, F. Hébert and R. T. Scalettar, *Phys. Rev. Lett.* **97**, 087209 (2006); V. W. Scarola and S. Das Sarma, *ibid.* **95**, 033003 (2005); P. Sengupta1, L. P. Pryadko1, F. Alet, M. Troyer and G. Schmid, *ibid.* **94**, 207202 (2005); S. Wessel and M. Troyer, *ibid.* **95**, 127205 (2005); D. Heidarian and K. Damle, *ibid* **95**, 127206 (2005); R. G. Melko, A. Paramekanti, A. A. Burkov, A. Vishwanath, D. N. Sheng, and L. Balents, *ibid.* **95**, 127207 (2005); H.P. Büchler and G. Blatter, *ibid.* **91**, 130404 (2004); M. Boninsegni and N. Prokof'ev, *ibid.* **95**, 237204 (2005); C. Trefzger, C. Menotti, M. Lewenstein, *Phys. Rev. Lett.* **103**, 035304 (2009).

[19] M.P.A. Fisher, P.B. Weichman, G. Grinstein, and D.S. Fisher, *Phys. Rev. B* **40**, 546 (1989).

[20] D. B. M. Dickerscheid, D. van Oosten, P. J. H. Denteneer, and H. T. C. Stoof, *Phys. Rev. A* **68**, 043623 (2003).

[21] V. A. Kashurnikov, N. V. Prokof'ev, and B. V. Svistunov, Phys. Rev. A 66, 031601(R) (2002). G. G. Batrouni, V. Rousseau, R. T. Scalettar, M. Rigol, A. Muramatsu, P. J. H. Denteneer, and M. Troyer, Phys. Rev. Lett. 89, 117203 (2002). B. Capogrosso-Sansone, N. V. Prokof'ev, and B. V. Svistunov, Phys. Rev. B 75, 134302 (2007).

[22] J. K. Freericks and H. Monien, Phys. Rev. B 53, 2691 (1996).

[23] B. Paredes, A. Widera, V. Murg, O. Mandel, S. Foelling, I. Cirac, G. Shlyapnikov, T. W. Hansch and I. Bloch, *Nature* **429**, 277 (2004).

[24] T. Giamarchi, *Quantum physics in one dimension*, (Oxford Univ. Press, Oxford, UK, 2004).

[25] F. D. M. Haldane, *Phys. Rev. Lett.* **47**, 1840 (1981).

[26] M. Girardeau, J. Math. Phys. 1, 516 (1960); E. H. Lieb, and W. Liniger, Phys. Rev. 130, 1605(1963).

[27] J. M. Kosterlitz and D. J. Thouless, *J. Phys. C* **6**, 1181 (1973); V. L. Berezinskii, Zh. Eksp. Teor. Fiz. **6**, 907 (1970) [Sov. Phys. JETP **32**, 493 (1971)].

[28] P. Pippan, H. G. Evertz, and M. Hohenadler, *Phys. Rev. A* **80**, 033612 (2009).

[29] C. Kollath, U. Schollwöck, J. von Delft, and W. Zwerger, Phys. Rev. A 69, 031601(R) (2004). Steven R. White, Phys. Rev. Lett. 69, 2863 (1992); Phys. Rev. B 48, 10345 (1993).

[30] E. Altman, E. Demler, and M. D. Lukin, *Phys. Rev. A* **70**, 013603 (2004).

[31] A. Widera, S. Trotzky, P. Cheinet, S. Fölling, F. Gerbier, and I. Bloch , *Phys. Rev. Lett.* **100**, 140401 (2008)S. Fölling, F. Gerbier, A. Widera, O. Mandel, T. Gericke, and I. Bloch, *Nature* **434**, 481-484(2005).

[32] I. B. Spielman, W. D. Phillips, and J. V. Porto, *Phys. Rev. Lett.* **98**, 080404 (2007).

[33] M. Greiner, C. A. Regal, J. T. Stewart, and D. S. Jin, *Phys. Rev. Lett.* **94**, 110401 (2005).

[34] A. Imambekov, I. E. Mazets, D. S. Petrov, V. Gritsev, S. Manz, S. Hofferberth, T. Schumm, E. Demler, and J. Schmiedmayer, *Phys. Rev. A* **80**, 033604 (2009).

[35] L. Mathey, A. Vishwanath, and E. Altman, *Phys. Rev. A* **79**, 013609 (2009).

[36] L. Mathey, E. Altman, and A. Vishwanath, *Phys. Rev. Lett.* **100**, 240401 (2008).

[37] V. W. Scarola, E. Demler, and S. Das Sarma, *Phys. Rev. A* **73**, 051601(R) (2006).

[38] A. Lüscher and A. M. Läuchli, *Phys. Rev. A* **76**, 043614 (2007); A. Lüscher, R. M. Noack, and A. M. Läuchli, *Phys. Rev. A* **78**, 013637 (2008).

[39] L. Mathey, I. Danshita and C. W. Clark, *Phys. Rev. A* **79**, 011602(R) (2009).

[40] A. M. Rey, I. I Satija, and C. W Clark, *J. Phys. B* **39,** S177-S190 (2006); A. M. Rey, I. I. Satija, and C. W. Clark, *Phys. Rev. A* **73**, 063610 (2006).

[41] K. Nelson, X. Li, and D. Weiss, *Nature Phys.* **3**, 556(2007),

[42] M. Karski, L. Förster, J. M. Choi, W. Alt, A. Widera, and D. Meschede, *Phys. Rev. Lett.* **102**, 053001 (2009) .

[43] Gericke, T., Würtz, P., Reitz, D., Langen, T. & Ott, *Nature Phys.* **4**, 949(2008).

[44] A. Itah, H. Veksler, O. Lahav, A. Blumkin, C. Moreno, C. Gordon, and J. Steinhauer, *Phys. Rev. Lett.* **104**, 113001 (2010).

[45] M. Greiner, O. Mandel, T. Esslinger, T. W. Hänsch, I. Bloch, *Nature* **415**, 39 (2002).

[46] W. S. Bakr, A. Peng, M. E. Tai, R. Ma, J. Simon, J. I. Gillen, S. Fölling, L. Pollet, M. Greiner, *Science* **329**, 547 (2010).

[47] N. Gemelke, X. Zhang, C. Hung and C. Chin, *Nature* **460**, 995 (2009).

[48] G. Vidal, *Phys. Rev. Lett.* **91**, 147902 (2003).

[49] G. Vidal, *Phys. Rev. Lett.* **93**, 040502 (2004).

[50] G. Vidal, *Phys. Rev. Lett* **98**, 070201 (2007); S. R. White and A. E. Feiguin, *ibid.* **93**, 076401 (2004); I. Danshita and P. Naidon, *Phys. Rev. A* **79**, 043601 (2009); I. Danshita and C. W. Clark, *Phys. Rev. Lett.* **102**, 030407 (2009); L. D. Carr, M. L. Wall, D. G. Schirmer, R. C. Brown, J. E. Williams, and Charles W. Clark, *Phys. Rev. A* **81**, 013613 (2010);

[51] M. A. Nielsen and I. L. Chuang, *Quantum Computation and quantum communication* (Cambridge University Press, 2000).

[52] Y. Y. Shi, L. M. Duan, and G. Vidal, Phys. Rev. A 74, 022320 (2006); I. Danshita and P. Naidon, *Phys. Rev. A* **79**, 043601 (2009).

[53] I. Danshita, J. E. Williams, C. A. R. Sá de Melo, and C. W. Clark, *Phys. Rev. A* **76**, 043606 (2007); I. Danshita, C. A. R. Sá de Melo, and C. W. Clark, *Phys. Rev. A* **77**, 063609 (2008).

[54] M. Suzuki, Phys. Lett. A 146, 319 (1990); J. Math. Phys. 32, 400 (1991).

[55] C. A. Regal, M. Greiner and D. S. Jin, *Phys. Rev. Lett.* **92** 040403 (2004); M.W. Zwierlein, C. A. Stan, C. H. Schunck, S. M. F. Raupach, A. J. Kerman and W. Ketterle, *Phys. Rev. Lett.* **92** 120403 (2004); M. Bartenstein, A. Altmeyer, S. Riedl, S. Jochim, C. Chin, J. Hecker Denschlag and R. Grimm, *Phys. Rev. Lett.* **92** 120401 (2004); T. Bourdel, L. Khaykovich, J. Cubizolles, J. Zhang, F. Chevy, M. Teichmann, L. Tarruell, S. J. J. M. F. Kokkelmans and C. Salomon *Phys. Rev. Lett.* **93** 050401 (2004).

[56] A. B. Kuklov and B. V. Svistunov, *Phys. Rev. Lett.* **90**, 100401 (2003).

[57] A. Kuklov, N. Prokof'ev and B. Svistunov, *Phys. Rev. Lett.* **92**, 050402 (2004);*Phys. Rev. Lett.* **92**, 030403 (2003).

[58] A. Argüelles and L. Santos, Phys. Rev. A 75, 053613 (2007); ibid 77, 059904 (2008).

[59] L. Mathey, *Phys. Rev. B* **75**, 144510 (2007).

[60] C. Trefzger, C. Menotti, M. Lewenstein, arXiv:0904.1552.

[61] A. Masaki, S. Tsukada, and H. Mori, *J. Phys. Conf. Ser.* **150**, 032050 (2009).

[62] M. A. Cazalilla, *J. Phys. B: At. Mol. Opt. Phys.* **37**, S1 (2004).

[63] M.A. Cazalilla, *Phys. Rev. A* **70**, 041604(R) (2004).

[64] J. B. Kogut, *Rev. Mod. Phys.* **51**, 659 (1979).

[65] T. Mishra, R. V. Pai and B. P. Das, *Phys. Rev. A* **76**, 013604 (2007).

[66] J. Stenger, S. Inouye, A. P. Chikkatur, D. M. Stamper-Kurn, D. E. Pritchard, and W. Ketterle, *Phys. Rev. Lett. 82,* 4569 (1999); J. Steinhauer, R. Ozeri, N. Katz, and N. Davidson, *ibid.* **88**, 120407 (2002).

[67] D. Clément, N. Fabbri, L. Fallani, C. Fort, and M. Inguscio, *Phys. Rev. Lett.* **102**, 155301 (2009).

[68] A. Widera, S. Trotzky, P. Cheinet, S. Fölling, F. Gerbier, and I. Bloch , *Phys. Rev. Lett.* **100**, 140401 (2008).

[69] A. Kuklov, N. Prokof'ev and B. Svistunov, *Phys. Rev. Lett.* **92**, 050402 (2004);*Phys. Rev. Lett.* **92**, 030403 (2003).

[70] A. Hu, L. Mathey, I. Danshita, E. Tiesinga, C. J. Williams, and C. W. Clark, *Phys. Rev. A* **80**, 023619 (2009).

[71] C. Menotti and S. Stringari, arXiv:0912.4452.

[72] S. Fölling, A. Widera, T. Müller, F. Gerbier, and I. Bloch, *Phys. Rev. Lett.* **97**, 060403 (2006).

[73] C. D. Fertig, K. M. O'Hara, J. H. Huckans, S. L. Rolston, W. D. Phillips, and J. V. Porto, *Phys. Rev. Lett.* **94**, 120403 (2005).

[74] I. Danshita and C. W. Clark, *Phys. Rev. Lett.* **102**, 030407 (2009).

[75] S. Montangero, R. Fazio, P. Zoller, and G. Pupillo, *Phys. Rev. A* **79**, 041602(R) (2009).

[76] L. D. Carr, D. DeMille, R. V. Krems, and J. Ye, New J. Phys. **11**, 055049 (2009).

[77] S. Ospelkaus, K.-K. Ni, D. Wang, M. H. G. de Miranda, B. Neyenhuis, G. Quéméner, P. S. Julienne, J. L. Bohn, D. S. Jin, J. Ye, *Science* **327**, 853 (2010).

[78] H. P. Büchler, A. Micheli and P. Zoller, *Nature Physics* **3**, 726 (2007).

[79] L. Santos, G. V. Shlyapnikov, P. Zoller, and M. Lewenstein, *Phys. Rev. Lett.* **85**, 1791(2000); K. Góral, L. Santos, and M. Lewenstein, *Phys. Rev. Lett.* **88**, 170406 (2002).

[80] B. Capogrosso-Sansone, C. Trefzger, M. Lewenstein, P. Zoller, and G. Pupillo, *Phys. Rev. Lett*. **104**, 125301 (2010).

[81] D. DeMille, *Phys. Rev. Lett.* **88**, 067901 (2002).

[82] C. Ospelkaus, S. Ospelkaus, L. Humbert, P. Ernst, K. Sengstock, and K. Bongs, Phys. Rev. Lett. 97, 120402 (2006).

[83] J. J. Zirbel, K.-K. Ni, S. Ospelkaus, T. L. Nicholson, M. L. Olsen, P. S. Julienne, C. E. Weiman, J. Ye, and D. S. Jin, Phys. Rev. A 78, 013416 (2008).

[84] J. M. Sage, S. Sainis, T. Bergeman, and D. DeMille, *Phys. Rev. Lett.* **94**, 203001 (2005).

[85] C. Weber, G. Barontini, J. Catani, G. Thalhammer, M. Inguscio, and F. Minardi, Phys. Rev. A 78, 061601(R) (2008).

[86] J. J. Zirbel, K.-K. Ni, S. Ospelkaus, J. P. D'Incao, C. E. Wieman, J. Ye, and D. S. Jin, *Phys. Rev. Lett.* **100**, 143201 (2008).

[87] G. Thalhammer, K. Winkler, F. Lang, S. Schmid, R. Grimm, and J. H. Denschlag, *Phys. Rev. Lett.* **96**, 050402 (2006); K. Pilch, A. D. Lange, A. Prantner, G. Kerner, F. Ferlaino, H.-C. Nägerl, and R. Grimm, *Phys. Rev. A* **79**, 042718 (2009).

[88] K. M. Jones, E. Tiesinga, P. D. Lett, and P. S. Julienne, *Rev. Mod. Phys.* **78**, 483 (2006).

[89] S. Ospelkaus, A. Pe'er, K.-K. Ni, J. J. Zirbel, B. Neyenhuis, S. Kotochigova, P. S. Julienne, J. Ye and D. S. Jin, *Nature Physics* **4**, 622 (2008).

[90] K.-K. Ni, S. Ospelkaus, M. H. G. de Miranda, A. Pe'er, B. Neyenhuis, J. J. Zirbel, S. Kotochigova, P. S. Julienne, D. S. Jin, J. Ye, *Science* **322**, 231 (2008).

[91] D. Jaksch, V. Venturi, J. I. Cirac, C. J. Williams, and P. Zoller, *Phys. Rev. Lett*. **89**, 040402 (2002).

[92] J. K. Freericks, M. M. Maśka, Anzi Hu, Thomas M. Hanna, C. J. Williams, P. S. Julienne and R. Lemański, *Phys. Rev. A* **81**, 011605 (2010); *ibid.* **82**, 039901(E) (2010).

[93] L. M. Falicov and J. C. Kimball, *Phys. Rev. Lett.* **22**, 997 (1969).

[94] C. Ates and K. Ziegler, Phys. Rev. A 71, 063610 (2005).

[95] M. Iskin and J. K. Freericks, *Phys. Rev. A* **80**, 053623 (2009).

[96] C. Gruber and N. Macris, *Helv. Phys. Acta* **69**, 850 (1996); J. Jedrzejewski and R. Lemański, *Acta Phys. Pol. B* **32**, 3243 (2001).

[97] M. M. Maśka, R. Lemański, J. K. Freericks, and C. J. Williams, *Phys. Rev. Lett*. **101**, 060404 (2008).

[98] L. Pollet, C. Kollath, K. V. Houcke, and M. Troyer, New J. Phys. **10**, 065001 (2008);

[99] P. B. Blakie and J. V. Porto, *Phys. Rev. A* **69**, 013603 (2004).

[100] F. Gerbier, Phys. Rev. Lett. 99, 120405 (2007); D. McKay, M. White, and B. DeMarco, *Phys. Rev. A* **79**, 063605 (2009); A. Hoffmann and A. Pelster, Phys. Rev. A 79, 053623 (2009); D. Baillie and P. B. Blakie, *Phys. Rev. A* **80**, 033620 (2009).

[101] L. Pollet, C. Kollath, K. V. Houcke, and M. Troyer, New J. Phys. **10**, 065001 (2008).

[102] D. McKay, M. White, and B. DeMarco, *Phys. Rev. A* **79**, 063605 (2009).

[103] B. Capogrosso-Sansone, E. Kozik, N. Prokof'ev, and B. Svistunov, *Phys. Rev. A* **75**, 013619 (2007).

[104] Q. Zhou, T.-L. Ho, arXiv:0908.3015.

[105] M. Olshanii and D. Weiss, *Phys. Rev. Lett.* **89**, 090404 (2002).

[106] F. Gerbier, A. Widera A, S. Fölling, O. Mandel, T. Gericke and I. Bloch, *Phys. Rev. Lett.* **95** 050404(2005).

[107] M. Popp, J.-J. Garcia-Ripoll, K. G. Vollbrecht, and J. I. Cirac, *Phys. Rev. A* **74**, 013622 (2006); T.-L. Ho and Q. Zhou, Proc. *Natl. Acad. Sci. U.S.A.* **106**, 6916 (2009); J.-S.Bernier, C. Kollath, A. Georges, L. De Leo, F. Gerbier, C. Salomon, and M. Köhl , *Phys. Rev. A* **79**, 061601(R) (2009).

[108] B. Capogrosso-Sansone, E. Kozik, N. Prokof'ev, and B. Svistunov, *Phys. Rev. A* **75**, 013619 (2007).

[109] G. Pupillo, C. J. Williams, and N. V. Prokof'ev, *Phys. Rev. A* **73**, 013408 (2006).

[110] A. Hoffmann and A. Pelster, *Phys. Rev. A* **79**, 053623 (2009).

[111] C. Sanner, E. J. Su, A. Keshet, R. Gommers, Y. Shin, W. Huang, and W. Ketterle, *Phys. Rev. Lett.* **105**, 040402 (2010).

[112] D. M. Weld, P. Medley, H. Miyake, D. Hucul, D. E. Pritchard, and W. Ketterle, *Phys. Rev. Lett.* **103**, 245301 (2009).

[113] P. N. Ma, L. Pollet, M. Troyer, *Phys. Rev. A* **82**, 033627 (2010).

[114] Y.-J. Lin, R. L. Compton, A. R. Perry, W. D. Phillips, J. V. Porto, and I. B. Spielman, *Phys. Rev. Lett.* **102**, 130401 (2009).

[115] T. H. Johnson, S. R. Clark, and D. Jaksch, *Phys. Rev. E* **82**, 036702 (2010); M. Žnidarič, T. Prosen, G. Benenti, G. Casati, and D. Rossini, *Phys. Rev. E* **81**, 051135 (2010).